Empirical Model Improvements for a Mixed Gas Joule-Thomson Cycle with Precooling for Cryosurgery

by

Kendra L. Passow

A dissertation submitted in partial fulfillment of the requirements for the degree of:

Master of Science

(Mechanical Engineering)

at the

UNIVERSITY OF WISCONSIN – MADISON

2012

This page is left blank intentionally.

APPROVED BY

_____

PROFESSOR GREGORY F. NELLIS

_____

PROFESSOR SANFORD A. KLEIN

DATE:_____

Empirical Model Improvements for a Mixed Gas Joule-Thomson Cycle with Precooling for Cryosurgery

Kendra L. Passow

Under the supervision of Professor Sanford Klein and Greg Nellis at the University of Wisconsin – Madison

Abstract

Cryosurgery is a medical technique that uses a cryoprobe to apply extreme cold to undesirable tissue such as cancers. An effective cryoprobe maximizes cooling power while maintaining a small and therefore ergonomic and noninvasive envelope. Precooled Mixed Gas Joule-Thomson (pMGJT) cycles with Hampson-style recuperators are integrated with the latest generation of cryoprobes to create more powerful and compact instruments. Selection of gas mixtures for these cycles is not a trivial process; the focus of this research is the development of a detailed model that can be integrated with an optimization algorithm in order to select optimal gas mixtures. A test facility has been constructed to experimentally tune and verify this model (Skye 2011). The facility uses a commercially available cryoprobe system that was modified to integrate measurement instrumentation that is sufficient to determine the performance of the system and its component parts. Spatially resolved temperature measurements in the recuperator allow detailed measurements of the heat transfer within the recuperator and therefore computation of the spatially resolved conductance. These data can be used to study the multiphase, multi-component heat transfer process in the complicated recuperator geometry.

The optimization model developed by Skye (2011) has been expanded to model the pressure drop associated with the flow in order to more accurately predict the performance of the system. The test facility has been used to evaluate the accuracy and usefulness of this improvement. A compressor model has also been formulated that relates the mass flow and compressor pressure ratio, allowing the optimization of the suction/discharge pressures and the 2^{nd} stage mass flow in addition to the refrigerant mixture composition. The adjusted empirical correlations and compressor model are used to demonstrate the design process for a fixed geometry to maximize cryoprobe performance.

Acknowledgements

I owe a great number of thank-yous to the many people who have contributed in some way to my graduate school experience. First and foremost, I would like to thank my graduate advisors, Dr. Greg Nellis and Dr. Sandy Klein. My initial meetings with them during my Visit Wisconsin weekend were a large part of my motivation to choose the University of Wisconsin – Madison, and the dedication to teaching and the intelligence that I observed then has been a true representation of how they conduct themselves daily on the 13th floor. They like to say that classes are only a distant second to research in terms of importance, but I am sure that the clear notes and interesting homeworks with real-world applications I have collected from their courses will be permanent references to me in the future. Their willingness to help with homework, sometimes responding to emailed questions late at night or on the weekends, was reflected manyfold in their commitment to guiding me through the trials and tribulations of my research. In our weekly meetings, they demonstrated a seemingly endless source of ideas – and often patience! Their prowess with a ping pong paddle has also been noted, and I hope the enthusiasm for an annual ping pong tournament will last longer than did the sprint races.

In many ways, I feel like I have had a third advisor on this project: teaching me the basics from day one, collaborating me with on the various problems we discovered, and still answering my emails promptly and with enthusiasm even after he has graduated. Harrison, I really enjoyed the time I had working with you, and not just because I would have been completely lost without your expertise as I jumped into the middle of a long-term project. Even if I am not the *shortest* member of the SEL, it has always been a fond reminder of our time sharing the lab space when I drag the various chairs and stools around in order to reach the equipment that you put together for easy access from your great height.

The other students and researchers of the SEL have made my work over the past two years so very enjoyable. Thanks to undergraduate researcher Jake Kilbane, whose long-term dedication to the project has made him an invaluable expert on the

experimentation (in addition to a sounding-board for the many problems I came across). Thanks also to the contributions of Greg Marsicek, who helped me adjust to life in the lab, and to Joe Jaeckels. I will miss the easy access to smart consultants and great people John Dyreby, Mark Rodarte, Doug Gavic, and Wenjie Zhou, as well as the other members of the lab who helped both with homework and with making the lab a true community: Ty Neises, Will Seidel, Soenke Teichel, Mike Cheadle, Jake Leachman, Amanda Pertzborn, Amir Jahromi, Jake Brenner, Stephanie Knauf, Rodrigo Barraza, Diego Fonseca, Dan Potraz, Bryant Mueller, Dan Schick, Eric Alar, Brad Moore, Brad Knier, Nevzat Akkurt, Rogelio Rosas, Bill Brey, Russell Knudson, and Dongsheng Zhang. Thanks to John Pfotenhauer, fellow Ole and SEL professor, for serving on my committee.

Gratefully acknowledged financial support for this project was provided by the Wisconsin Space Grant Consortium, the UW-Madison Graduate School Physical Sciences Fellowship, and the American Society of Heating, Refrigerating, and Air-Conditioning Engineers (ASHRAE) under Research Project 1472. Furthermore, the assistance from Endress+Hauser in equipping the lab with two new Coriolis flow meters at cost is greatly appreciated.

A final thanks to the friends and family that helped me to achieve balance and happiness during my time in Madison. The support and motivation you provided was invaluable – from helping me practice presentations and edit papers to simply listening to me describe the latest problem, I always felt like I had someone in my corner. And then of course, when I need that mental break, I had no doubt that someone would be happy to oblige, whether it was kayaking, playing frisbee, or simply cooking a good meal. I will miss you all!

Table of Contents

List of Figures

List of Tables

List of Variables

Nomenclature

a	Recuperator/precooler pressure drop and conductance correlation coefficients, Crisholm correlation coefficient for all the flow liquid (Pa m^{-1})
b	Recuperator/precooler pressure drop and conductance correlation coefficients, Crisholm correlation coefficient for all the flow vapor (Pa m^{-1})
C	Clearance volume ratio
$\overline{c}$	Average thermal capacitance (kJ kg^{-1} K^{-1})
c_p	Constant pressure specific heat (kJ kg^{-1} K^{-1})
c_v	Constant volume specific heat (kJ kg^{-1} K^{-1})
$\dot{C}$	Capacity rate of heat exchanger stream
C_r	Capacity ratio between heat exchanger streams
d	Tube diameter (m)
Eterm	Exponential term used to transition between the vapor and two-phase precooler conductance correlations
e	Tube surface roughness (m)
E_{RMS}	RMS error
f	Friction factor
$f_{trans,vap}$	Fraction of precooler tube length in the phase-transition section assumed to contain vapor-only flow
h	Enthalpy (kJ kg^{-1})
g	acceleration due to gravity (m s^{-2})
I	Electric current (A)
k	Isentropic exponent
L	Tube length (m)
$\dot{m}$	Mass flow (kg s^{-1})
min	minimum
N	Number of discrete heat exchanger sections, number of data points used for calibration

n	Polytropic exponent
N_{points}	Number of data points used in a curve fit
NTU	Number of Transfer Units in a heat exchanger
P	Pressure (kPa)
P_{ratio}	Pressure ratio
PRT	Platinum Resistance Thermometer
$\dot{Q}$	Heat transfer or refrigeration load (W)
R^2	Statistical coefficient of determination – measure of ability of curve fit to predict future outcomes
Re	Reynolds number
$Reynolds$	Reynolds number
RPM	Revolutions per minute (compressor frequency)
T	Temperature (K)
TC	ThermoCouple
UA	Conductance (W K^{-1})
UA/L	Conductance per length of finned tube (W K^{-1} m^{-1})
V	Voltage , volume
$\dot{V}$	Volumetric flow rate (m^3 s^{-1})
VF	Vapor void fraction
v	Specific volume (m^3 kg^{-1}), velocity (m s^{-1})
x	Thermodynamic quality, distance
$\overline{y}$	Mixture mole fraction vector

Greek symbols

χ	Vapor quality
Δh_T	Isothermal enthalpy difference (kJ kg^{-1})
ΔT	Temperature difference or pinch point temperature difference (K)
ΔP	Pressure drop (kPa)

ε	Heat exchanger effectiveness
η_{vol}	Volumetric compressor efficiency
μ	dynamic viscosity (N s m^{-2})
ρ	Density (kg m^{-3})
σ	Surface tension (N m^{-1})

Subscripts

#	*Temperature or pressure transducer number*
i#	*PRT# for sensors embedded in G10 sheath that surrounds the recuperator*
1^{st}	First stage cycle (vapor compression cycle)
2^{nd}	Second stage (mixed gas JT cycle stage)
3^{rd}	Third order fit region of recuperator UA/L correlation
amb	Ambient condition
avg	Averaged property
c	Cold stream
calc	Calculated value
discharge	Compressor discharge side
disp	Displacement
f	Finned tube
frict	Two-phase frictional pressure drop
G	Vapor or gas
guess	Guess value
h	Hot stream
high	High pressure stream
JT	Joule-Thomson effect – i.e. a change in fluid temperature caused by isenthalpic expansion
i	Node or heat exchanger section index
in	Inlet

L	Liquid
lin	Linear fit region of UA/L correlation
load	Cryoprobe tip refrigeration load
low	Low pressure stream
max	Maximum possible refrigeration
meas	Uncertainty related to resolution
mom	Two-phase momentum pressure drop
out	Outlet
p	Thermodynamic property associated with pressure drop calculations
pc	Precooler
pc,2ϕ	Portion of precooler tube containing two-phase flow
pp	Pinch point
rec	Recuperator
sub	Number of numerical sub-heat exchangers representing the recuperator sections between each PRT embedded in the G10 sheath
suction	Compressor suction side
total	Combined from precooler/recuperator (UA,L,P) or $1^{st}/2^{nd}$ stage ($\dot{v}$)
trans	Precooler tube section where the 2^{nd} stage refrigerant transitions from vapor to two-phase
tube,f,pc	Length of finned precooler tube section
tube,f,pc,2ϕ	Length of finned precooler tube section containing two-phase flow
tube,f,pc,vap	Length of finned precooler tube section containing vapor phase flow

1 Introduction

1.1 Cryoprobes/Cryosurgery

1.1.1 Overview

Cryosurgery is a medical technique that uses cryogenic temperatures to ablate undesirable tissue, such as tumors. Besides this application in oncology, cryotherapy is also used in gynecology and dermatology. During surgery, the tip of the cryosurgical probe (see Figure 1-1) is inserted into the body to create the cryolesion. The tip must reach a temperature of about -120ºC during this freezing process. Since these instruments are handheld during surgeries that can take upwards of one hour, they must be relatively compact and ergonomic.

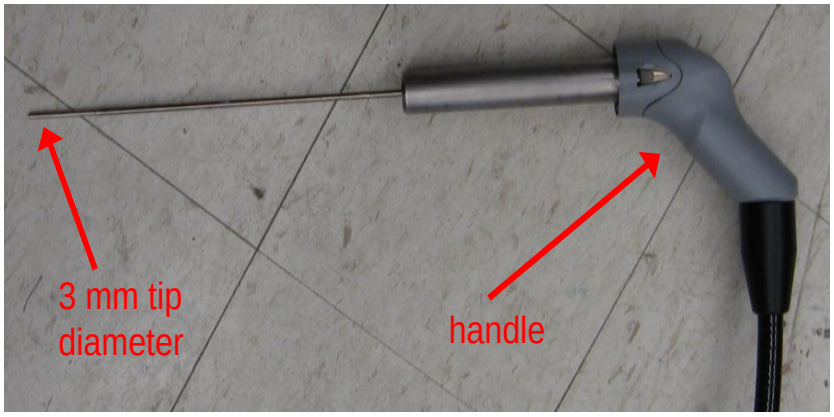

Figure 1-1: Cryoprobe used for a cryosurgical procedure, illustrating the small tip that is inserted into the body to ablate undesirable tissue. (Skye 2011)

The pear-shaped iceball that is formed at the tip of the instrument is on the order of tens of millimeters in diameter, as shown in Figure 1-2 (Frederickson 2004). The area in which cell death occurs, called the lethal zone, extends outward from the tip of the

cryoprobe to the location where the tissue temperature is at about -30ºC. These surgeries most often consist of cyclical cooling and warming to maximize cell death, and multiple probes may be used to maximize the volume of ablation or to conform to the shape of the undesirable tissue (Rubinsky 2000). Rapid cooling of the tissue and prolonged freezing both increase cell destruction, but the coldest tissue temperature achieved is the largest factor in cell death (Gage 1998).

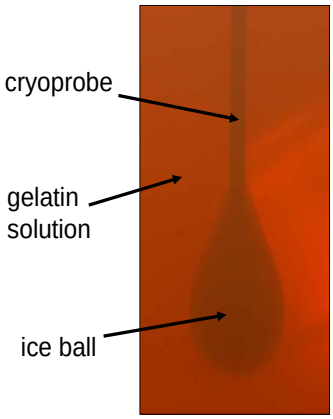

Figure 1-2: Photograph of an iceball grown in a gelatin solution using a cryoprobe. (Fredrikson 2004)

1.1.2 Mechanism of Cell Death

Cell death occurs through two major mechanisms, one immediate due to the effect of cooling and warming cycles on the cells and one delayed due to the progressive failure of the microcirculation after the tissue thaws (Gage 1998). The immediate effects are seen as the temperature begins to fall, causing cell metabolism to fail. As the tissue reaches 0ºC, ice crystals begin to form in the extracellular spaces, creating an imbalance in the osmotic pressure inside and outside of the cells. This causes water to be drawn out of the cells in the attempt to correct this imbalance, in turn causing cells to shrink and

membranes and cell constituents to be damaged. The increased electrolyte concentration in the cells during this process may be sufficient to destroy the cells. If further cooling (below -40ºC) or rapid cooling occurs, ice crystals can be found inside the cell, disrupting organelles and cell membranes and making cell death relatively certain. After surgery, the delayed effects are similar to those observed in frostbite injuries. As the tissue thaws and circulation resumes, damage to the cells lining the blood vessels results in stagnation of circulation due to platelet aggregation, and this loss of blood supply is a major cause of cell death. (Gage 1998)

1.1.3 Advantages and Disadvantages

Cryosurgical techniques hold many advantages over classical surgery. The technique is minimally invasive compared with traditional resection. It spares more healthy tissue, is shown to be effective in inducing tumor cell death, allows retreatment if necessary, and there is less risk of hemorrhage or dissemination of cancer cells. Some tumors that are unable to be removed completely through resection due to size, location, or patient health conditions are able to be treated with cryosurgery. There is also evidence that the use of cryogenic temperatures in the body elicits an immunologic response to antigens in the frozen tissue (Korpan 2007). The economics of cryosurgery are also favorable, with the associated costs usually considerably lower than those of excisional surgery.

However, there are disadvantages to the widespread use of the technology. The refrigeration power associated with today's cryosurgical instruments is limited. This means that multiple probes may be needed to treat a large area, making the technique

more invasive. Following a set freezing protocol may not destroy all undesirable tissue, so multiple procedures may be necessary to ensure the desired result. Also, accurate positioning of the probes is a difficulty, although recent advances in imaging-monitored cryosurgery using ultrasound, Magnetic Resonance Imaging (MRI), and optical spectroscopy show promise. These techniques help the physician position the probes and monitor the freezing process during surgery in the attempt to maximize the death of undesirable tissue while protecting healthy tissue. These techniques can add significant cost to an otherwise inexpensive procedure, so the precision of the technique must be balanced with the expense. (Rubinsky 2000)

1.1.4 History of Cryosurgery

Cold temperatures have been used as early as 3000 BC for medical purposes, when cold compresses were first documented as being used to treat compound skull fractures and infected wounds in ancient Egypt (Korpan 2007). However, the first successful demonstration of cryotherapy for the treatment of malignant disease occurred between 1845 and 1851, when Dr. James Arnott began using iced saline solutions (-18ºC to -24ºC) to treat advanced breast and uterine cancer (Arnott 1851). Over the next century, advancements in refrigeration techniques brought cryotherapy into more widespread use. The early 18th century saw the use of liquefied air, solid carbon dioxide 'pencils', and liquid oxygen primarily for the treatment of skin disease. Until the 1960s, freezing was used primarily to remove superficial layers of tissue in dermatology and gynecology, as depths of only 2 mm were achieved with typical swab techniques (Korpan 2007).

The era of modern cryosurgery began with the collaborative work of neurosurgeon Irving Cooper and engineer Arnold Lee, who introduced the first cryosurgical system capable of producing sizeable cryolesions deep in the body. The apparatus was supplied with liquid nitrogen (-196ºC) from a tank, which passed through the innermost tube of a vacuum-insulated cannula to produce the freezing effect at the tip (see Figure 1-3). The resultant gaseous nitrogen then escaped through an outer tube and was removed through tubing attached to a vacuum pump (Cooper 1961). Liquid nitrogen cryosurgical probes are still used today; however, difficulties with storage, transportation, and recovery of the fluid make this type of system undesirable for a surgical setting. The Joule-Thomson cryoprobe was developed by Amoils in 1965 (Amoils 1967) for use in cataract surgery using pure gas in an open cycle. Advancements with multi-stage closed cycles using mixed gases as a working fluid have made Amoils's technology the basis for the state-of-the-art-systems now in use. A two-stage mixed gas Joule-Thomson cycle is the focus of this project and is discussed in detail in Section 1.2.

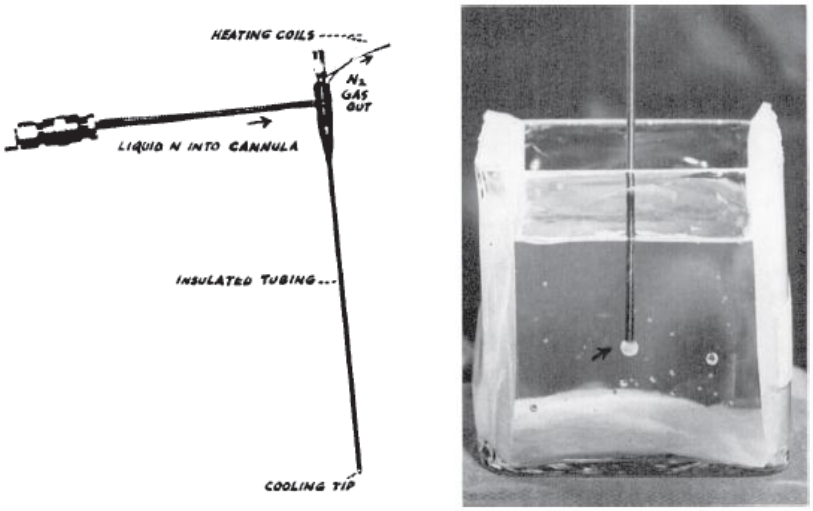

(a) (b)

Figure 1-3: (a) Diagram of cooling device designed by Irving and Lee, and (b) spherical frozen lesion produced during two minutes of passage of liquid nitrogen through the tip. (Cooper 1961)

1.2 Mixed Gas Joule-Thomson Cryoprobe Systems

1.2.1 Cycle Overview and Integration with Cryoprobe System

Figure 1-4(a) shows the cycle diagram for a mixed gas Joule-Thomson (MGJT) cycle with precooling, and Figure 1-5 shows this cycle integrated with a cryosurgical probe. High pressure gas from the remotely located compressor (state 2) is carried through the aftercooler and flexible tubing to reach the handheld cryosurgical probe (state 3). The mixed refrigerant first passes through the precooler, where it is cooled by the first stage pure refrigerant (to state 4), and then through the hot side of the recuperator, where it is cooled further by the returning low pressure, cold gas (to state 5). The mixture then expands isenthalpically through the long capillary tube (expansion valve) to reach its coldest temperature at the very tip (state 6), where it exchanges heat with the

tissue during surgery to form the cryolesion ($\dot{Q}_{load}$). The low pressure gas (at state 7) then passes back through the cold side of the recuperator, cooling the incoming high pressure gas (to state 1), and then is recovered by the compressor.

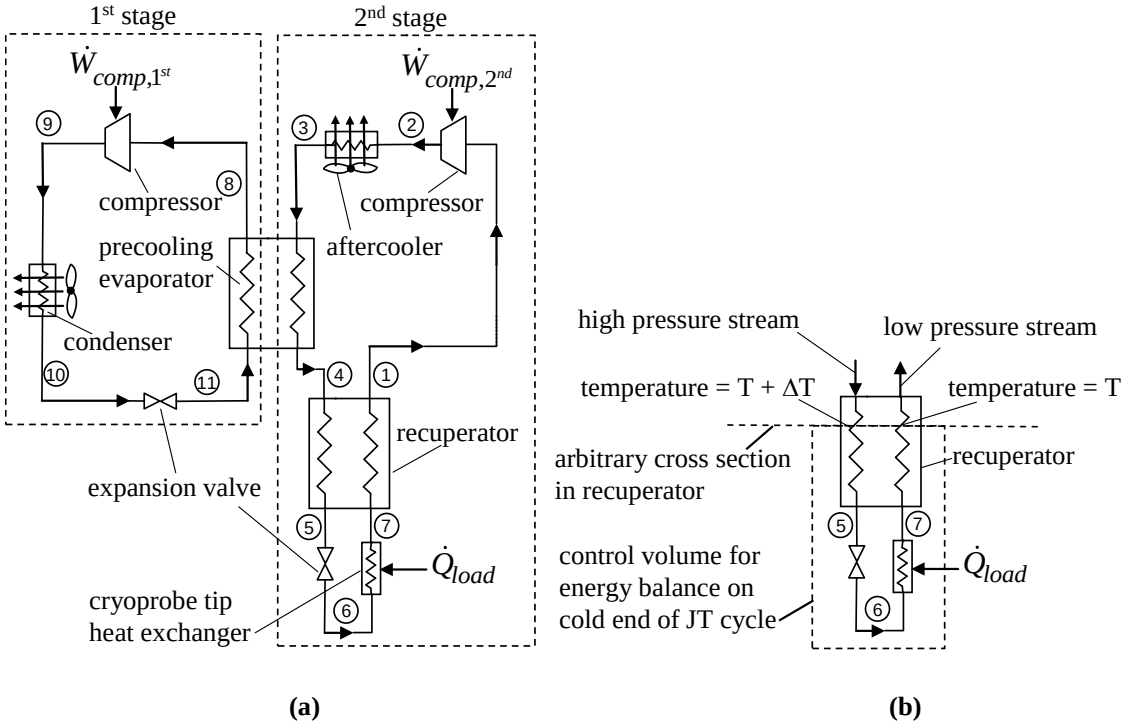

Figure 1-4: a) Schematic of two stage refrigeration cycle showing the thermodynamic states associated with each stage. b) Control volume around cold end of JT cycle which passes through an arbitrary cross section in the recuperator. (Skye 2011)

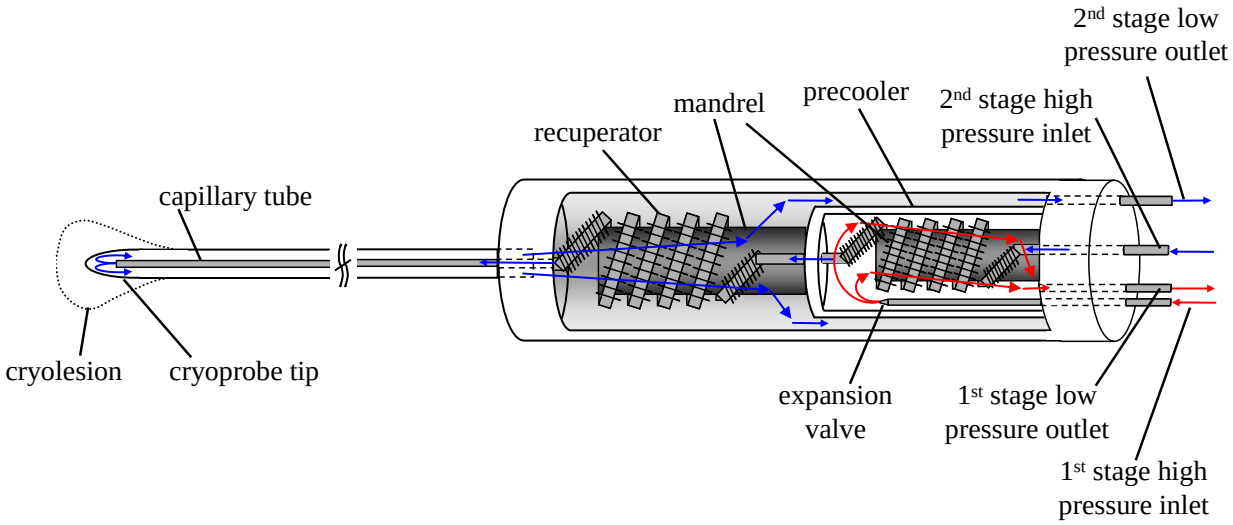

Figure 1-5: Geometric schematic of a 2 stage cryoprobe showing the fluid flow, expansion valves, cryoprobe shaft and coiled fin tube heat exchangers. (Skye 2011)

1.2.2 Optimization Criteria

A cryoprobe must have a large refrigeration power in order to successfully create the cryogenic temperatures associated with cell death. A single probe with large cooling capacity will be able to ablate a larger mass of tissue in a shorter amount of time with greater precision, reducing the need for additional, carefully maneuvered probes that may make the surgery more invasive. However, the probe must also be small in order to be ergonomic and noninvasive. The size of the instrument, as illustrated in Figure 1-1, is largely determined by the size of both the precooling and recuperative heat exchangers. Since the heat exchanger size is approximately determined by its conductance, this can be used as a figure of compactness. When designing a cryosurgical system, then, the increase in cooling capacity must be balanced with the compactness of the instrument. As a result, the most appropriate figure to judge the success of a design is the ratio of refrigeration load to the total heat exchanger conductance ($\dot{Q}_{load}/UA_{total}$).

1.2.3 Determining the Refrigeration Power

The Joule-Thomson effect, which describes the isenthalpic cooling process that occurs from state 5 to state 6 in Figure 1-4(a), regulates the refrigeration power of the cycle. The refrigeration capacity ($\dot{Q}_{load}$) can be determined by drawing an energy balance on the cold end of the cycle as in Figure 1-4(b), passing through an arbitrary location in the recuperator and encompassing the expansion valve and the heat input:

$$\dot{Q}_{load} = \dot{m}\left[enthalpy\left(P_{low}, T, \bar{y}\right) - enthalpy\left(P_{high}, T + \Delta T, \bar{y}\right)\right] \tag{1.1}$$

where $\dot{m}$ is the mass flow rate, P_{high} is the high pressure, P_{low} is the low pressure, T is the temperature of the low pressure stream at the location of the balance, ΔT is the temperature difference between the streams at the cross section, and $\bar{y}$ is a vector of the molar concentrations of each component in the gas mixture. In a perfect recuperator with infinite conductance, the minimum temperature difference between the hot and cold sides (the pinch point temperature difference ΔT_{pp}) at some point in the recuperator is zero; conversely, a poorly performing recuperator would have a large pinch point temperature difference. The enthalpy difference at the pinch point (which is the minimum enthalpy difference between the high and low pressure sides over the temperature range of the recuperator) therefore defines the maximum achievable refrigeration power:

$$\frac{\dot{Q}_{load,\max}}{\dot{m}} = \min\left(\underbrace{\left[enthalpy\left(P_{low}, T, \bar{y}\right) - enthalpy\left(P_{high}, T, \bar{y}\right)\right]}_{\Delta h_T} \text{for} \, T = T_3 \, \text{to} \, T_6 \right) \tag{1.2}$$

1.2.4 Advantages of Mixed Gas Cycles

As discussed in the previous section, in order to maximize the refrigeration power of a JT cycle, the minimum enthalpy difference (and therefore the heat transfer) must be as large as possible over the temperature span of the recuperator. Mixed gases create these large enthalpy differences due to changes in the mixture properties. For example, Figure 1-6(a) shows a pressure-enthalpy diagram for pure nitrogen, marking the isothermal enthalpy difference across several isotherms. As this figure illustrates, the isotherms are horizontal in the two phase region beneath the vapor dome, creating larger enthalpy differences. For a pressure drop (i.e. expansion through the JT valve) from 1000 kPa to 100 kPa at a temperature of 100 K, nitrogen has an enthalpy change of about 180 kJ/kg. Outside of the vapor dome at 150 K, the same pressure drop causes an enthalpy change of only about 15 kJ/kg.

In contrast, the carefully optimized mixture consisting of nitrogen, methane, ethane, propane, isobutane, isopentane, and argon in Figure 1-6(b) exhibits a vapor dome typical of mixtures: it spans a much greater temperature range, from a temperature near the lowest boiling point of the components to a temperature near the highest boiling point of the components. As a result, the enthalpy differences at 150 K, 200 K, and 250 K are all greater than 100 kJ/kg. The enthalpy difference as a function of temperature for both nitrogen and the optimized mixture are compared in Figure 1-7. The figure shows that for an equal pressure drop, the optimized mixture performs significantly better than pure nitrogen over the operating temperature span, with a minimum enthalpy difference that is 50 times greater.

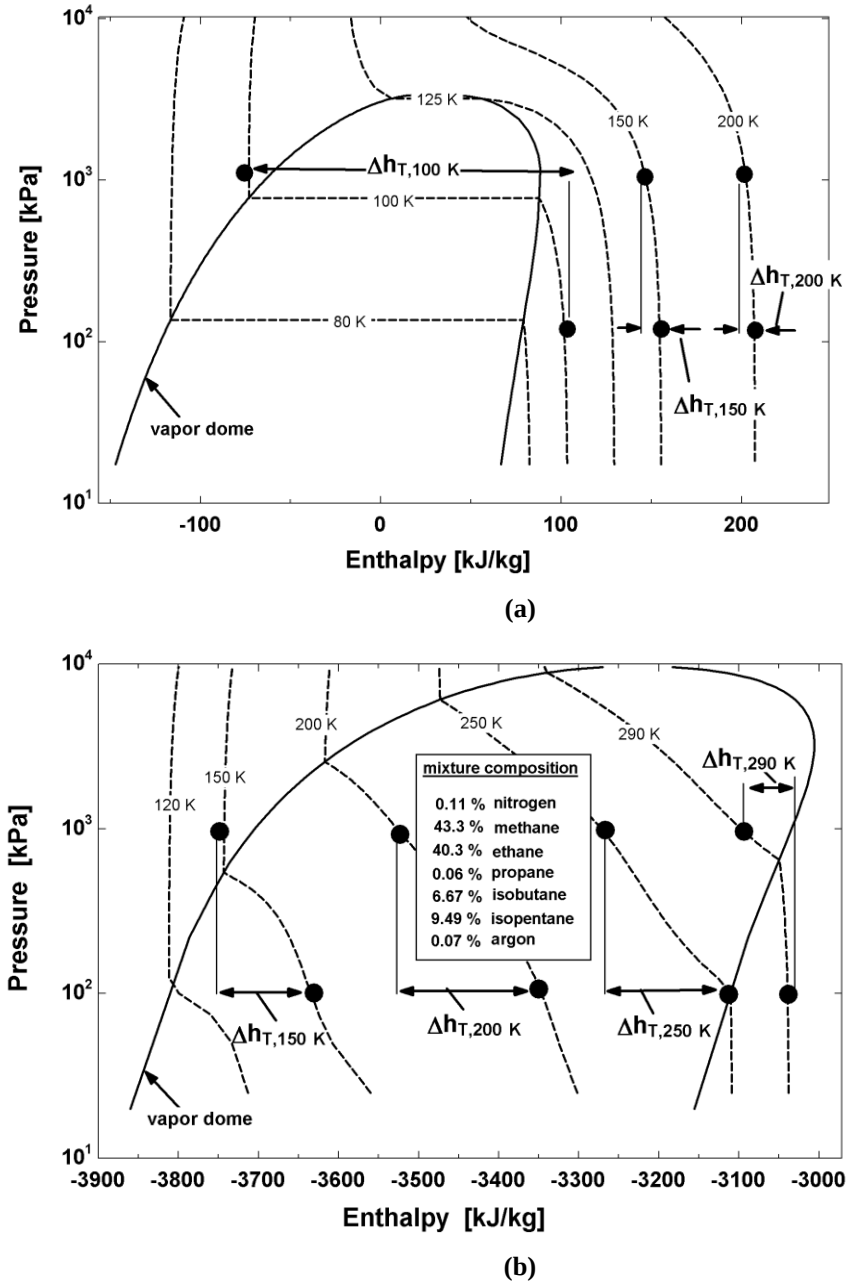

Figure 1-6: Pressure-enthalpy chart showing the evaluation of the isothermal enthalpy difference along several isotherms for (a) a single component working fluid, nitrogen and (b) a carefully optimized gas mixture of nitrogen, methane, ethane, propane, isobutene, isopentane, and argon. (Skye 2011)

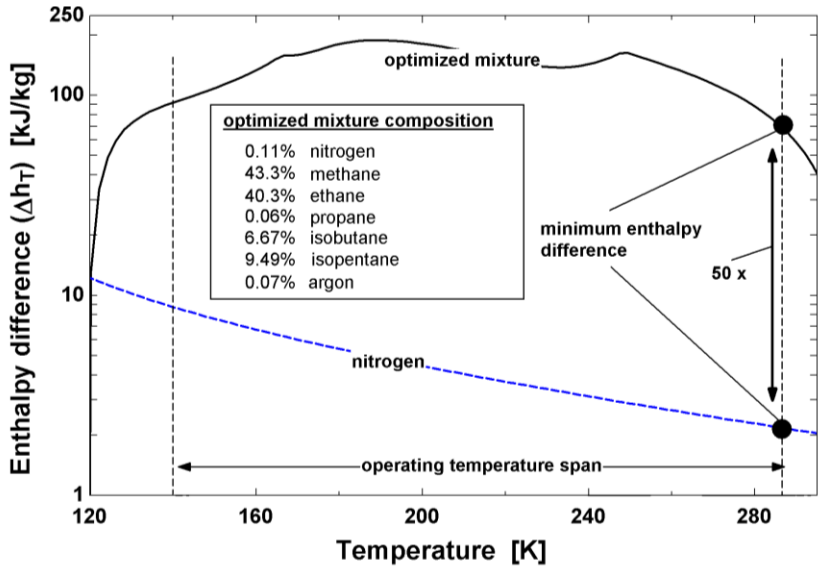

Figure 1-7: Comparison of isothermal enthalpy difference between 1000 to 100 kPa using a single component working fluid, nitrogen, and a carefully optimized mixture of nitrogen, methane, ethane, propane, isobutene, isopentane, and argon. The minimum enthalpy difference for the mixture is 50 times greater. (Skye 2011)

1.3 Previous Work

An optimization routine was developed by Keppler et al. (2004) to identify the best mixture for a single stage MGJT cycle. Given a set of refrigerant mixtures and a specified set of operating conditions, the method uses the genetic optimization algorithm (Charbonneau 2002; PIKAIA) to maximize the probe refrigeration per unit of heat exchanger conductance. Figure 1-8 shows an example of the optimization to obtain the maximum refrigeration at varying target load temperatures (125 K, 150 K, 175 K, 200 K, and 215 K), resulting in five different optimized mixtures composed of the same components (including argon, krypton, R116, R22, R14, R23, R32, R134a, and R125). Conditions consistent with the physical parameters for a commercially available cryoprobe were used: a heat rejection temperature of 293.2 K, a compressor discharge

pressure of 2,500 kPa, a compressor suction pressure of 250 kPa, a compressor suction volumetric flow rate of 100 cc/sec, and a total recuperator conductance of 10 W/K.

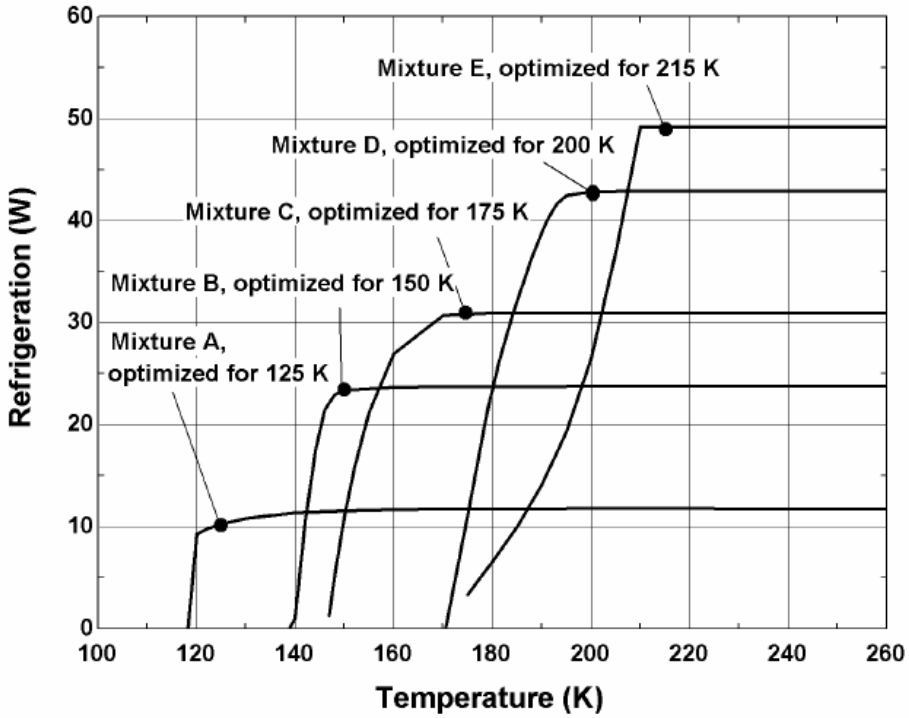

Figure 1-8: Refrigeration load curves for mixtures of synthetic refrigerants with krypton and argon, optimized for refrigeration power at various load temperatures. (Fredrickson 2004)

Figure 1-8 demonstrates the tradeoff between high refrigeration power and low no-load temperatures as well as low temperature refrigeration power. However, it is not apparent from this figure which mixture will produce the largest diameter cryolesion and therefore be the most effective at causing cell death. Frederickson (2004) modeled the geometry of a commercially available cryosurgical probe and developed a numerical model to describe the effect of load curve shape on cryolesion size. The optimization routine created by Keppler et al. (2004) was incorporated in Frederickson's work to create a design method that combines the steady state characteristics of iceball growth

with the locus of optimized mixtures in order to identify the appropriate optimization temperature for the design mixture in a cryosurgical probe. An example of a design chart is shown in Figure 1-9 for a fixed volumetric flow rate of 200 cc/s entering the suction side of the compressor in a closed JT cycle. The design point shows a case where the manufacturer has designed a probe with a 600 mm^2 area, with a recuperator conductance of 12.5 W/K and a compressor capacity of 200 cc/s. The point of intersection of the probe area and recuperator conductance is found to correspond to a temperature of 175 K. This is the temperature at which the mixture should be optimized in order to maximize the iceball radius produced by a cryoprobe operating with a given set of constituent refrigerants.

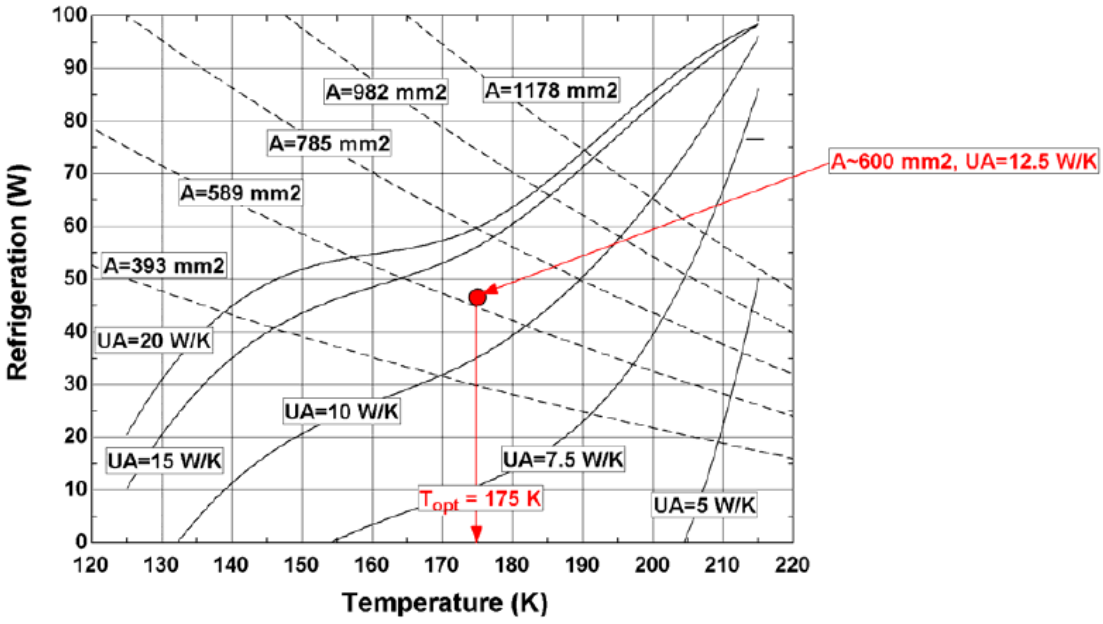

Figure 1-9: An example of a design chart created for a fixed volumetric flow rate of 200 cc/s entering the suction side of the compressor in a closed JT cycle. Solid lines represent the best mixture locus for a fixed heat exchanger conductance, while dashed lines represent the steady state refrigeration power and steady state temperature attainable in the tissue. The intersection of the solid and dashed lines identifies the temperature at which the mixture should be optimized in order to yield the largest possible iceball. (Frederickson 2004)

Skye (2011) expanded the optimization routine developed by Keppler et al. (2004) and Frederickson (2004) from a single-stage to a two-stage MGJT system. This pinch point model made the following assumptions:

(a) The 2nd stage aftercooler and 1st stage condenser were not explicitly modeled; they were assumed to be sufficiently large to cool the compressor outlet fluid to ambient temperature.
(b) The 1st stage fluid exiting the precooler was assumed to be a saturated vapor.
(c) The pressure drops in the heat exchangers (both the precooler and the recuperator) were neglected, such that the only pressure drops in the system occurred in the compressors and expansion valves.
(d) The performance of the heat exchangers was estimated using a specified pinch point temperature difference.

Therefore, the inputs to the system were limited to the high and low pressures governing each stage, the fluid compositions, the ambient temperature, the load temperature, and the pinch point temperature differences in the two heat exchangers. The model showed that adding a second stage offers a more compact cryoprobe without a significant change in the compressor size or power consumption.

This overly simplistic model neglects the impact of the operating conditions, mixture properties, and geometry on the performance of the recuperator, which in turn largely regulates the performance of the overall cycle. The failure of this model to characterize the complex fluid dynamics in the recuperator, involving multiple components and two-phase flow through a complicated geometry, may cause selected

optimal mixtures to perform poorly in the system. As a result, the mixture selection process needs to rely heavily on trial-and-error experimental testing that is both costly and time consuming. The empirical model described in Skye 2011 seeks to capture the complicated performance of the gas mixtures in the commercial system by creating component-level models that are experimentally tuned and verified. The experimental testing is summarized in Chapter 2. Figure 1-10 compares the cryoprobe tip refrigeration measured in the experiment with the values predicted by three different models:

(a) the minimum isothermal enthalpy difference (Δh_{JT}) model, which calculates the refrigeration power as described in Section 1.2.3,
(b) the pinch point model, as described earlier in this section, which estimates the heat exchanger performances by specifying the pinch point temperature difference, and
(c) the empirical model, which uses pressure drop and conductance correlations formed from experimental data to predict the component performance.

As this figure shows, the simpler pinch point and Δh_{JT} models tend to overpredict the refrigeration power, whereas the empirically tuned model provides a more realistic but sometimes over-conservative estimate. The empirical model may improve the prediction of the system refrigeration power, especially for refrigeration less than 15 W, but there are still possible improvements to be made. In particular, Skye's empirical model assumes that the pressure drop through the precooler and the recuperator are equal. Also, the optimization model requires fixed mass flow and compressor pressure inputs; however, for a specified compressor, the pressure ratio and mass flow will be related.

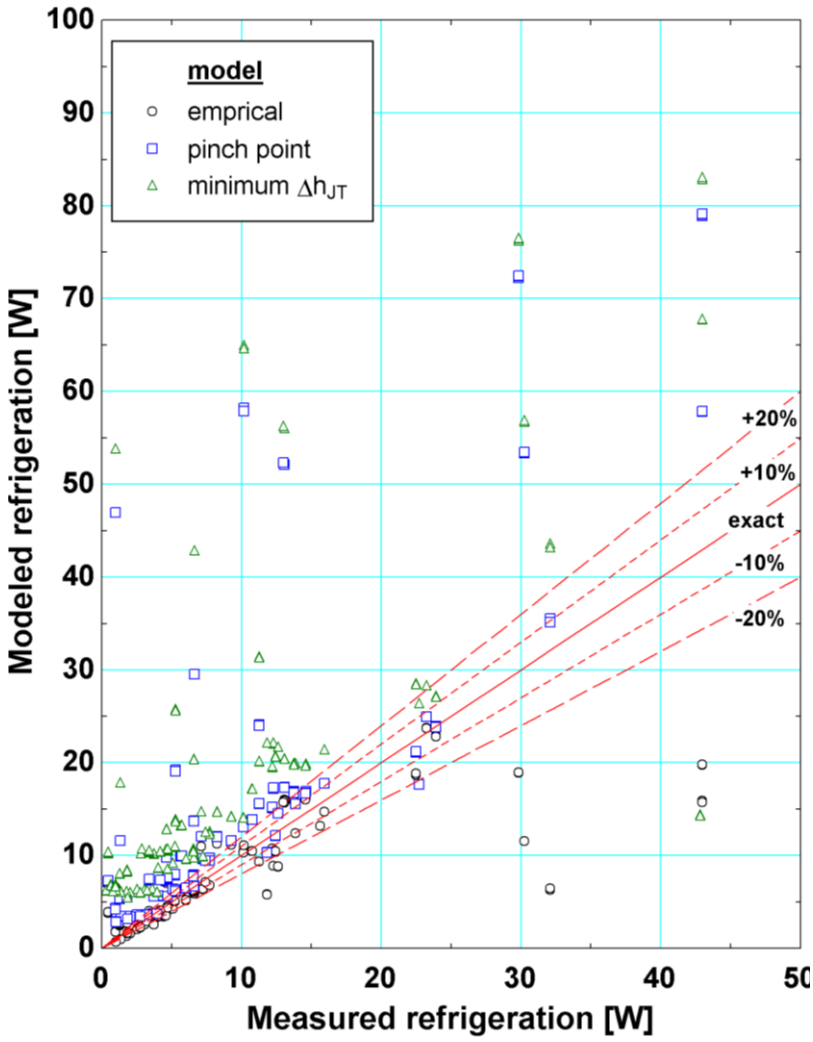

Figure 1-10: Measured and predicted refrigeration power for the empirical model, the pinch point model, and the isothermal enthalpy difference model. (Skye 2011)

1.4 Research Goals and Outline

The primary objective of this research is to develop an empirical MGJT cryoprobe model that can be used to optimize the mixture composition given a certain set of operating conditions. The first generation empirical model developed by Skye (2011) shows a significantly improved prediction power compared with the simpler minimum isothermal enthalpy difference and pinch point models (see Section 1.3). However, this

model still makes two major assumptions regarding the pressure drops through the heat exchangers and the compressor performance that are the focus of this thesis. First, the pressure drops through the hot sides of the precooler and the recuperator were formerly assumed to be equal; this thesis describes the implementation of a two-phase pressure drop model to calculate a more physics-based prediction of the intermediate pressures in the heat exchangers and therefore of the conductance. Second, the optimization model that uses the empirical correlations requires fixed mass flow and compressor pressure inputs; for a particular compressor, specifying either the mass flow or the pressure ratio should determine the other parameter. In the improved model, then, a performance map is formulated for the compressor used in the commercial cryoprobe system to predict the mass flow rate for given suction and discharge pressures.

Chapter 2 discusses the experimental testing that was conducted to formulate the empirical model, including an overview of the test facility, experimental modifications, and the test matrix. Chapter 3 demonstrates the data processing procedure, which uses numerical heat exchanger models and the new pressure drop model to calculate the thermodynamic state points and system performance parameters. Chapter 4 presents the pressure drop model that is implemented in the data processing procedure to make more physics-based predictions of the pressure drop and intermediate pressures in the heat exchangers (which are important parameters in calculating the total conductance). Chapter 5 compares the new correlations created using the data processed using the new pressure drop model with the correlations from Skye 2011. Chapter 6 discusses the compressor model that is used in the optimization to link the mass flow to the pressure

ratio in the compressor. Chapter 7 gives examples of optimizations for a fixed geometry, including optimizations that use the genetic algorithm with the new correlations for pressure drop and the compressor map to select optimal operating conditions and refrigerant mixtures. Finally, Chapter 8 discusses conclusions and gives recommendations for future work on this project.

1.5 References

Amoils, S.P. The Joule Thomson Cryoprobe. *Archives of Ophthalmology* 1967; 78(2):201-207.

Arnott, J. On the Treatment of Cancer by the Regulated Application of an Anaesthetic Temperature. London: Churchill 1851

Brodyansky, V.M., Gresin, A.K., Gromov, E.M., Yagodin, V.M., Nicolsky, V.A., Alpheev,
V.N. 1973. The Use of Mixtures as the Working Gas in Throttle Joule Thomson Cryogen Refrigerators. *Proceedings of the 13th International Congress of Refrigeration, Washington,*
D.C. Progress in Refrigeration Science and Technology 1971; Vol. 1:43-46.

Charbonneau, P. 2002. *Release Notes for PIKAIA 1.2*, NCAR Technical Note 451+STR (Boulder: National Center for Atmospheric Research).

Cooper, I.S. and A.J. Lee. Cryostatic Congelation: A system for Producing a Limited, Controlled Region of Cooling or Freezing of Biologic Tissues. *Journal of Nervous and Mental Disease* 1961; 133(3):259-263.

Fredrikson, K. 2004. Optimization of Cryosurgical Probes for Cancer Treatment. M.S. thesis. Madison, WI USA: University of Wisconsin - Madison, Mechanical Engineering Dept.

Fredrikson, K.; Nellis, G.; Klein, S. A. A Design Method for Cryosurgical Probes. *International Journal of Refrigeration* 2006; 29:700-715.

Gage, A.A. and J. Baust. Mechanism of Tissue Injury in Cryosurgery. *Cryobiology* 1998; 37: 171-186.

Gong, M.Q., Luo, E.C., Zhou, Y., Liang, J.T., and L. Zhang. Optimum Composition Calculation for Multicomponent Cryogenic Mixture Used in Joule-Thomson Refrigerators. *Advances in Cryogenic Engineering* 2000; Vol. 45A:283-290.

Keppler, F. Nellis, G. and Klein, S. Optimization of the Composition of a Gas Mixture in a Joule-Thomson Cycle. *International Journal of Heating, Ventilation, Air Conditioning, and Refrigeration Research* 2004; 10(2):213-230.

Korpan, Nikolai. A History of Cryosurgery: Its Development and Future. *Journal of the American College of Surgeons* 2007; 204(2):314-324.

Müller-Steinhagen H, Heck K. A simple friction pressure drop correlation for two-phase flow in pipes. *Chem Eng Process* 1986; 20:297-308.

Skye, H.M. 2011. Modeling, Experimentation and Optimization for a Mixed-Gas Joule-Thomson Cycle with Precooling for Cryosurgery. PhD thesis. Madison, WI USA: University of Wisconsin – Madison, Mechanical Engineering Department.

2 Preliminary Experimental Work

2.1 Test Facility Overview

The experimental test facility, described in detail in Chapter 4 of Skye 2011, was constructed by modifying a commercially available cryoprobe system from American Medical Systems to integrate measurement instrumentation. The instrumentation (see Table 2-1 for summary of instrumentation and errors) was chosen such that the heat exchanger conductance could be predicted with less than 10% uncertainty. All measurements are monitored using a National Instruments data acquisition system with LabVIEW. A schematic of the experimental cycle is shown in Figure 2-1. The pressure measurements are shown with "P#"; the temperatures are measured with ThermoCouples ("TC#") and Platinum Resistance Thermometers ("PRT#"). Additional PRTs ("PRT_i") measure intermediate temperatures on the low pressure stream of the recuperative heat exchanger, allowing a more precise calculation of the heat exchanger conductance. The mass flow rates of each stage were originally measured with calorimetric flow meters, such that the measurement had to be adjusted based on the specific heat of the refrigerants; recently, these meters were replaced by Coriolis flow meters (see Section 2.2.2 for further discussion). A nichrome wire heater is attached to the cryoprobe tip to simulate the biological thermal load. An interchangeable jewel orifice and a bypass valve on the 2nd stage compressor are used to independently regulate the pressure ratio and mass flow in the system. The cold test section of the experiment is covered with seven layers of MultiLayer Insulation (MLI) and enclosed in a vacuum dewar (pressure <1e-4 torr) to minimize parasitic heat leak. A gas chromatograph was integrated with the system to determine the 2nd stage mixture composition during collection of steady state

data. Recent modifications allow the composition data to be collected and analyzed digitally rather than using a manual integrator.

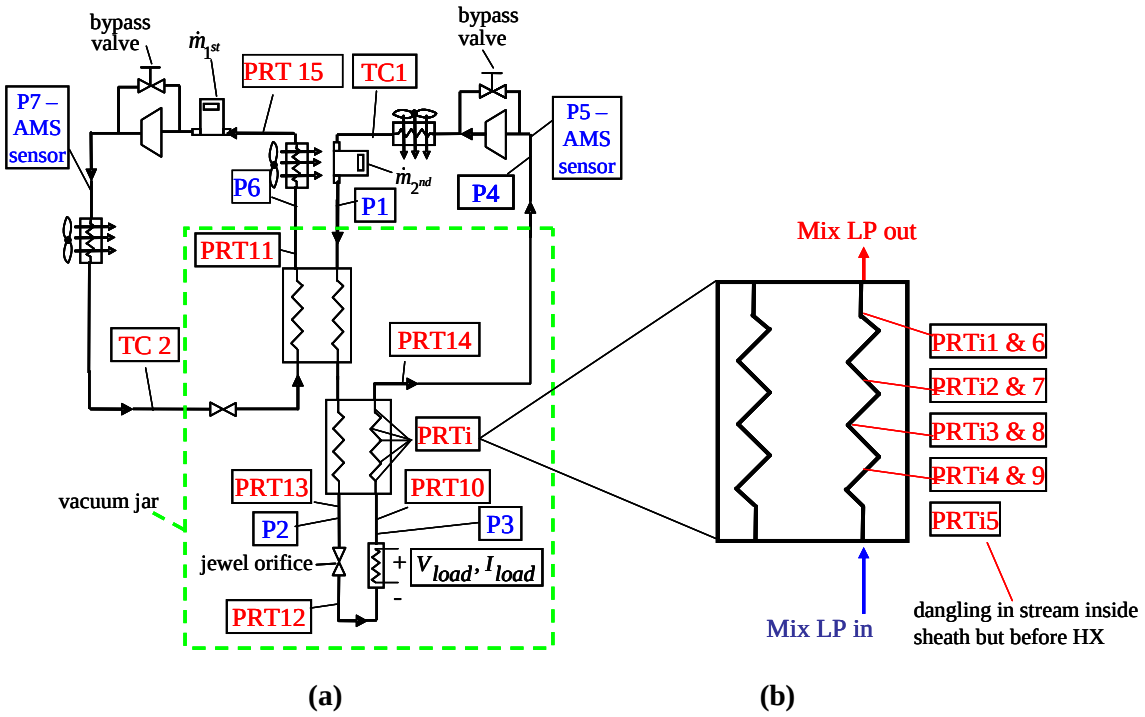

Figure 2-1: (a) Schematic of experimental cycle showing the location of measurements. (b) Expanded view of recuperator showing location of temperature sensors. (Adapted from Skye 2011)

Table 2-1: List of temperature, pressure, and mass flow sensors used in the experimental test facility. (Adapted from Skye 2011)

Measurement	Label on Figure 2-1	Manufacturer	Part #	Actual precision
Temperature (PRT)	PRT 1,5,6,7,8,8a, 11	Lakeshore	PRT-111	0.5 K (calibrated in situ)
Temperature (PRT_i)	$PRT_{rec,i}$	Lakeshore	PRT-111	0.5 K (calibrated in situ)
Temperature (ThermoCouple)	TC 3,8,10	Lakeshore	9006-004	~1 K in 290-400 K range
Mixture high pressure ($P_{h,2^{nd}}$)	P1	Setra	206-500G	0.65 psi, plus drift = 3 psi total
Mixture high pressure ($P_{h,2^{nd}}$)	P2	Setra	206-500G	0.65 psi, plus drift = 3 psi total
Mixture low pressure ($P_{l,2^{nd}}$)	P3	Setra	206-100G	0.15 psi, plus drift = 1.5 total
Mixture low pressure ($P_{l,2^{nd}}$)	P4	Setra	206-100G	0.15 psi, plus drift 1.5 total
Pure fluid high pressure ($P_{h,1^{st}}$)	P7	Setra	206-500G	0.65 psi, plus drift =3 psi total
Pure fluid low pressure ($P_{l,1^{st}}$)	P6	Setra	206-100G	0.15 psi, plus drift = 1.5 total
1^{st} stage mass flow-old ($\dot{m}_{1^{st}}$)	$\dot{m}_{1^{st}}$	Omega	FMA1742-EPDM	3% F.S. = 0.03*100 stdL/min = 3 stdL/min

Measurement	Label on Figure 2-1	Manufacturer	Part #	Actual precision
2nd stage mass flow-old ($\dot{m}_{2^{nd}}$)	$\dot{m}_{2^{nd}}$	Omega	FMA1741ST-EPDM	3% F.S. = 0.03*80 stdL/min = 2.4 stdL/min
1st stage mass flow-new ($\dot{m}_{1^{st}}$)	$\dot{m}_{1^{st}}$	Endress&Hauser	ProMass 83A	0.5% o.r., 1% o.r. for low flow
2nd stage mass flow-new ($\dot{m}_{2^{nd}}$)	$\dot{m}_{2^{nd}}$	Endress&Hauser	ProMass 83A	0.5% o.r., 1% o.r. for low flow
Cryoprobe load ($\dot{Q}_{load}$)	$\dot{Q}_{load}$	--	--	0.00001 W
Heater voltage V_{load})	V_{load}	--	--	0.005 V
Heater current (I_{load})	I_{load}	--	--	0.002 A
Mixture composition ($y_{2^{nd}}$)		Air Liquide		3% absolute

2.2 Experimental Modifications

2.2.1 Oil System for Prevention of Freezing in 2nd Stage

Controlling the purity of the fluid in the test section is critical for the operation of the experimental test facility. If oil from the compressor migrates into the test section or air is allowed to contaminate the cycle during charging the cycle or general maintenance, freezing at the cold end at the small-diameter opening of the Joule-Thomson orifice (0.01 inch to 0.02 inch) can cause complete obstruction of the flow stream. Figure 2-2 shows an example of such behavior during early testing: the jewel orifice temperature and mass flow are plotted as a function of time, and the steep dropoff in mass flow at a low tip temperature of around 267 K indicates an obstruction due to freezing. This cause was confirmed when deconstruction of the cold end of the system for cleaning showed large amounts of oil.

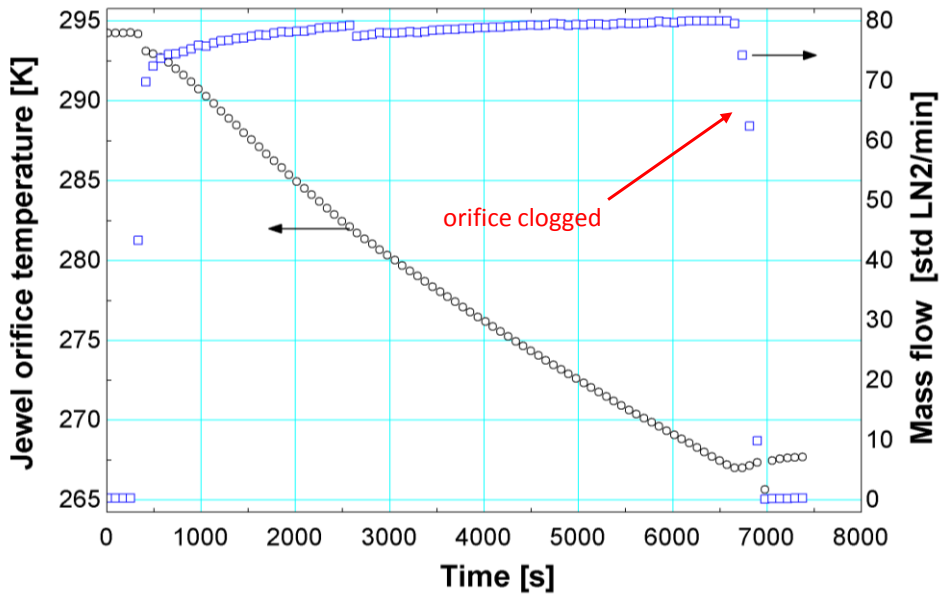

Figure 2-2: Jewel orifice temperature and mass flow as a function of time. The steep decline in mass flow at the low tip temperature indicates a clog due to freezing.

Experimental modifications were made to address the issues with freezing in the test section. The former setup is shown in Figure 2-3. Originally, the high pressure fluid exited the compressor, passing through a single oil separator before continuing on to the experiment. Any oil trapped would fall through the bottom of the separator to be returned to the compressor through a solenoid valve. The manufacturer controls have this solenoid open at the beginning of each freeze cycle (every 20 minutes); however, achieving steady state in the modified system with greater thermal mass can take up to two hours of uninterrupted flow. As a result, the automatic cycling was deactivated such that the solenoid only opened once at the beginning of testing. However, with the test facility running continuously for upwards of ten hours, this was insufficient to carry the accumulated oil back to the compressor. The revised experimental hardware after many trials is pictured in Figure 2-4. The high pressure gas from the compressor travels through two oil separators and a filter-drier before passing on to the experiment. Any oil caught in the separators falls through, where it is flushed back into the compressor by periodic opening of the two solenoid valves, which are regulated in the computer interface.

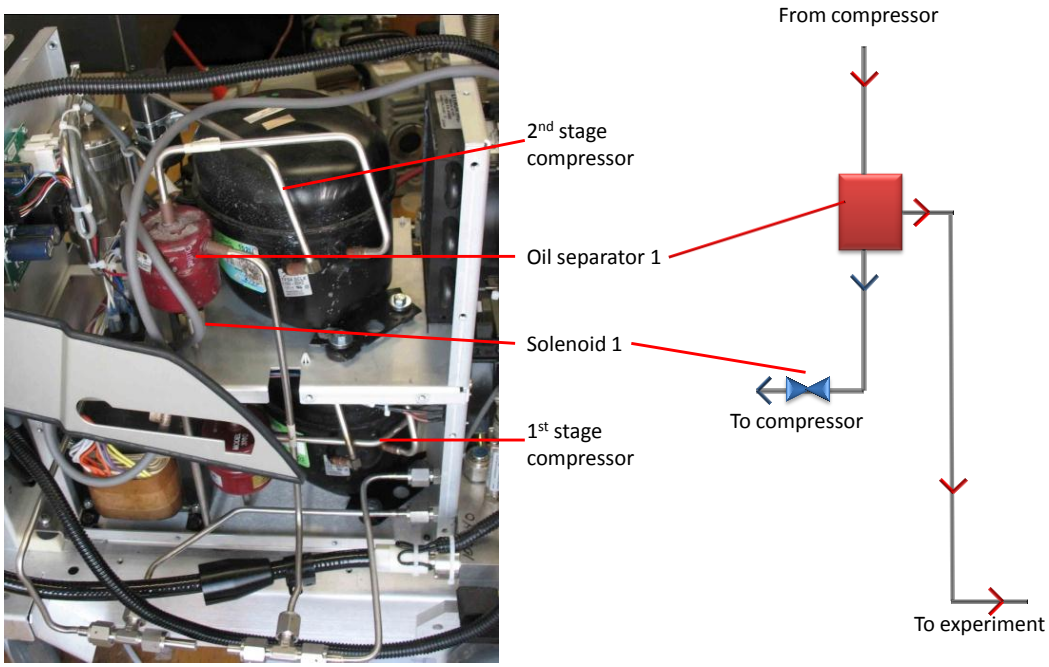

Figure 2-3: Photo and diagram of former setup used to control the oil migration into the system.

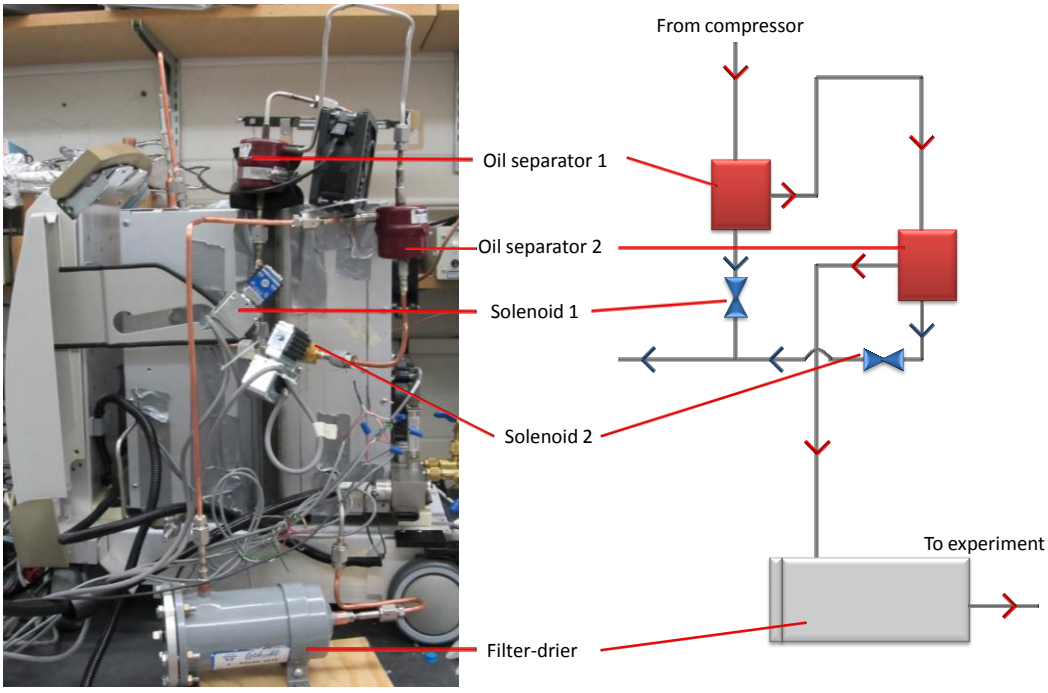

Figure 2-4: Photo and diagram of new setup used to control the oil migration into the system with added oil separator, solenoid system, and filter-drier.

2.2.2 Mass Flow Meters

The mass flow in both cycles was originally measured using calorimetric flow meters from Omega (FMA1742-EPDM for the 1st stage and FMA1741ST-EPDM for the 2nd stage). At the end of August 2011, these mass flow meters were taken out of the system and tested in parallel and the readings were found to be 40% different (see Figure 2-5). The mass flow error is thought to be related to the principle of operation of the calorimetric flow meters. In these meters, a small portion of the mass flow entering the meter is diverted through a capillary stainless steel sensor tube, where a precision heater causes a small temperature rise. The measured temperature-dependent resistance differential is linearly proportional to the flow rate, allowing this value to be determined. It is possible that for the issues with compressor oil entering the experimental test section, some of the oil travelled through the capillary tube and either changed the reading due to the difference in the material properties or partially clogged the flow pathway. In either case, the flow meters were recalibrated and the sensors were replaced by Omega in September 2011. Unfortunately, this means that there is a high unknown uncertainty in the mass flow for all 198 tests used to create the empirical correlations described in Chapter 5. This may explain some of the variability in the data used for these correlations.

The short circuit data described in Section 6.3.2 was taken using the recalibrated calorimetric meters (with the filter-drier system implemented to keep oil out of the test section). The data taken with the bypass closed for the compressor map (see Section 6.2) used two different Coriolis meters. First, a MicroMotion CMF010 (accuracy ±0.35 o.r.)

was loaned to the lab. Then, two ProMass 83A Coriolis flow meters (one for each stage) were purchased for this experiment from Endress+Hauser. Since these meters use the Coriolis effect to directly measure the mass flow, the uncertainty due to the estimation of mixture properties in the data processing is eliminated. Additionally, the meters also measure density, which may help monitor the presence of oil in the cycle. The mass flow uncertainty for gases for the E&H meters is ± 0.50% o.r.; however, since the experiment operates below 10% of maximum flow, this error is estimated at ±1% based on the calibration curve provided by the manufacturer.

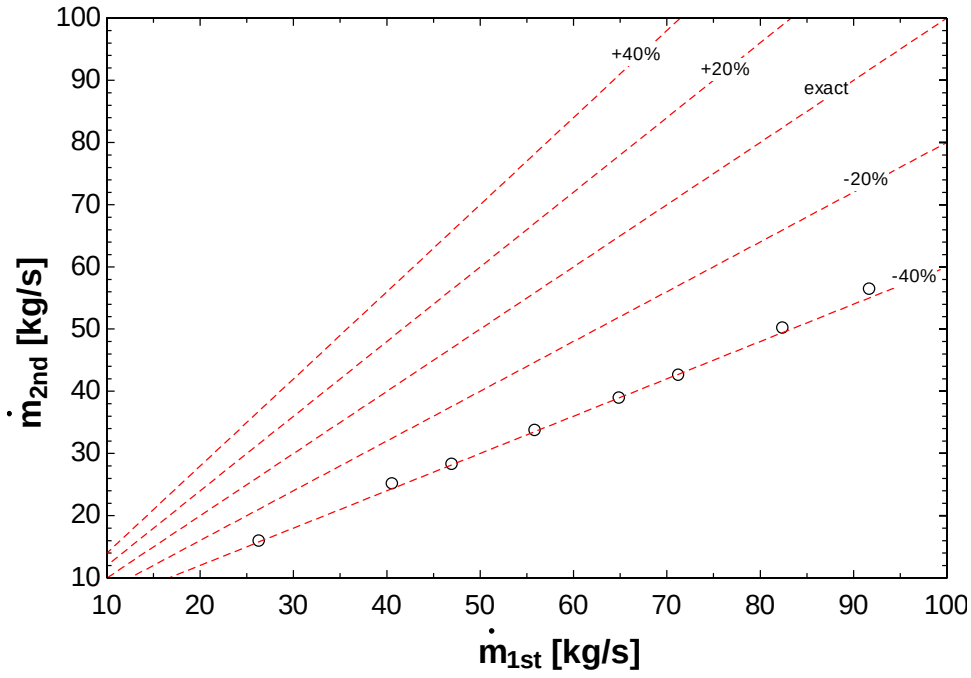

Figure 2-5: 2nd stage mass flow as a function of first stage mass flow measured with Omega calorimetric meters, August 2011.

2.3 Test Matrix

The heat transfer in the precooler is relatively well understood. The gas mixture exchanges heat with the constant temperature, saturated 1st stage pure fluid, and will exit the precooler at about the same temperature regardless of the mixture composition (see Section 5.2.1 of Skye 2011 for detailed discussion). In contrast, the heat transfer in the recuperator is complicated by the two-phase flow through both the hot and cold sides of a complex heat exchanger geometry. As a result, the focus of the experimental data is mapping the heat transfer performance of the recuperator associated with two-phase flow. The two phase flow and pressure drop are mostly a function of thermodynamic quality and mass flux, so experimental conditions are chosen to achieve the maximum range of these parameters. The quality is determined largely by the load temperature and the recuperator temperatures, the high and low pressures, and the mixture composition. The mass flux is a function of the high and low pressures, as varied using the compressor bypass valve and the jewel orifice (0.0175 inches for the tests discussed here), as well as the total charge pressure of the system.

Table 2-2 summarizes the four different sets of experimental data taken for a total of 198 data points. Sets 1 and 2 are composed of tests taken with working fluids of pure R14 and R23, respectively, with the precooling cycle turned off. These tests are useful for system debugging and test facility verification, because the property data for pure components are well defined. In contrast, mixture properties must be calculated using complicated equations of state, introducing a larger uncertainty. The comparison of the measured and calculated JT effect, as described in Section 0, is one example of how these

pure fluid tests are used for verification. The third set of tests used a precisely formed mixture of argon, R14, and R23 to explore the composition shift of the circulation mixture (see Section 5.4.2 of Skye 2011). This set of data also has some tests with two-phase flow in the recuperator, but the minimum quality observed was 0.8. To explore the heat transfer performance at lower qualities, the argon was left out of the working fluid for the fourth set of data; instead, R14-R23 mixtures were created from the pure components by combining them in the experimental test facility. These tests from Set 4 represent the majority of the two-phase data collected and were the primary source of the data used to develop the empirical correlations as discussed in Chapter 5.

Table 2-2: Summary of test parameters for the collected data. (Skye 2011)

	Set 1	**Set 2**	**Set 3**	**Set 4**
2nd stage				
Mole fraction argon	--	--	10-15%	--
Mole fraction R14	100%	--	55-65%	20-50%
Mole fraction R23	--	100%	25-35%	50-80%
High Pressure	185-350 psig	240-350 psig	190-255 psig	160-290 psig
Low Pressure	10-40 psig	11-25 psig	10-25 psig	14-100 psig
Tip temperature (T_7)	163-255 K	240-292 K	170-215 K	175-260 K
Tip thermal load ($\dot{Q}_{load}$)	0.5-17.5 W	7-24 W	0.5-7.5 W	0.3-43 W
Mass flow ($\dot{m}_{2nd}$)	0.8 -1.6 g/s	0.65-0.9 g/s	0.8-1.0 g/s	0.7-1.7 g/s
1st stage				
Working fluid	R410a	N/A	R410a	R410a
Evaporator temperature	237-240 K	N/A	240-242 K	235-242 K
mass flow ($\dot{m}_{1st}$)	1.4-2 g/s	N/A	2-2.2g/s	1.2-1.4 g/s

2.4 References

Endress+Hauser website, Promass 83A technical documentation: http://www.us.endress.com/#product/83A

Omega Engineering website, calorimetric flow meter technical manual: http://www.omega.com/Manuals/manualpdf/M1680.pdf

Skye, H.M. 2011. Modeling, Experimentation and Optimization for a Mixed-Gas Joule-Thomson Cycle with Precooling for Cryosurgery. PhD thesis. Madison, WI USA: University of Wisconsin – Madison, Mechanical Engineering Department.

3 Data Processing

3.1 Overview and List of Measurements

The experimental results are post-processed using a numerical model of the two stage refrigeration cycle. A schematic of the cycle is shown in Figure 3-1. The inputs for the post-processing analysis correspond to the experimental measurements shown in Figure 3-2. The Engineering Equation Solver (EES) software (Klein 2012) is used to carry out the thermodynamic analysis. The cycle analysis is designed to operate for a variety of 1st stage working fluids; the selection of the fluid depends on the desired precooling temperature. The analysis presented here has been tested using the refrigerant R410a, modeled with the property routines that are provided in EES. The 2nd stage refrigeration mixture property data are predicted using the REFPROP database (Lemmon 2007) through an interface to the EES program (Klein 2008).

Following experimental data collection, steady state data are entered into EES. The measurements are assigned to the corresponding cycle parameters in order to accomplish the analysis, as presented in Table 3-1. The equations in the analysis description reference the cycle parameter notation (see Figure 3-1) rather than the sensor location notation (shown in Figure 3-2).

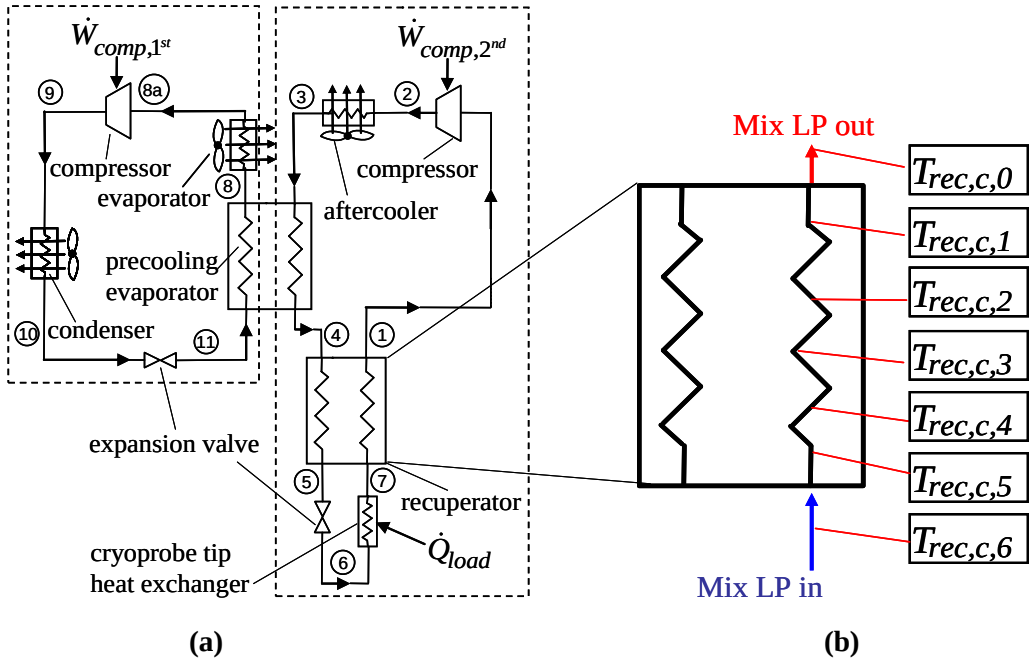

Figure 3-1: (a) Schematic of two stage refrigeration cycle showing the thermodynamic states associated with each stage. (b) Expanded view of the recuperator showing the thermodynamic states at the locations of the temperature sensors in the low pressure stream. (Adapted from Skye 2011)

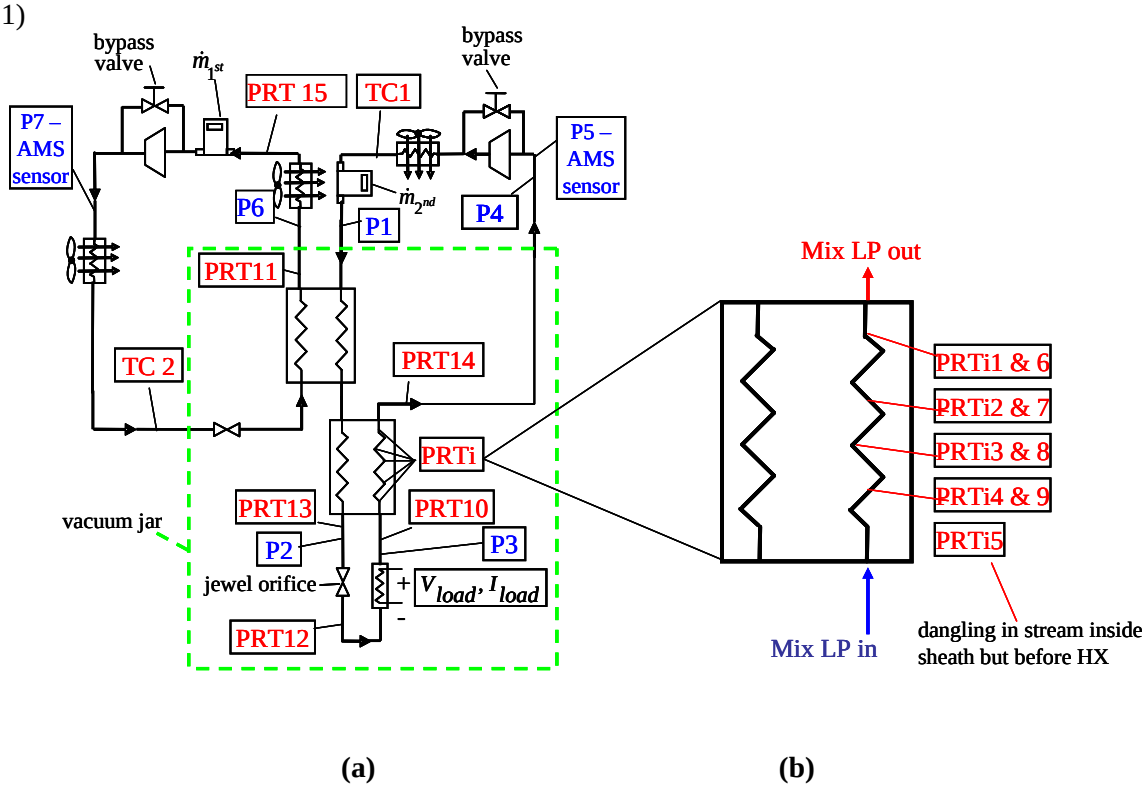

Figure 3-2: (a) Schematic of experimental cycle showing the location of measurements. (b) Expanded view of recuperator showing location of temperature sensors. (Adapted from Skye 2011)

Table 3-1: Data collected from the sensor is assigned to the corresponding cycle parameter for (a) the gas mix cycle, (b) the precool cycle, and (c) the recuperator.

(a)

State Point (Figure 3-1a)	Cycle Parameter	Sensor Name (Figure 3-2a)	Cycle Parameter	Sensor Name (Figure 3-2a)
1	P_1	P4	T_1	PRT14
2	P_2	--	T_2	--
3	P_3	P1	T_3	TC1
4	P_4	--	T_4	--
5	P_5	P2	T_5	PRT13
6	P_6	--	T_6	PRT12
7	P_7	P3	T_7	PRT10

(b)

State Point (Figure 3-1a)	Cycle Parameter	Sensor Name (Figure 3-2a)	Cycle Parameter	Sensor Name (Figure 3-2a)
8	P_8	P6	T_8	PRT11
8a	P_{8a}	--	T_{8a}	PRT15
9	P_9	P7	T_9	--
10	P_{10}	--	T_{10}	TC2
11	P_{11}	--	T_{11}	--

(c)

Cycle Parameter	Sensor Name (Figure 3-2b)
$T_{rec,c,1}$	PRT14
$T_{rec,c,2}$	Average of PRTi1 & PRTi6
$T_{rec,c,3}$	Average of PRTi2 & PRTi7
$T_{rec,c,4}$	Average of PRTi3 & PRTi8
$T_{rec,c,5}$	Average of PRTi4 & PRTi9
$T_{rec,c,6}$	PRTi5
$T_{rec,c,7}$	PRT10

3.2 Cycle Overview

3.2.1 *P-h* Diagram of Gas Mix Cycle

An example cycle schematic is shown on a pressure-enthalpy diagram in Figure 3-3. The boxed numbers correspond to the thermodynamic state points as shown in Figure 3-1. The discussion of the cycle begins with the high pressure gas leaving the second stage compressor aftercooler at state 3 (where *P* and *T* are measured) and traveling through the precooler to state 4 (note that *P* and *T* are not measured at this location). The refrigerant mixture then travels through the hot side of the recuperator to state 5 (*P*,*T* measured) and passes through the jewel orifice restriction, isenthalpically expanding to state 6 (*P*,*T* measured). The simulated biological thermal load is then applied to reach point 7 at the cryoprobe tip (*P*,*T* measured) before the low pressure gas travels back through the cold side of the recuperator (note that spatially resolved temperature sensors are integrated into this stream) to state 1 (*P*,*T* measured). The gas mixture finally returns to the compressor to begin the cycle again.

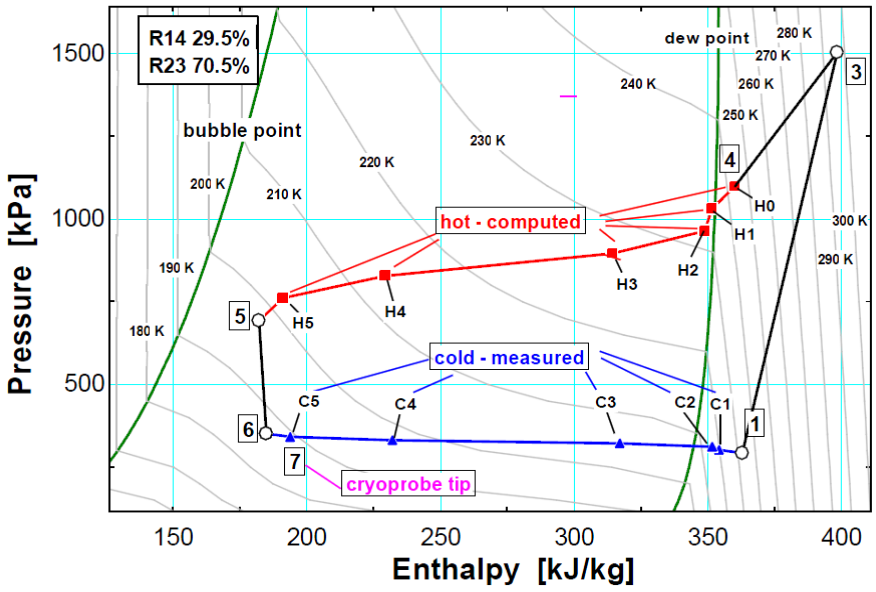

Figure 3-3: Sample set of data shown on a *P-h* diagram for the 2nd stage. (Adapted from Skye 2011)

3.2.2 Joule-Thomson Effect

One important characteristic of the cycle is the temperature difference that is induced across the 2nd stage expansion orifice due to the Joule-Thomson effect. The measured JT effect is calculated according to:

$$\Delta T_{JT,meas} = T_5 - T_6 \tag{3.1}$$

where T_5 and T_6 are the measured temperatures entering and leaving the orifice, respectively. The measured JT effect can be compared to the value predicted using the REFPROP property database. The specific enthalpy at the inlet (h_5) is computed using the measured temperature and pressure. The orifice is isenthalpic, therefore:

$$h_6 = h_5 \tag{3.2}$$

The temperature at the outlet based on the REFPROP correlation is computed using the specific enthalpy and pressure for the mixture composition (represented by $\bar{y}_{rec}$, a vector of compositions):

$$T_6 = temperature(h_6, P_6, \bar{y}_{rec}) \tag{3.3}$$

The JT effect obtained using the REFPROP values is calculated according to:

$$\Delta T_{JT} = T_5 - T_6 \tag{3.4}$$

Another check on the REFPROP correlations is provided by an energy balance on the heater. An energy balance on the heater provides an estimate of the heater power input:

$$\dot{Q}_{load} = \dot{m}_{2nd}(h_7 - h_6) \tag{3.5}$$

which can be compared to the measured heater power. The closer the agreement of these checks with the measured values, the greater confidence the user may have in both the measured values and the accuracy of this analysis. See Section 5.4.3 in Skye 2011 for comparison results.

3.3 2nd Stage Analysis

3.3.1 Cycle Properties

The analysis of the 2nd stage cycle begins by calculating the specific enthalpies at states 1, 3, 5, and 7 (h_1, h_3, h_5, and h_7 – see Figure 3-1(a)) using the measured temperature and pressure at these locations (T_i and P_i, respectively) together with the recuperator mixture composition:

$$h_i = enthalpy(T_i, P_i, \bar{y}_{rec}) \qquad i=1,3,5,7 \qquad (3.6)$$

where *enthalpy* represents the specific enthalpy computed using the REFPROP database (Lemmon 2007) that is interfaced with EES (Klein 2008). The pressure at the inlet to the heater (P_6) is not directly measured but is assumed to be equal to the pressure at the heater exit (P_7), as the pressure drop in the ¼" diameter tube that serves as the heated section is negligible compared to the 2nd stage expansion orifice:

$$P_6 = P_7 \qquad (3.7)$$

The specific enthalpy at the heater inlet (h_6) can then be calculated from the temperature and pressure:

$$h_6 = enthalpy(T_6, P_6, \bar{y}_{rec}) \qquad (3.8)$$

The pressure of the gas mixture entering the hot side of the recuperator (P_4) is not directly measured; the pressures of the gas mixture entering the precooler (P_3) and leaving the hot side of the recuperator (P_5) are measured. Previous analysis assumed P_4 to be an average of P_3 and P_5 (Skye 2011); however, it has been shown that the pressure assumed to exist at state 4 has a relatively large effect on the computed conductance (*UA*) of both the recuperator and the precooler. Therefore, the data analysis has been improved by assigning the value of P_4 using the correlation for pressure drop as described in Chapter 4. An energy balance is then used to calculate the total rate of heat transfer in the recuperator ($\dot{Q}_{rec}$) per mass flow rate of gas mix ($\dot{m}_{2nd}$) and the specific enthalpy at the hot-side inlet of the recuperator (h_4):

$$\dot{Q}_{rec} / \dot{m}_{2nd} = h_1 - h_7 \tag{3.9}$$

$$h_4 = h_5 + \dot{Q}_{rec} / \dot{m}_{2nd} \tag{3.10}$$

The temperature at the hot-side inlet (T_4) is computed using the calculated pressure (P_4) and specific enthalpy (h_4):

$$T_4 = temperature(h_4, P_4, \bar{y}_{rec}) \tag{3.11}$$

where *temperature* represents using the appropriate correlations in the REFPROP database to evaluate the temperature of the gas mix at the given state.

The recuperator is divided into six heat exchanger sections according to the points of measurement labeled in Figure 3-4(a). The last section is located at the cold end of the recuperator, as shown in Figure 3-4(b). The temperature of the cold fluid is measured directly at each location. The cold fluid pressure is not measured at these locations, but is assumed to vary linearly from P_7 to P_1, both of which are directly measured. The pressure of the cold fluid at each location is computed according to:

$$\Delta P_{rec,c} = \frac{P_7 - P_1}{6} \tag{3.12}$$

$$P_{rec,c,i} = P_{rec,c,i-1} + \Delta P_{rec,c} \qquad i = 0...5 \tag{3.13}$$

The pressure and temperature are used to calculate the specific enthalpy of the cold stream at each measurement location.

$$h_{rec,c,i} = enthalpy(T_{rec,c,i}, P_{rec,c,i}, \bar{y}_{rec}) \qquad i = 0...6 \tag{3.14}$$

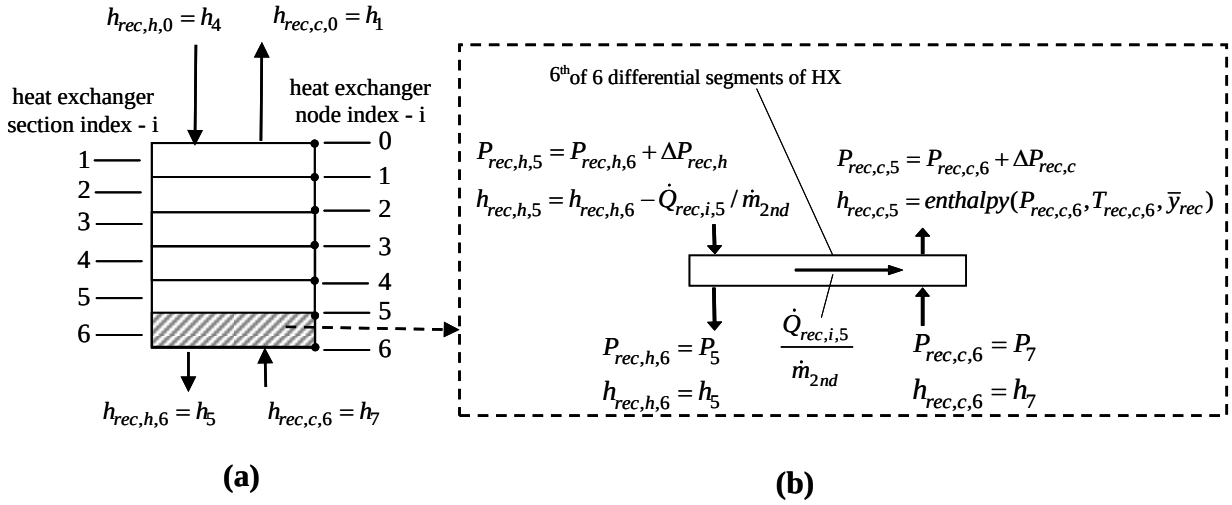

Figure 3-4: (a) Recuperating heat exchanger divided into six sections and seven nodes according to location of experimental measurements. (b) Last heat exchanger element. (Adapted from Skye 2011)

3.3.2 Calculating Recuperator Properties

The specific enthalpy of the hot working fluid exiting the recuperator (h_5) calculated previously from the measured temperature (T_5) and pressure (P_5) is equal to the specific enthalpy of the hot fluid at the last node of the heat exchanger:

$$h_{rec,h,6} = h_5 \tag{3.15}$$

The specific enthalpies of the hot stream at the interface of each segment are calculated using an energy balance. The rate of heat transfer within each segment is computed according to:

$$\dot{Q}_{rec,i} / \dot{m}_{2nd} = h_{rec,c,i+1} - h_{rec,c,i} \qquad i = 0...5 \tag{3.16}$$

and the specific enthalpy of the hot stream is computed according to:

$$h_{rec,h,i} = \dot{Q}_{rec,i} / \dot{m}_{2nd} + h_{rec,h,i+1} \qquad i = 0...5 \quad (3.17)$$

The pressures along the hot side of the recuperator (from P_4, which is calculated using Eq. (4.33), to P_5, which is directly measured) are assigned so that the pressure drop within each section is proportional to the pressure drop calculated using the pressure drop correlation discussed in Chapter 4 (Eq. (4.34)-(4.35)); the pressure drops are each scaled so that the overall pressure drop is consistent with the measured value. The temperatures of the hot stream at each node are calculated from the specific enthalpy and pressure using the appropriate REFPROP correlations:

$$T_{rec,h,i} = temperature(h_{rec,h,i}, P_{rec,h,i}, \bar{y}_{rec}) \qquad i = 0...5 \quad (3.18)$$

3.3.3 Numerical Analysis of Each Recuperator Section

The properties at each measurement location within the recuperator have been calculated. However, the properties of the fluid within each of the six sections are not constant. Therefore, each of the six small heat exchangers that lie between the measurement sections must be further divided into a number of sub-heat exchangers (N_{rec}), as shown in Figure 3-5(b). The rate of heat transfer within each sub-section is taken to be an equal fraction ($1/N_{rec}$) of the total rate of heat transfer that occurs between the appropriate sensors in Figure 3-5(b). As the number of sub-heat exchangers used in the simulation increases, the assumption of constant properties within each sub-heat exchanger improves.

The specific enthalpy, pressure, and temperature of the hot and cold mixture at the first node of each discrete section are equal to the specific enthalpy, pressure, and temperature calculated at the interfaces of the six larger sections:

$$h_{recsub,h,0,i} = h_{rec,h,i} \qquad i = 0...5,\ j = 1...N_{rec} - 1 \quad (3.19)$$

$$h_{recsub,c,0,i} = h_{rec,c,i} \qquad i = 0...5,\ j = 1...N_{rec} - 1 \quad (3.20)$$

$$P_{recsub,h,0,i} = P_{rec,h,i} \qquad i = 0...5,\ j = 1...N_{rec} - 1 \quad (3.21)$$

$$P_{recsub,c,0,i} = P_{rec,c,i} \qquad i = 0...5,\ j = 1...N_{rec} - 1 \quad (3.22)$$

$$T_{recsub,h,0,i} = T_{rec,h,i} \qquad i = 0...5,\ j = 1...N_{rec} - 1 \quad (3.23)$$

$$T_{recsub,c,0,i} = T_{rec,c,i} \qquad i = 0...5,\ j = 1...N_{rec} - 1 \quad (3.24)$$

The specific enthalpy, pressure, and temperature of the hot and cold mixture at the final node for each of the six sections are equal to the specific enthalpy, pressure, and temperature calculated at the interface of the next large section:

$$h_{recsub,h,Nrec,i} = h_{rec,h,i+1} \qquad i = 0...5,\ j = 1...N_{rec} - 1 \quad (3.25)$$

$$h_{recsub,c,Nrec,i} = h_{rec,c,i+1} \qquad i = 0...5,\ j = 1...N_{rec} - 1 \quad (3.26)$$

$$P_{recsub,h,Nrec,i} = P_{rec,h,i+1} \qquad i = 0...5,\ j = 1...N_{rec} - 1 \quad (3.27)$$

$$P_{recsub,c,Nrec,i} = P_{rec,c,i+1} \qquad i = 0...5,\ j = 1...N_{rec} - 1 \quad (3.28)$$

$$T_{recsub,h,Nrec,i} = T_{rec,h,i+1} \qquad i = 0...5,\ j = 1...N_{rec} - 1 \quad (3.29)$$

$$T_{recsub,c,Nrec,i} = T_{rec,c,i+1} \qquad i = 0...5,\ j = 1...N_{rec} - 1 \quad (3.30)$$

The specific enthalpy of the hot and cold mixture of each discrete node is calculated using an energy balance as shown in Figure 3-5(c):

$$h_{recsub,h,j,i} = h_{recsub,h,j-1,i} - \frac{\dot{Q}_{rec,i} / \dot{m}_{2nd}}{N_{rec}} \qquad i = 0...5,\ j = 1...N_{rec} - 1 \quad (3.31)$$

$$h_{recsub,c,j,i} = h_{recsub,c,j-1,i} - \frac{\dot{Q}_{rec,i} / \dot{m}_{2nd}}{N_{rec}} \qquad i = 0...5,\ j = 1...N_{rec} - 1 \quad (3.32)$$

The total pressure drop is assumed to occur equally across each of the sub-sections:

$$\Delta P_{recsub,h,i} = \frac{P_{rec,h,i} - P_{rec,h,i+1}}{N_{rec}} \qquad i = 0...5 \quad (3.33)$$

$$\Delta P_{recsub,c,i} = \frac{P_{rec,c,i+1} - P_{rec,c,i}}{N_{rec}} \qquad i = 0...5 \quad (3.34)$$

$$P_{recsub,h,j,i} = P_{recsub,h,j-1,i} - \Delta P_{recsub,h,i} \qquad i = 0...5,\ j = 1...N_{rec} - 1 \quad (3.35)$$

$$P_{recsub,c,j,i} = P_{recsub,c,j-1,i} + \Delta P_{recsub,c,i} \qquad i = 0...5,\ j = 1...N_{rec} - 1 \quad (3.36)$$

The temperature distribution is computed based on the specific enthalpy and pressure at each node:

$$T_{recsub,h,j,i} = temperature(h_{recsub,h,j,i}, P_{recsub,h,j,i}, \bar{y}_{rec}) \qquad i = 0...5,\ j = 1...N_{rec} - 1 \quad (3.37)$$

$$T_{recsub,c,j,i} = temperature(h_{recsub,c,j,i}, P_{recsub,c,j,i}, \bar{y}_{rec}) \qquad i = 0...5,\ j = 1...N_{rec} - 1 \quad (3.38)$$

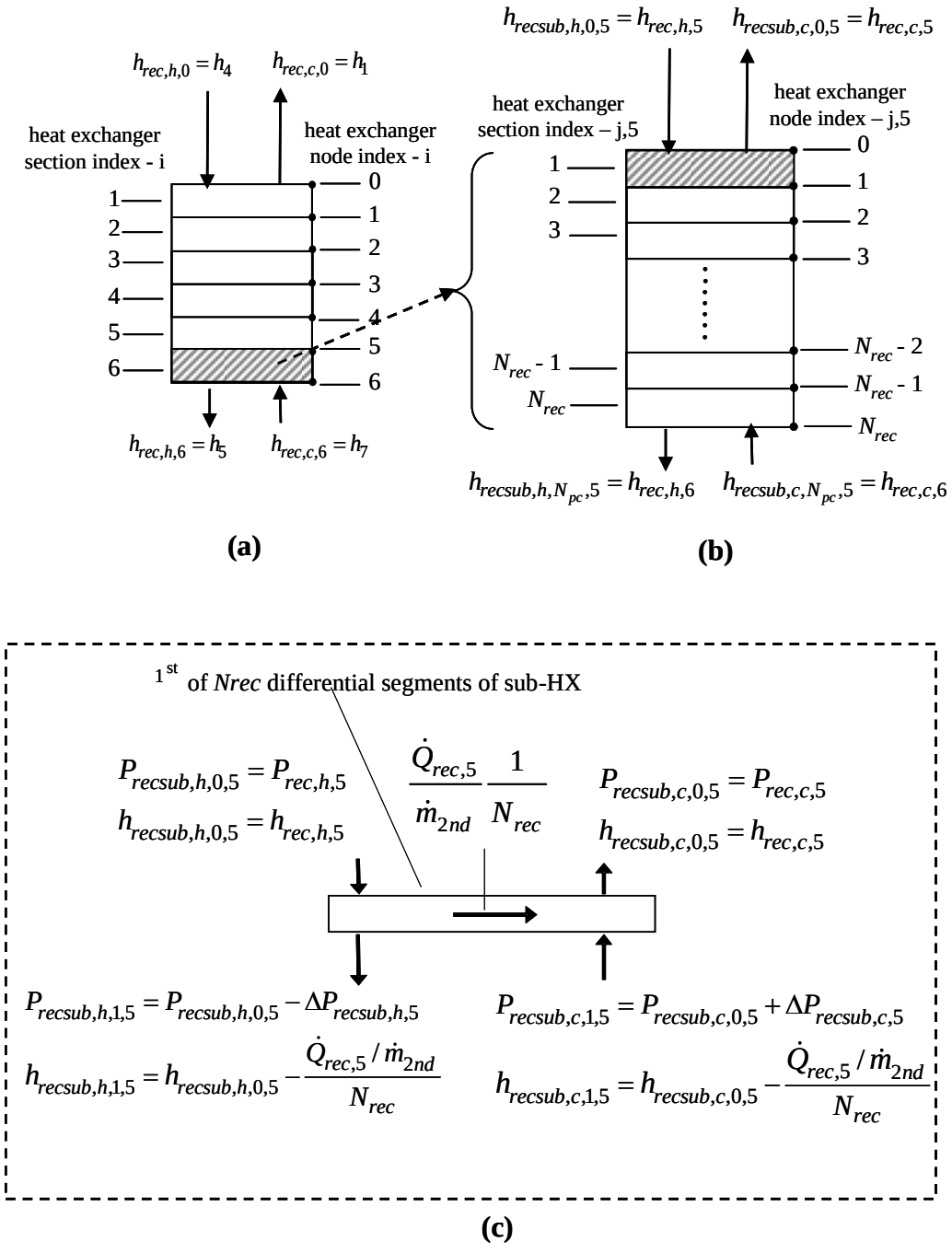

Figure 3-5: (a) Recuperating heat exchanger divided into six segments. (b) Last of six larger segments divided into N_{rec} subsections. (c) First subsection of larger segment number six. (Adapted from Skye 2011)

3.3.4 Calculating the Recuperator Conductance

The conductance of the recuperator (UA_{rec}) can be calculated by summing the conductances of the sub-heat exchanger sections. These conductances are determined using the effectiveness-*NTU* method for a counterflow heat exchanger, assuming that the specific heat capacity of the fluid on both sides of the heat exchanger is constant. The specific heat capacity of the refrigeration mixture varies significantly as it passes through the heat exchanger. However, by dividing the heat exchanger into a large number of small sections (N_{rec}), the assumption of constant specific heat capacity in each of these sub-sections is justified. The total heat exchanger conductance can then be calculated by summing the conductances of the smaller sections. The average specific heat capacity of the fluid within each discrete section is computed according to:

$$\overline{c}_{recsub,h,j,i} = \frac{h_{recsub,h,j-1,i} - h_{recsub,h,j,i}}{\left(T_{recsub,h,j-1,i} - T_{recsub,h,j,i}\right)} \qquad i = 0...5,\ j = 1...N_{rec} \quad (3.39)$$

$$\overline{c}_{recsub,c,j,i} = \frac{h_{recsub,c,j-1,i} - h_{recsub,c,j,i}}{\left(T_{recsub,c,j-1,i} - T_{recsub,c,j,i}\right)} \qquad i = 0...5,\ j = 1...N_{rec} \quad (3.40)$$

The minimum and maximum capacitance rates for each section are calculated according to:

$$\dot{C}_{recsub,min,j,i} = \min\left(\overline{c}_{recsub,h,j,i}, \overline{c}_{recsub,c,j,i}\right)\ \dot{m}_{2nd} \qquad i = 0...5,\ j = 1...N_{rec} \quad (3.41)$$

$$\dot{C}_{recsub,max,j,i} = \max\left(\overline{c}_{recsub,h,j,i}, \overline{c}_{recsub,c,j,i}\right)\ \dot{m}_{2nd} \qquad i = 0...5,\ j = 1...N_{rec} \quad (3.42)$$

The effectiveness of each discrete segment ($\varepsilon_{j,i}$) is defined as the ratio of actual rate of heat transfer to the maximum possible rate of heat transfer in that section. The maximum rate of heat transfer occurs when the outlet temperature associated with the

flow that has the minimum capacitance rate achieves the inlet temperature of the flow associated with the maximum capacity rate:

$$\varepsilon_{recsub,j,i} = \frac{\frac{\dot{Q}_{rec,i} / \dot{m}_{2nd}}{N_{rec}}}{\left(\min\left(\bar{c}_{recsub,c,j,i},\ \bar{c}_{recsub,h,j,i}\right)\ \left(T_{recsub,h,j-1,i} - T_{recsub,c,j,i}\right)\right)} \quad i = 0...5,\ j = 1...N_{rec} \qquad (3.43)$$

The conductance of each discrete section is calculated according to:

$$UA_{recsub,j,i} / \dot{m}_{2nd} = \min\left(\bar{c}_{recsub,c,j,i}, \bar{c}_{recsub,h,j,i}\right) \left(\frac{\ln\left(\frac{\varepsilon_{recsub,j,i} - 1}{\varepsilon_{recsub,j,i} \cdot C_{r,recsub,j,i} - 1} \right)}{C_{r,recsub,j,i} - 1} \right) \quad \begin{matrix} i = 0...5 \\ j = 1...N_{rec} \end{matrix} \qquad (3.44)$$

where $C_{r,rec,j,i}$ is the capacity ratio characterizing the section:

$$C_{r,recsub,j,i} = \frac{\dot{C}_{recsub,min,j,i}}{\dot{C}_{recsub,max,j,i}} \qquad i = 0...5,\ j = 1...N_{rec} \qquad (3.45)$$

The overall conductance of the recuperator is computed by summing the conductances of all of the discrete segments.

$$UA_{rec} / \dot{m}_{2nd} = \sum_{i=1}^{6} \sum_{j=1}^{N_{rec}} UA_{recsub,j,i} / \dot{m}_{2nd} \qquad (3.46)$$

Note that the conductance of each of the six sections that lie between the measurement locations can be separately computed based on this technique; this calculation allows some spatial resolution of the total conductance measurement.

3.4 1st Stage Analysis

The process for analyzing the precooling evaporator begins by assuming an isenthalpic expansion across the 1st stage valve:

$$h_{11} = h_{10} \tag{3.47}$$

The pressure drop across the condenser is assumed to be negligible so that the pressures at the inlet and outlet of the condenser (P_9 and P_{10}) are equal.

$$P_9 = P_{10} \tag{3.48}$$

The specific enthalpy of the fluid entering the precooler can then be calculated according to:

$$h_{10} = enthalpy(T_{10}, P_{10}, \bar{y}_{10}) \tag{3.49}$$

where *enthalpy* represents using the appropriate correlations in REFPROP or EES to evaluate the specific enthalpy at the given state (Lemmon 2007). An energy balance on the gas mix side of the precooler is used to calculate the total rate of heat transfer:

$$\dot{Q}_{pc} = \left(h_3 - h_4\right) \cdot \dot{m}_{2nd} \tag{3.50}$$

The specific enthalpy (h_8) at the cold outlet of the heat exchanger is computed using an energy balance on the 1st stage side of the precooler:

$$h_8 = h_{11} + \dot{Q}_{pc} \big/ \dot{m}_{1^{st}} \tag{3.51}$$

where $\dot{m}_{1st}$ is the mass flow rate measured in the 1st stage of the cycle.

The precooling evaporator is divided into a number (N_{pc}) of smaller sections each with equal heat transfer rates, as shown in Figure 3-6(a). As with the 2nd stage analysis, dividing the precooler into small sections improves the assumption of constant properties

within each section and therefore allows the application of the ε-*NTU* solution to each section. The first segment is located at the hot end of the precooler, as shown in Figure 3-6(b). The specific enthalpy of the first node for the 2nd stage side of the heat exchanger is equal to the specific enthalpy at the 2nd stage inlet (h_3).

$$h_{2nd,pc,0} = h_3 \tag{3.52}$$

The specific enthalpy of the 1st stage final node is equal to the specific enthalpy calculated at the 1st stage inlet (h_{11}).

$$h_{1st,pc,N} = h_{11} \tag{3.53}$$

An energy balance on each segment is used to calculate the specific enthalpies at each node on both sides of the precooling heat exchanger, as shown in Figure 3-6(b):

$$h_{2nd,pc,i} = h_{2nd,pc,i-1} - \frac{\dot{Q}_{pc} / \dot{m}_{2nd}}{N_{pc}} \qquad i = 1...N_{pc} \tag{3.54}$$

$$h_{1st,pc,i} = h_{1st,pc,i-1} - \frac{\dot{Q}_{pc/m} / \dot{m}_{1st}}{N_{pc}} \qquad i = 1...N_{pc} \tag{3.55}$$

The pressure on the 1st stage side of the precooler can be assumed to be constant, as there is a relatively large flow passage between the fins of the heat exchanger. This flow restriction is negligible in comparison to the pressure difference across the precooler cycle jewel orifice.

$$P_{1st,pc,i} = P_8 \qquad i = 0...N_{pc} \tag{3.56}$$

The 2nd stage pressure is assumed to vary in a manner that is proportional to the pressure drop calculated using the correlation, as explained in Chapter 4. Again, the pressure

calculated using the pressure drop model is scaled so that the measured and predicted total pressure drops agree. The pressure at the first node is equal to the measured pressure at the 2nd stage inlet (P_3).

$$P_{2nd,pc,0} = P_3 \tag{3.57}$$

The R410a working fluid in the precooling evaporator is in a saturated state; therefore, it will evaporate at a nearly constant temperature while exchanging heat with the 2nd stage fluid. The evaporation temperature can be computed using the temperature at the 1st stage inlet (T_{11}), which is calculated assuming isenthalpic expansion and the 1st stage exit pressure (P_8). Alternatively, the temperature on the 1st stage side of the precooler can be set equal to the measured outlet temperature (T_8). These two estimates of the temperatures vary by only approximately 1 K. Here, the temperatures of all nodes on the 1st stage side are set equal to the measured outlet temperature:

$$T_{1st,pc,i} = T_8 \qquad i = 0...N_{pc} \tag{3.58}$$

The temperature of the first node of the 2nd stage ($T_{2nd,pc,0}$) is equal to the measured 2nd stage inlet temperature (T_3).

$$T_{2nd,pc,0} = T_3 \tag{3.59}$$

With all 2nd stage specific enthalpies and pressures determined, the temperature distribution on the 2nd stage side of the precooler is calculated using the appropriate REFPROP property relation:

$$T_{2nd,pc,i} = Temperature(h_{2nd,pc,i}, P_{2nd,pc,i}, \bar{y}_{pc}) \qquad i = 1...N_{pc} \tag{3.60}$$

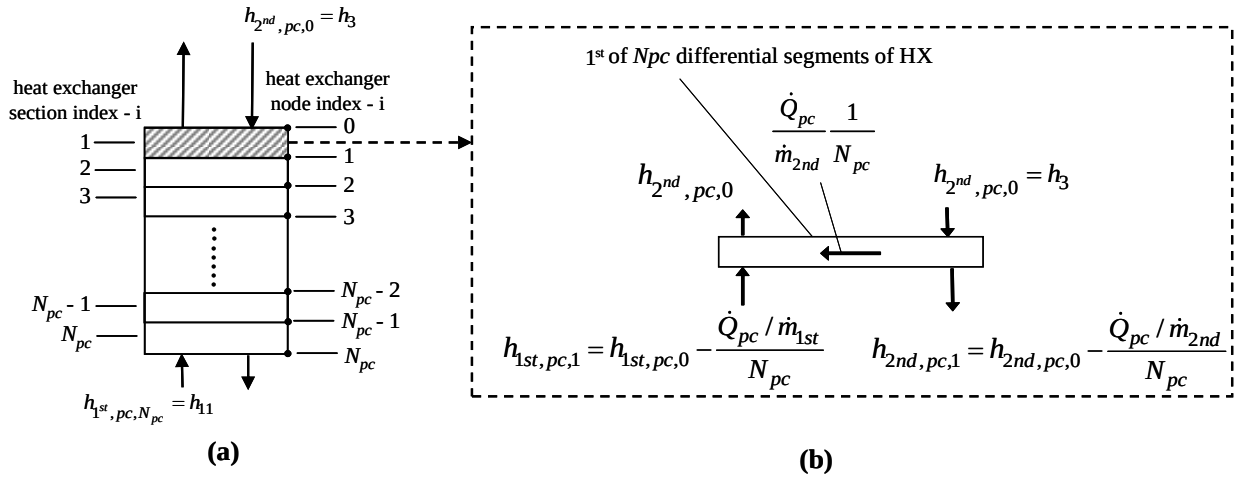

Figure 3-6: (a) Precooling heat exchanger divided into N_{pc} sections and $N_{pc}+1$ nodes. (b) First heat exchanger element. (Adapted from Skye 2011)

The conductance of the precooling evaporator (UA_{pc}) is calculated utilizing the same method that was applied to the recuperator model. The heat exchanger is broken into a number of small heat exchanger segments (N_{pc}) over which the temperature change is small and the heat capacity is nearly constant; therefore, the effectiveness-*NTU* relationship can be applied to each of the sections in order to compute the conductance. The conductance is calculated for a number of discrete segments with a mean specific heat capacity and summed to find the total conductance of the precooling heat exchanger. The average specific heat capacity of each section is defined as:

$$\bar{c}_{2nd,pc,i} = \frac{h_{2nd,pc,i-1} - h_{2nd,pc,i}}{T_{2nd,pc,i-1} - T_{2nd,pc,i}} \qquad i = 1...N_{pc} \quad (3.61)$$

$$\bar{c}_{1st,pc,i} = \frac{h_{1st,pc,i-1} - h_{1st,pc,i}}{T_{1st,pc,i-1} - T_{1st,pc,i}} \qquad i = 1...N_{pc} \quad (3.62)$$

Note that when the 1st stage is operated with a pure fluid, there will be an infinitely small temperature difference (here assumed to be zero) across each section, and therefore the mean specific heat capacity will be infinitely large. The capacitance rates are calculated as follows:

$$\dot{C}_{pc,min,i} = \min\left(\bar{c}_{2nd,pc,i}\ \dot{m}_{2nd}\,,\ \bar{c}_{1st,pc,i}\ \dot{m}_{1st}\right) \qquad i = 1...N_{pc} \quad (3.63)$$

$$\dot{C}_{pc,max,i} = \max\left(\bar{c}_{2nd,pc,i}\ \dot{m}_{2nd}\,,\ \bar{c}_{1st,pc,i}\ \dot{m}_{1st}\right) \qquad i = 1...N_{pc} \quad (3.64)$$

The capacity ratio, which will be effectively zero due to the large specific heat capacity of the 1st stage when it is operated with a pure fluid, is defined to be:

$$C_{r,pc,i} = \frac{\dot{C}_{pc,min,i}}{\dot{C}_{pc,max,i}} \qquad i = 1...N_{pc} \quad (3.65)$$

The effectiveness of each section is then calculated as in the recuperator models:

$$\varepsilon_{pc,i} = \frac{\dot{Q}_{pc} / (N_{pc} \cdot \dot{m}_{2nd})}{\left(min\left(\bar{c}_{2nd,pc,i}\,,\ \bar{c}_{1st,pc,i}\right) \cdot \left(T_{2nd,pc,i-1} - T_{1st,pc,i}\right)\right)} \quad i = 1...N_{pc} \quad (3.66)$$

The calculated effectiveness in turn determines the conductance of each discrete segment of the precooler.

$$UA_{pc,i} / \dot{m}_{2nd} = \min\left(\bar{c}_{1st,pc,i}\,,\ \bar{c}_{2nd,pc,i}\right) \left(\frac{\ln\left(\frac{\varepsilon_{pc,i} - 1}{\varepsilon_{pc,i} \cdot C_{r,pc,i} - 1} \right)}{C_{r,pc,i} - 1} \right) \quad i = 1...N_{pc} \quad (3.67)$$

The total conductance is calculated by summing the individual conductances of the segments:

$$UA_{pc} = \sum_{i=1}^{N_{pc}} UA_{pc,i} \tag{3.68}$$

3.5 References

Ely, J. F. and Huber, M. L. NIST Thermophysical Properties of Hydrocarbon Mixtures Database (SUPERTRAPP). 1992, *3.2*.

Klein, S. A. EES - Engineering Equation Solver. 2012, *9.032*, f-Chart Software, http://fchart.com.

Klein, S.A., EES-NIST4 interface routine, f-Chart Software, http://fchart.com, 2008.

Lemmon, E. W.; Huber, M. L.; McLinden, M. O. NIST Reference Fluid Thermodynamic and Transport Properties - REFPROP. 2007, 8.0. More information available at http://www.nist.gov/srd/nist23.cfm.

Skye, H.M. 2011. Modeling, Experimentation and Optimization for a Mixed-Gas Joule-Thomson Cycle with Precooling for Cryosurgery. PhD thesis. Madison, WI USA: University of Wisconsin – Madison, Mechanical Engineering Department.

4 Pressure Drop Model

4.1 Justification

As discussed in Section 3.3.1, Skye's model (2011) assumed the pressure at the hot-side recuperator inlet (P_4) to be the average of the hot-side inlet pressure of the precooler (P_3) and the pressure at the hot-side outlet of the recuperator (P_5):

$$P_4 = \frac{\left(P_3 + P_5\right)}{2} \tag{4.1}$$

The length of tube through which the mixed gas must flow in the 2nd stage side of the precooler is about half the length of the hot side of the recuperator, and the inner tube diameters are the same. However, since the refrigerant is mostly vapor as it flows through the precooler, it has a higher velocity. With the countering effects of the differing lengths and velocities, it is not unreasonable to expect the average of P_3 and P_5 to be a good approximation for P_4.

However, it is apparent from this discussion that the assumption of linear pressure variation and, more importantly, the assumption of equal pressure drop between the recuperator and the precooler is rather crude. As shown in Figure 3-3, there is significantly increased heat transfer within the vapor dome as the mixture passes into the recuperator. In this region, the isotherms are more horizontal relative to the isotherms outside the vapor dome. Therefore, changing the assumed pressure at state 4 could drastically affect the temperatures predicted in the hot stream within the recuperator, and this in turn may have a large effect on the calculated conductance. Therefore, a pressure

drop model has been developed and integrated into the model as an additional improvement.

4.2 Two Phase Pressure Drop through Horizontal Tube

The Müller-Steinhagen and Heck two-phase pressure drop correlation is used to calculate the pressure drop through the precooling and recuperative heat exchangers (Didi 2001). For single-phase flow, the correlation simplifies to an appropriate single-phase pressure drop model (Müller-Steinhagen 1986). Generally, the pressure gradient for a horizontal tube is calculated as the sum of two contributions related to momentum and friction.

$$\Delta P = \Delta p_{mom} + \Delta p_{frict} \tag{4.2}$$

The momentum pressure drop (Δp_{mom}) is calculated according to:

$$\Delta p_{mom} = \dot{m}_{total}^2 \left\{ \left[\frac{(1-\chi)^2}{\rho_L (1-VF)} + \frac{\chi^2}{\rho_G \, VF} \right]_{out} - \left[\frac{(1-\chi)^2}{\rho_L (1-VF)} + \frac{\chi^2}{\rho_G \, VF} \right]_{in} \right\} \tag{4.3}$$

The void fraction *VF* is obtained from the Steiner version (1993) of the drift flux model of Rouhani and Axelsson for horizontal tubes (1970):

$$VF = \frac{\chi}{\rho_G} \left[\left(1 + 0.12(1-\chi)\right) \left(\frac{\chi}{\rho_G} + \frac{1-\chi}{\rho_L} \right) + \frac{1.18(1-\chi)\left[g\sigma(\rho_L - \rho_G) \right]^{0.25}}{m_{total}^2 \rho_L^{0.5}} \right]^{-1} \tag{4.4}$$

where $\dot{m}_{total}$ is the total mass flow rate of liquid plus vapor, χ represents the vapor quality, g is the acceleration due to gravity, σ is the surface tension, and the *L* and *G*

subscripts represent the liquid and vapor properties, respectively. The friction pressure drop (Δp_{frict}) is calculated according to:

$$\Delta p_{frict} = \left(G(1-\chi)^{1/3} + b\chi^3 \right) L \tag{4.5}$$

$$G = a + 2\left(b - a\right)\chi \tag{4.6}$$

where L is the tube length, and a and b are the frictional pressure gradients for all the flow liquid and all the flow vapor, respectively, given by the Chisholm correlation:

$$a = \left(\frac{dp}{dz} \right)_L = f_L \frac{2\dot{m}_{total}^2}{d\rho_L} \tag{4.7}$$

$$b = \left(\frac{dp}{dz} \right)_G = f_G \frac{2\dot{m}_{total}^2}{d\rho_G} \tag{4.8}$$

The liquid and vapor friction factors are calculated using the Friedel correlation (1979):

$$f_{L\ or\ G} = \frac{0.079}{\mathrm{Re}_{L\ or\ G}^{0.25}} \tag{4.9}$$

$$\mathrm{Re}_{L\ or\ G} = \frac{\dot{m}_{total} d}{\mu_{L\ or\ G}} \tag{4.10}$$

4.3 Precooling Evaporator

The precooling evaporator is divided into a number (N_{pc}) of smaller sections, each with equal heat transfer rates, as shown in Figure 3-6(a). The conditions at the inlet of the 2nd stage side are measured and used in other calculations, but all variable names are reassigned for the separate pressure drop calculations (indicated by an extra *p)*:

$$Pp_{2nd,pc,0} = P_{2nd,pc,0} \tag{4.11}$$

$$Tp_{2nd,pc,0} = T_{2nd,pc,0} \tag{4.12}$$

The enthalpies at each node on the 2nd stage side have been calculated in Eq. (3.54):

$$hp_{2nd,pc,i} = h_{2nd,pc,i} \qquad i = 1...N_{pc} \tag{4.13}$$

Starting with the first section, the enthalpy, temperature, and pressure are known at the inlet, and the enthalpy at the outlet is known. The correlation can be used to calculate the pressure drop for the first node. The outlet pressure ($Pp_{2nd,pc,1}$) is guessed, allowing the average properties of the node to be calculated:

$$\chi p_{pc,avg,1} = \frac{\chi\left(Pp_{2nd,pc,0}, hp_{2nd,pc,0}\right) + \chi\left(Pp_{2nd,pc,1,guess}, hp_{2nd,pc,1}\right)}{2} \tag{4.14}$$

$$\mu p_{L\ or\ G,pc,avg,1} = \frac{\mu_{L\ or\ G}\left(Pp_{2nd,pc,0}, hp_{2nd,pc,0}\right) + \mu_{L\ or\ G}\left(Pp_{2nd,pc,1,guess}, hp_{2nd,pc,1}\right)}{2} \tag{4.15}$$

$$\rho p_{L\ or\ G,pc,avg,1} = \frac{\rho_{L\ or\ G}\left(Pp_{2nd,pc,0}, hp_{2nd,pc,0}\right) + \rho_{L\ or\ G}\left(Pp_{2nd,pc,1,guess}, hp_{2nd,pc,1}\right)}{2} \tag{4.16}$$

These average properties are then used to calculate the momentum and friction pressure drops. The length L used to calculate the frictional pressure drop is given by:

$$L_{pc,i} = \frac{L_{pc}}{N_{pc}} \tag{4.17}$$

A more physical representation would calculate the length of each section by scaling the total length by the ratio of the *UA* of each section of length to the total *UA*:

$$L_{pc,i} = L_{pc} \frac{UA_{pc,i}}{UA_{pc}} \qquad i = 1...N_{pc} \qquad (4.18)$$

Implementing Eq. (4.18) as opposed to Eq. (4.17) changed the computed overall *UA* only by about one percent for those test conditions considered; therefore, Eq. (4.17) was used as it improved the overall convergence of the model. The predicted pressure at node 2 is calculated:

$$Pp_{2nd,pc,1} = Pp_{2nd,pc,0} - \Delta p_{mom} - \Delta p_{frict} \qquad (4.19)$$

However, since a guess value for the outlet pressure was used to calculate the average properties in the section, the calculated outlet pressure and guess pressure do not agree. Therefore, this procedure (Eq. (4.14)-(4.19)) is repeated, varying the guess value, until the outlet pressures agree and the true pressure drop for the section can be calculated:

$$Pp_{2nd,pc,1} = Pp_{2nd,pc,1,guess} \qquad (4.20)$$

$$\Delta P_{pc,calc,1} = Pp_{2nd,pc,0} - Pp_{2nd,pc,1} \qquad (4.21)$$

EES accomplishes this iteration automatically. At this point, the inlet condition to the second section is known, so the full pressure drop procedure (Eq. (4.14)-(4.21)) is repeated for each section until the pressure at the last node has been calculated. The total precooler pressure drop can then be determined by summing the pressure drops in each section:

$$\Delta P_{pc,calc} = \sum_{i=1}^{N_{pc}} \Delta P_{pc,calc,i} \qquad (4.22)$$

4.4 Recuperator

The recuperator is also divided into 6 sections corresponding to the locations of the experimental measurements (similar to Figure 3-4a). The pressure drop in each section is calculated in a manner similar to the precooler sections. However, in this case we know the state at the exit of the heat exchanger (state 5, as shown in Figure 3-1a).

$$Pp_{rec,h,6} = P_{rec,h,6} \tag{4.23}$$

$$Tp_{rec,h,6} = T_{rec,h,6} \tag{4.24}$$

The specific enthalpies on the hot side of the recuperator have been calculated using Eq. (3.17):

$$hp_{rec,h,i} = h_{rec,h,i} \tag{4.25}$$

Knowing the outlet state and the inlet enthalpy, the inlet pressure is guessed in order to calculate the thermal conductivity, viscosity and density at each node:

$$\chi p_{rec,avg,i} = \frac{\chi\left(Pp_{rec,i}, hp_{rec,i}\right) + \chi\left(Pp_{rec,i-1,guess}, hp_{rec,i-1}\right)}{2} \qquad i=1...6 \tag{4.26}$$

$$\mu p_{L\ or\ G,rec,avg,i} = \frac{\mu_{L\ or\ G}\left(Pp_{rec,i}, hp_{rec,i}\right) + \mu_{L\ or\ G}\left(Pp_{rec,i-1,guess}, hp_{rec,i-1}\right)}{2} \qquad i=1...6 \tag{4.27}$$

$$\rho p_{L\ or\ G,avg,i} = \frac{\rho_{L\ or\ G}\left(Pp_{rec,i}, hp_{rec,i}\right) + \rho_{L\ or\ G}\left(Pp_{rec,i-1,guess}, hp_{rec,i-1}\right)}{2} \qquad i=1...6 \tag{4.28}$$

The properties are then used to calculate the momentum and friction pressure drops from the Müller-Steinhagen correlation (Eq. (4.2)-(4.10)). The length of each section is known based on the evenly spaced experimental measurements.

$$L_{rec,i} = \frac{L_{rec}}{6} \qquad i = 1...6 \quad (4.29)$$

The inlet pressure guess is then varied until it agrees with the calculated inlet pressure.

$$Pp_{rec,i-1} = Pp_{rec,i} + \Delta p_{mom} + \Delta p_{frict} \qquad i = 1...6 \quad (4.30)$$

Finally, the pressure drop in each section is calculated and summed to determine the total pressure drop in the recuperator.

$$\Delta P_{rec,calc,i} = Pp_{rec,i-1} - Pp_{rec,i} \qquad i = 1...6 \quad (4.31)$$

$$\Delta P_{rec,calc} = \sum_{i=1}^{6} \Delta P_{rec,calc,i} \quad (4.32)$$

4.5 Integration into System Model

The calculated pressure drop tends to underpredict the experimentally measured pressure drop by an average of 25%, most likely due to the complicated heat exchanger geometry (see Figure 4-1). A more correct distribution of the pressure drop through each heat exchanger is estimated by scaling the calculated pressure drops so that their sum agrees with the experimentally measured pressure drop. First, P_4 is assigned such that the ratio of the calculated precooler pressure drop to the total calculated pressure drop is equal to the ratio of the same experimental parameters:

$$P_4 = P_3 - \frac{\Delta P_{pc,calc}}{\Delta P_{tot,calc}} \left(P_3 - P_5 \right) \quad (4.33)$$

Within the precooler, the pressures are scaled to agree with the ratio of the calculated section pressure drop to the total precooler pressure drop.

$$\Delta P_{2nd,pc,i} = \left(P_3 - P_4\right)\frac{\Delta P_{pc,calc,i}}{\Delta P_{pc,calc}} \qquad i = 1...N_{pc} \quad (4.34)$$

$$P_{2nd,pc,i} = P_{2nd,pc,i-1} - \Delta P_{2nd,pc,i} \qquad i = 1...N_{pc} \quad (4.35)$$

The pressures along the hot side of the recuperator can then be assigned to be proportional to the pressures calculated using the pressure drop correlation. The pressures of the subsections between the experimental measurements are assumed to be linear as described by Eq. (3.33).

$$\Delta P_{rec,h,i} = \left(P_4 - P_5\right)\left(\frac{\Delta P_{rec,calc,i}}{\Delta P_{rec,calc}}\right) \qquad i = 0...5 \quad (4.36)$$

$$P_{rec,h,i} = P_{rec,h,i-1} - \Delta P_{rec,h,i} \qquad i = 0...5 \quad (4.37)$$

4.6 Pressure Drop Model Results/Discussion

This pressure drop model creates a more physics-based prediction of the conductance in the optimization model. However, the pressure drop predicted by the model generally underpredicts the experimental pressure drop by about 25%, with higher disagreement evident with higher experimental pressure drops (see Figure 4-1). Therefore, scaling the calculated section pressure drops to agree with the total experimental pressure drop is necessary. Worse agreement is also seen for mixtures with a large percentage of R23, suggesting a disagreement between the predicted and observed property data (Müller-Steinhagen 1986). In general, the pressure predicted at state 4 only changes an average of 5%. However, as seen in Figure 4-2, the change in calculated

conductance is much larger. The average change in recuperator conductance is 10%, and the change is even more significant for two-phase experimental data.

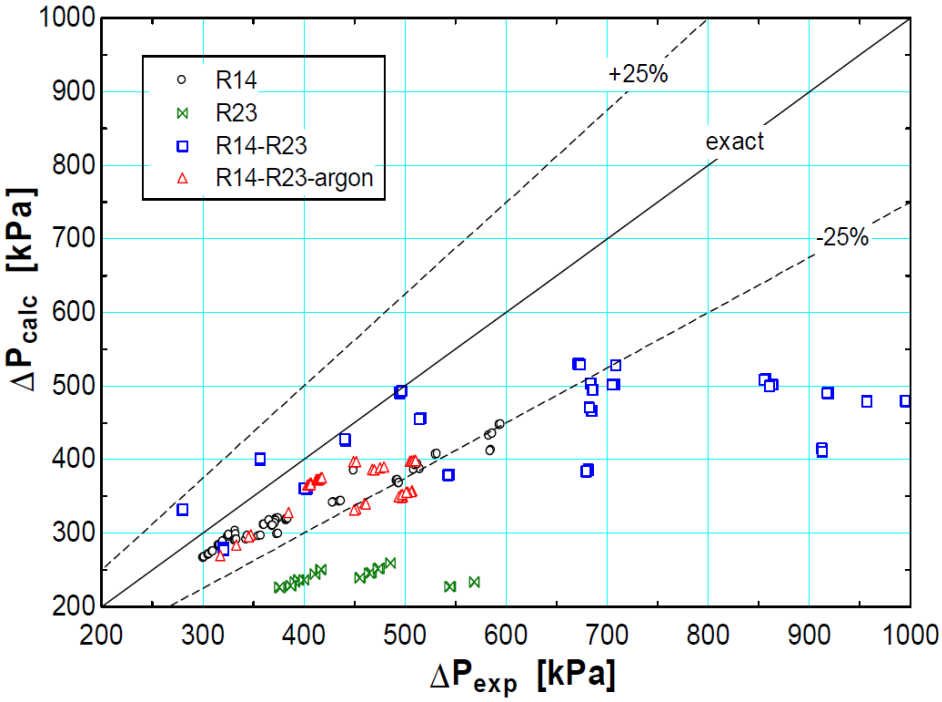

Figure 4-1: Comparison between pressure drop measured in experiment (from state 3 to 5) and pressure drop predicted by model for various mixture compositions.

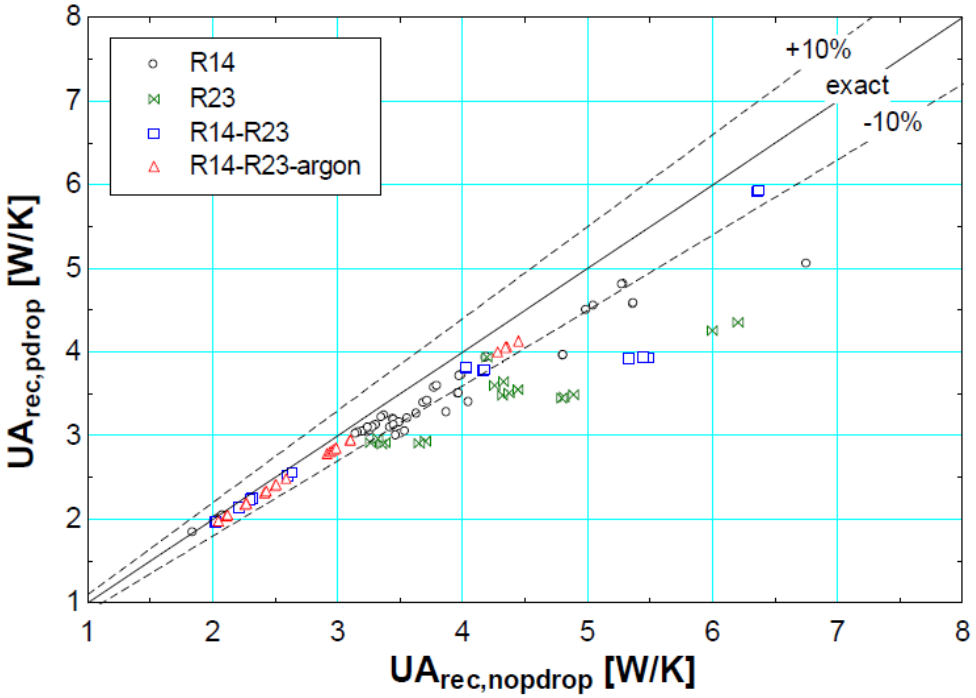

Figure 4-2: Comparison between recuperator conductance computed with and without the pressure drop model.

4.7 References

Didi, M.B., Kattan, N., and Thome, J.R. Prediction of two-phase pressure gradients of refrigerants in horizontal tubes. *International Journal of Refrigeration* 2001; 25:935-947.

Ely, J. F. and Huber, M. L. NIST Thermophysical Properties of Hydrocarbon Mixtures Database (SUPERTRAPP). 1992, *3.2*.

Friedel L. Improved friction pressure drop correlations for horizontal and vertical two-phase pipe flow. European Two-Phase Flow Group Meeting, Paper E2; 1979 June; Ispra, Italy.

Müller-Steinhagen H, Heck K. A simple friction pressure drop correlation for two-phase flow in pipes. *Chem Eng Process* 1986; 20:297-308.

Rouhani Z, Axelsson E. Calculation of void volume fraction in the subcooled and quality boiling regions. *Int J Mass Heat Transfer* 1970; 13:383-93.

Steiner D, VDI-Wärmeatlas (VDI Heat Atlas), Verein Deutscher Ingenieure, VDI-Gesellschaft Verfahrenstechnik und Chemieingenieurwesen (GCV), Düsseldorf 1993, Chapter Hbb.

Skye, H.M. 2011. Modeling, Experimentation and Optimization for a Mixed-Gas Joule-Thomson Cycle with Precooling for Cryosurgery. PhD thesis. Madison, WI USA: University of Wisconsin – Madison, Mechanical Engineering Department.

5 Reformulation of Empirical Model

The first generation empirical model was developed by Skye to predict the performance of the complex precooled MGJT cryoprobe system using the experimental data (see Chapters 5 and 6, Skye 2011). Implementing the pressure drop model changed the data processing results by improving the pressure prediction at state 4 (see Figure 3-1 for cycle schematic) and at discrete points within both the precooler and recuperator. The updated precooler and recuperator correlations are presented in the following sections (5.1-5.4).

5.1 Pressure Drop

The existing empirical model calculates the pressure drops in the recuperator and the precooler as follows (Section 5.4.7, Skye 2011): The pressure drop on the cold side of the recuperator is computed directly using the measurements at state 7 and 1. The pressure drops through the hot sides of the recuperator and precooler are assumed to be equal, computed using the measured pressures at states 3 and 5 and the predicted averaged pressure at state 4. The pressure drop is assumed to be dominated by the vapor phase flow at the warm end, where low densities and high velocities cause large frictional losses. In this case, the pressure drop in the recuperator is approximately correlated to $1/2\,\rho v^2$ at the hot side recuperator inlet and cold side outlet, drawing from the form of existing single phase pressure drop correlations for tubes:

$$\Delta P = f\left(Re, e, d\right)\frac{\rho v^2}{2}\frac{L}{d} \tag{5.1}$$

where ΔP is the pressure drop, f is the friction factor (which is a function of Reynolds number *Re*, tube roughness *e*, and diameter *d*), ρ is the density, *v* is the velocity, and *L* is the flow passage length.

Implementing the pressure drop procedure as described in Chapter 4 into the simulation model as an improvement to the simplified correlation described above increases the computational time by more than a factor of ten. Additionally, when the existing data points are used to verify the model, many runs have convergence issues and iterate to non-physical values; for runs that do converge, the results are not significantly different than the results from the dynamic head correlation. As a result, the pressure drop procedure is not directly implemented in the simulation model, and the correlations described in the following sections are used instead. However, since these correlations are created using the data processed using the pressure drop procedure, they represent a more physics-based prediction of the intermediate pressure between the precooler and recuperator.

5.1.1 Recuperator Pressure Drop

Since states 7 and 1 are directly measured, the cold side recuperator pressure drop model remains the same as in Skye 2011. With the improved prediction of the pressure at state 4 as described in Chapter 4, the hot side recuperator pressure drop model must be revised. Figure 5-1 shows the updated hot side pressure drop data with a linear curve fit. Table 5-1 summarizes the curve fit parameters and correlation statistics for both the new

correlation with the pressure drop implemented (unshaded) and the former correlation (shaded) for comparison. Similar to the previous empirical correlation (see Section 6.1, Skye 2011), the velocity and pressure drop terms do not extrapolate to zero together as expected as the velocity goes to zero; however, the curve does fit the empirical behavior shown in the data and is used to predict the pressure drop in the simulation model.

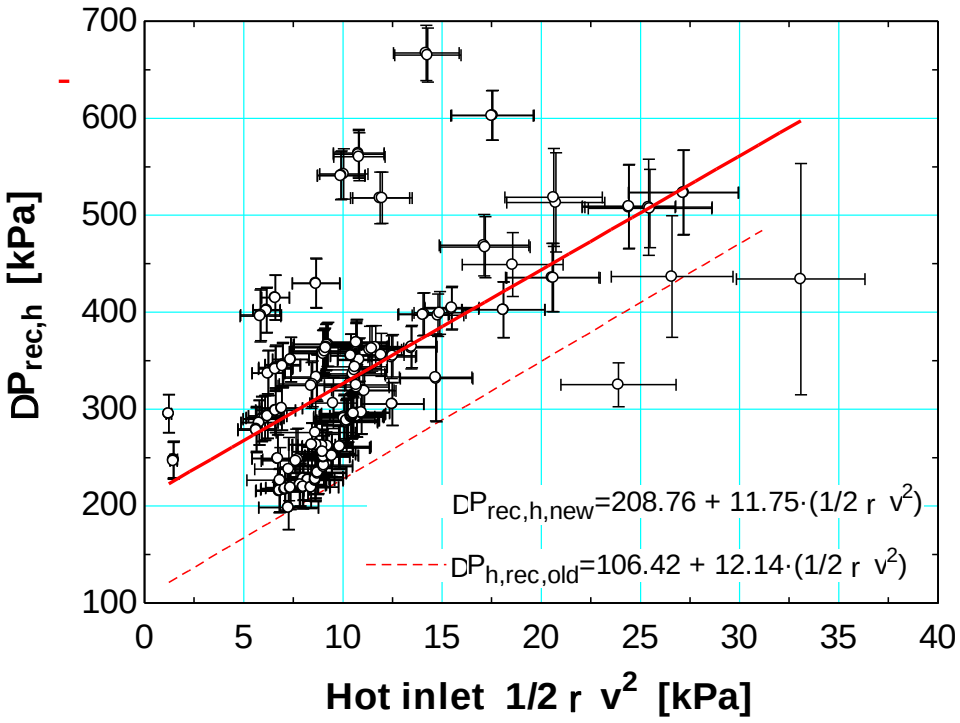

Figure 5-1: Recuperator pressure drop empirical correlation for hot stream of the recuperator showing fits both with and without the pressure drop model.

Table 5-1: Recuperator pressure drop correlation coefficients and curve fit statistics for (a) the hot side with the pressure drop model, (b) the hot side without the pressure drop model (Skye 2011), and (c) the cold side (Skye 2011).

Correlation form	a_0 **[kPa]**	a_1 **[-]**	**RMS error [kPa]**	R^2	N_{points}
(a) $\Delta P_{rec,h} = a_0 + a_1\left(1/2\,\rho_{rec,h,in}\,v^2_{rec,h,in}\right)$ with pressure drop model	208.78	11.748	78.0	0.35	198
(b) $\Delta P_{rec,h} = a_0 + a_1\left(1/2\,\rho_{pc,in}\,v^2_{pc,in}\right)$ without pressure drop model	106.42	12.14	50.0	0.61	198
(c) $\Delta P_{rec,c} = a_0 + a_1\left(1/2\,\rho_{rec,c,out}\,v^2_{rec,c,out}\right)$	31.93	1594.39	4.78	0.62	198

5.1.2 Precooler Pressure Drop

With the pressure drop model implemented in the data processing code, the precooler hot side pressure drop is no longer assumed to be equal to the recuperator hot side pressure drop. Instead, a separate correlation that predicts the precooler pressure drop based on the outlet conditions is formulated. Figure 5-2 shows the new hot side precooler pressure drop data with a linear curve fit. Table 5-2 summarizes the curve fit parameters and correlation statistics. Note that for the precooler, the pressure drop extrapolates to zero as the velocity goes to zero. Unlike the complicated two-phase flow in the recuperator, the precooler data are mostly vapor phase flow, and the simple dynamic head correlation does a better job of predicting this behavior.

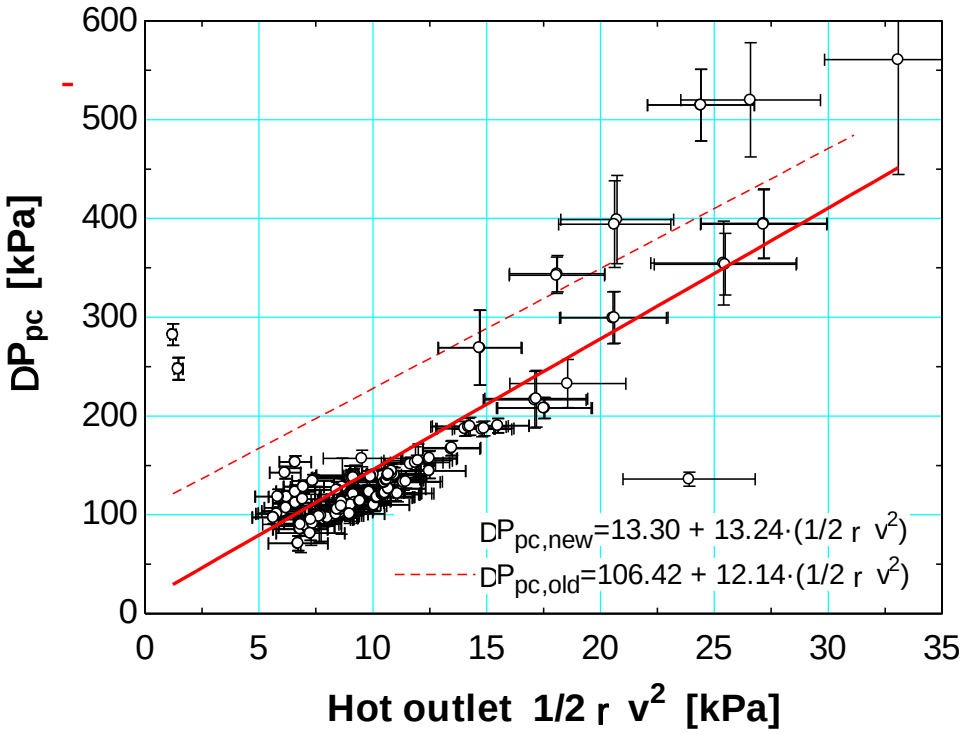

Figure 5-2: Precooler pressure drop as a function of the head loss; the linear best fits through these data represent the empirical correlation for the hot stream of the precooler both with and without the pressure drop model implemented.

Table 5-2: Precooler pressure drop correlation coefficients and curve fit statistics (a) with the pressure drop model implemented and (b) without the pressure drop model (Skye 2011).

Correlation form	a_0 [kPa]	a_1 [-]	RMS error [kPa]	R^2	N_{points}
(a) $\Delta P_{pc} = a_0 + a_1\left(1/2\,\rho_{pc,in}\,v_{pc,in}^2\right)$ with pressure drop model	13.301	13.241	52.4	0.60	198
(b) $\Delta P_{pc} = \Delta P_{rec,h} = a_0 + a_1\left(1/2\,\rho_{pc,in}\,v_{pc,in}^2\right)$ without pressure drop model	106.42	12.14	50.0	0.61	198

5.2 Recuperator Conductance

The conductance of each heat exchanger is a function of both the warm and cold side convective heat transfer coefficients and the conductive resistance in the tube walls and fins. Predicting the performance of the precooler and recuperator is complicated by the possibility of two-phase flow with a multi-component mixture in a complex heat exchanger geometry. Existing correlations for two-phase flow with pure fluids through simple geometries provide poor precision, with lowest possible uncertainties on the order of 25% (Timmerhaus 1989). With the complex system associated with a cryoprobe, the empirical correlations described here are vital to accurately predict system performance (see Section 6.6.2 of Skye 2011 for comparison to simpler pinch point and minimum isothermal enthalpy difference models). The addition of the pressure drop model in the data processing procedure gives a more physics-based estimate of the pressures at intermediate states in both heat exchangers and therefore of the total conductance compared with the previous pressure assumptions (see Chapter 4 for full discussion).

The conductance of the recuperator is largely a function of thermodynamic quality and mass flux, which are in turn influenced by the heat load, high and low pressures, and mixture composition. The heat transfer mechanisms for single and two-phase flow are significantly different, so the empirical conductance data is examined separately by flow regime prior to being combined into one recuperator conductance model.

5.2.1 Vapor Phase Conductance

Figure 5-3 shows vapor phase conductance normalized by length in each section as a function of the cold side Reynolds number. Figure 5-3(a) includes data with an uncertainty less than 40%, and Figure 5-3(b) includes all of the data. The conductance is normalized by length because the majority of the heat transfer occurs in the finned tubing (see Table 5-3 for lengths and types of tube in each section), and this normalization allows the correlation to be extended to designs with a variable finned tube length. Section 5 data is not included because this last section is significantly different from the other sections (it is relatively short and unfinned) and may also intercept radiation parasitic from the large conflat flange at the cold end of the cryoprobe sheath. The cold side Reynolds number is used as the correlating parameter because the cold side heat transfer coefficient is likely the limiting thermal resistance in the recuperator (Skye 2011, Section 5.2.1). The cold side Reynolds number is computed using the average cold side properties for the recuperator section.

(a)

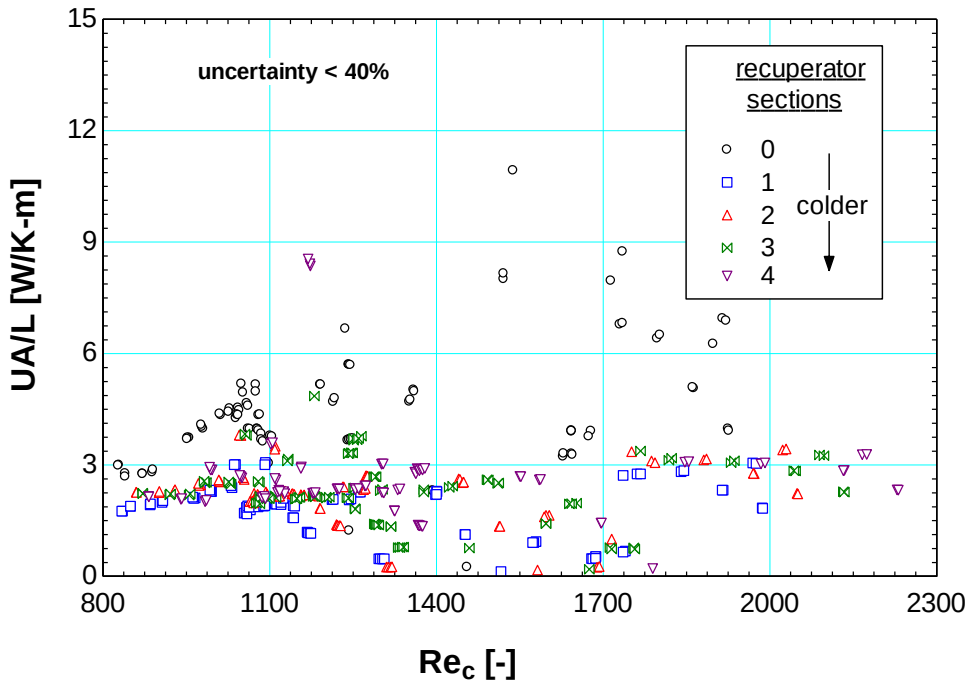

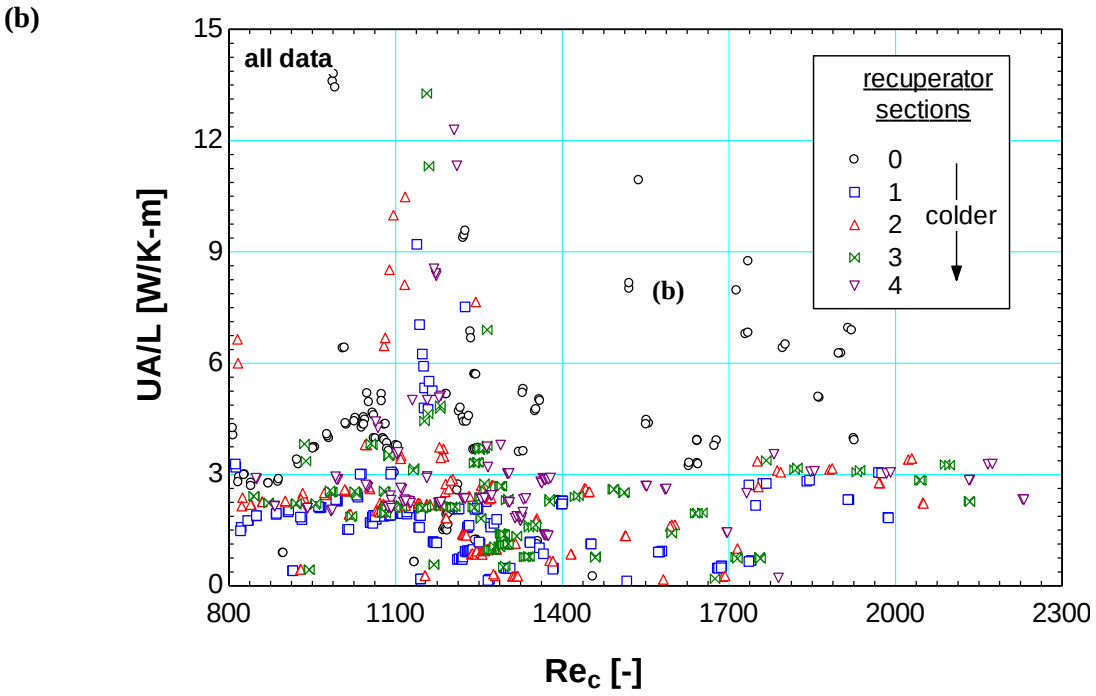

Figure 5-3: Vapor phase conductance measurements normalized by length of finned tube in recuperator sections 0-4 where (a) all data are shown, and (b) data with 40% or less uncertainty are shown. (Adapted from Skye 2011)

Table 5-3: Lengths of finned and smooth sections of tube in each recuperator section between the PRT centerlines (Skye 2011).

Section	Begin PRTs	End PRTs	axial length of finned tube [in]	length of finned tube [in]	length of smooth tube [in]
0	1	i1, i6	0.45	7.0	2.73
1	i1,i6	i2,i7	0.65	10.1	--
2	i2,i7	i3,i8	0.65	10.1	--
3	i3,i8	i4,i9	0.65	10.1	--
4	i4,i9	i5	0.56	8.7	0.97
5	i5	PRT 7	--	--	0.9

Figure 5-4 shows the recuperator conductance data filtered by uncertainty, where the red circles represent a threshold of 20% uncertainty, the blue circles include data with 40% uncertainty or less, and the black circles show the full data with no uncertainty constraint. The uncertainty filter significantly reduces the scatter in the data, but the uncertainty constraint must be balanced with the number of data points included and the RMS error value for the curve fit. A constant curve fit is chosen (with uncertainty < 40%), as a linear fit does not significantly improve the RMS error. Table 5-4 shows the statistics for both the new fits (including the pressure drop model improvement) and the old fits (Skye 2011). Note that more points can be used for the fit with the implementation of the pressure drop model due to better convergence and less instances of pinch point violation, where the hot side outlet temperature is colder than the cold side inlet temperature.

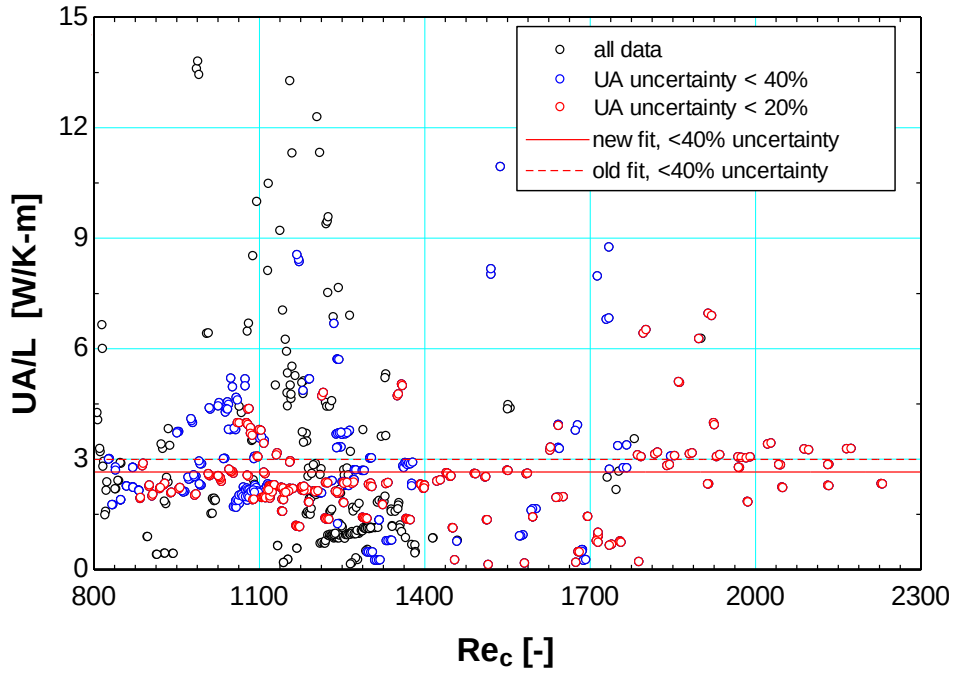

Figure 5-4: Recuperator vapor phase conductance data normalized by tube length as a function of Reynolds number sorted by uncertainty. Both the new and old constant fits are shown with <40% uncertainty. (Adapted from Skye 2011)

Table 5-4: Recuperator vapor phase conductance correlation coefficients and fit statistics (a) with the pressure drop model and (b) without the pressure drop model implemented (Skye 2011).

***UA/L* correlation**							
Correlation form	**Uncertainty Criteria**	***a*$_0$ [W/K-m]**	***a*$_1$ [W/K-m]**	**RMS error [W/K-m]**	**RMS error**	**R^2**	**N_{points}**
(a) $UA/L = a_0$ with pressure drop model	*UA/L* < 20%	2.423	--	1.096	41%	--	246
	UA/L < 40%	2.649	--	1.444	55%	--	447
	UA/L < 60%	2.493	--	1.513	57%	--	580
(b) $UA/L = a_0 + a_1$ without pressure drop model	*UA/L* < 20%	2.643	--	1.35	45%	--	235
	UA/L < 40%	2.993	--	1.579	53%	--	415
	UA/L < 60%	2.741	--	1.735	58%	--	533

5.2.2 Two-Phase Conductance

Figure 5-5(a) shows the conductance data normalized by length sorted by section as a function of the cold stream quality; note that section 0 is removed as a significant outlier for calculating the curve fit shown in Figure 5-5(b). This section contains a significant length of unfinned tube, and the space between the precooler shell and the outer sheath introduces an unknown heat transfer effect. Section 5 is also excluded as for the vapor phase conductance discussion because it is significantly different and may introduce radiation parasitic from the conflate flange. Figure 5-5(b) shows the length-normalized conductance data filtered by various uncertainties for sections 1-4 as a function of vapor quality. A third order fit is used for the data with < 80% uncertainty; the fit is forced to pass through the constant vapor value (2.649 W/K-m) at a quality of one, creating a continuous function. Table 5-5 shows the fit statistics for the curve fit with varying levels of uncertainty both with and without the pressure drop model implemented. The 80% uncertainty fit is chosen to include the majority of the data while eliminating a few outliers.

(a)

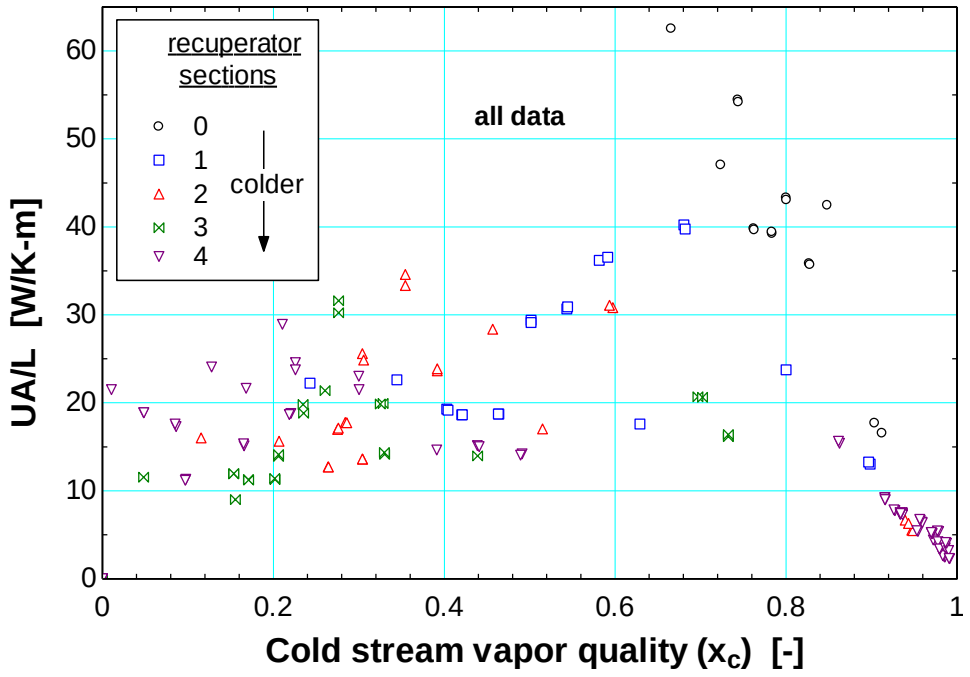

(b)

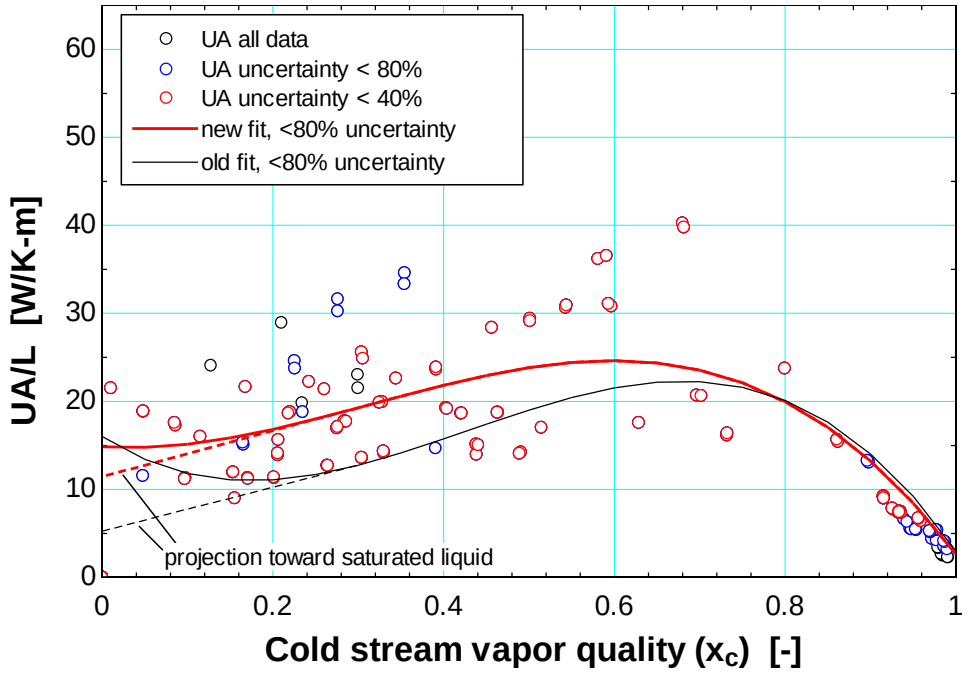

Figure 5-5: Recuperator conductance data normalized by length as a function of cold side quality. (a) shows the full data set sorted by recuperator section, and (b) shows the data sorted by uncertainty, with the new and old 3rd order curve fits and projections toward saturated liquid from a quality of 0.3. (Adapted from Skye 2011)

Table 5-5: 3rd order fit correlation for the recuperator conductance in the 0.3 to 1 cold stream quality region (a) with the pressure drop model implemented and (b) without the pressure drop model (Skye 2011).

Correlation form	Saturated Vapor Constraint
$(UA/L)_{3rd} = a_0 + a_1 x_c^1 + a_2 x_c^2 + a_3 x_c^3$	$(UA/L)_{3rd}\big\|_{x_c=1,new} = 2.649\ [W/K\square m]$ $(UA/L)_{3rd}\big\|_{x_c=1,Skye} = 2.999\ [W/K\square m]$

	Uncertainty Criteria	a_0 [W/K-m]	a_1 [W/K-m]	a_2 [W/K-m]	a_3 [W/K-m]	RMS error (absolute)	R^2	N_{points}
(a) with pressure drop model	UA < 40%	17.04	-35.73	170.01	-148.67	5.16	0.57	90
	UA < 80%	14.84	-6.37	103.15	-108.97	5.26	0.63	122
	none	15.39	-5.24	96.59	-104.10	5.20	0.66	134
(b) without pressure drop model	UA < 40%	17.05	-70.95	244	-187.1	3.449	0.6847	95
	UA < 80%	15.99	-62.49	224.6	-175.1	3.143	0.7481	123
	none	16.86	-58.96	211	-165.9	3.815	0.6847	134

The curve fit follows the trend of the data well for the region from a vapor quality of 0.3-1; however, the 3rd order fit trends upwards in the low quality regions. As shown in previous experiments, the heat transfer coefficients are expected to be exhibit a relatively low and nearly constant value in the liquid regime (Nellis 2005, Hughes 2004); therefore, the correlation is forced to follow the downward trend for vapor values 0-0.3 with a linear projection. The slope for the linear projection is set equal to the slope of the 3rd order fit at a quality of 0.3, and the conductance at the intersection point of the two quality regions is set equal to calculate the second correlation coefficient (see Section 6.2, Skye 2011). Table 5-6 shows the new linear fit correlation coefficients with the pressure

drop model as well as those from Skye 2011. Note that the linear projection forces the constant liquid value to 9.768 [W/K-m], which is significantly higher than shown in Skye 2011. The liquid, two-phase, and vapor correlations are combined into a continuous function, as summarized in Table 5-7. This continuous model is plotted in Figure 5-6.

Table 5-6: Linear fit correlations for the recuperator conductance data in the 0 to 0.3 cold stream quality regions (a) with the pressure drop model implemented and (b) without the pressure drop model (Skye 2011).

Correlation form	b_0 **[W/K-m]**	b_1 **[W/K-m]**
(a) $(UA/L)_{lin} = b_0 + b_1 x_c$ with pressure drop model	11.442	26.1
(b) $(UA/L)_{lin} = b_0 + b_1 x_c$ without pressure	5.238	25.0

Table 5-7: Recuperator conductance correlation over the entire range of cold stream quality (a) with the pressure drop model implemented and (b) without the pressure drop model (Skye 2011).

Quality range	**(UA_{rec}/L_{rec}) Correlation [W/K-m] with pressure drop model**	**(UA_{rec}/L_{rec}) Correlation [W/K-m] without pressure drop model**
$x_c < 0$ (liquid)	11.442	5.238
$0 \le x_c < 0.3$	$11.442 + 26.1\,x_c$	$5.238 + 25.0\,x_c$
$0.3 \le x_c \le 1$	$14.84 - 6.37\,x_c + 103.15\,x_c^2 - 108.97\,x_c^3$	$15.99 - 62.49\,x_c + 224.6\,x_c^2 - 175.1\,x_c^3$
$x_c > 1$ (vapor)	2.649	2.99

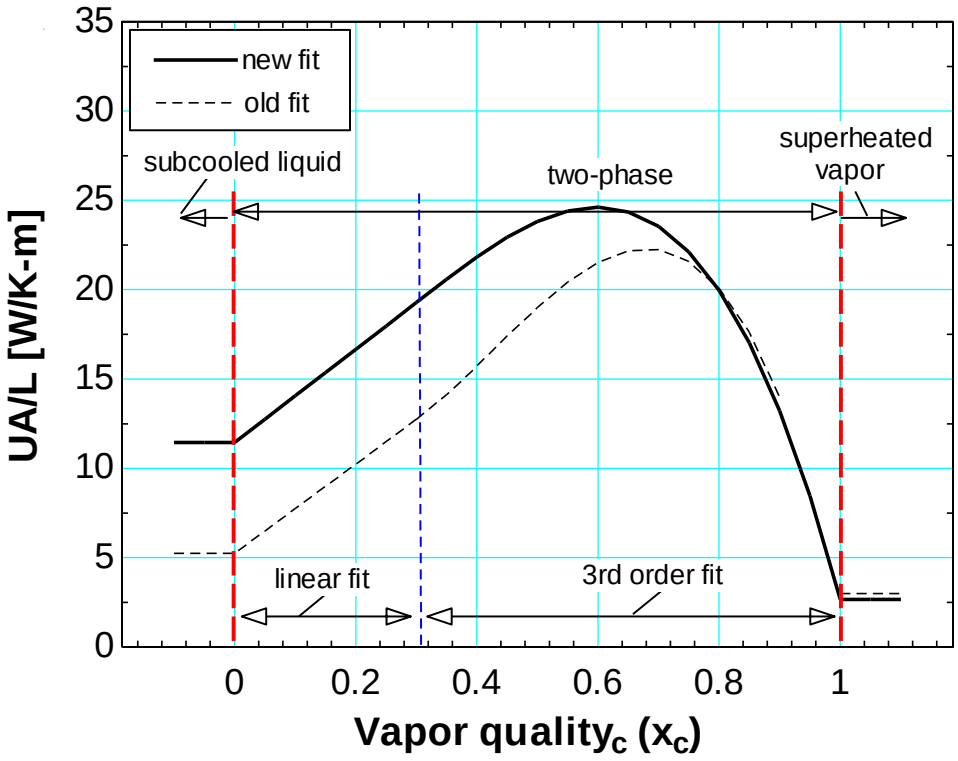

Figure 5-6: Recuperator conductance correlation over the liquid, two-phase, and vapor regimes. The linear and 3rd order fits in the two-phase region for both the new and old model are delineated. (Adapted from Skye 2011)

5.3 Recuperator Model Verification

The recuperator empirical model is verified in the same manner as in Skye 2011 by applying the correlation in Table 5-7 to the experimental data used to create the model. This should give an estimate of its accuracy when used to select mixtures and operating conditions within the range of the experimental data; however, future work should validate the model using a different set of data to test its broad applicability.

A summary of how the simulation model iteratively determines the thermodynamic state points can be found in Section 5.6; for a full description, see Section

6.6.1 of Skye 2011. The measured and predicted recuperator effectiveness is used to evaluate the accuracy of the recuperator model:

$$\varepsilon = \frac{h_4 - h_5}{h_4 - h(P_4, T_7)} \tag{5.2}$$

where h_4 and h_5 are the enthalpies at states 4 and 5, and $h(P_4,T_7)$ represents the minimum possible enthalpy for the hot stream if the pinch point is assumed to occur at the cold end. The predicted effectiveness values were calculated using the temperatures at the hot inlet (T_4) and cold inlet (T_7) inlets. The corresponding pressures were calculated in two different ways: First, all available experimental measurements were used (P_5, P_7, P_1 and the estimate for P_4 calculated using the pressure drop model). Second, just P_4 and P_7 were used and the recuperator pressure drop correlations described in Table 5-1 were used. Figure 5-7 shows the modeled effectiveness as a function of the measured effectiveness calculated both (a) with and (b) without the pressure drop model with the results filtered for <10% uncertainty. The results generally agree for both model versions to within 10-15% (see Figure 5-7(c)). With the <10% uncertainty filter for experimental values of effectiveness removing any significant outliers, the new model gives a slightly lower average percent deviation from the measured effectiveness of about 5.5% compared with 6.5% for the old model. In addition, the measured effectiveness does not exhibit values greater than one using the new model, indicating that there are fewer instances of a pinch point violation in the recuperator.

(a)

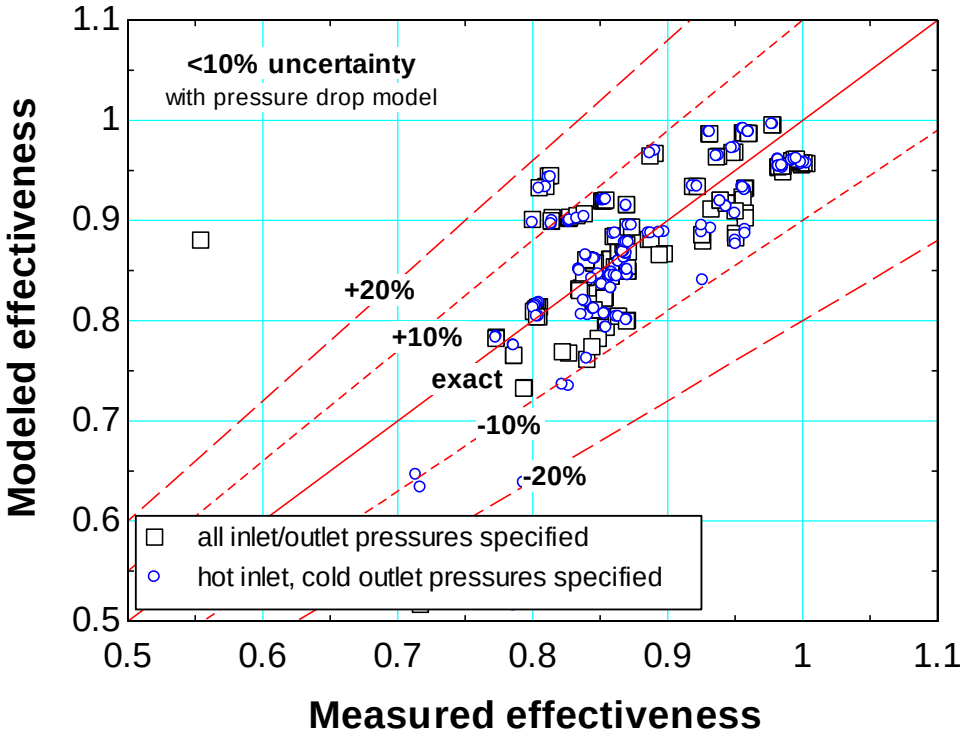
<10% uncertainty
with pressure drop model
+20%
+10%
exact
-10%
-20%
all inlet/outlet pressures specified
hot inlet, cold outlet pressures specified
Modeled effectiveness
Measured effectiveness
0.5
0.6
0.7
0.8
0.9
1
1.1

(b)

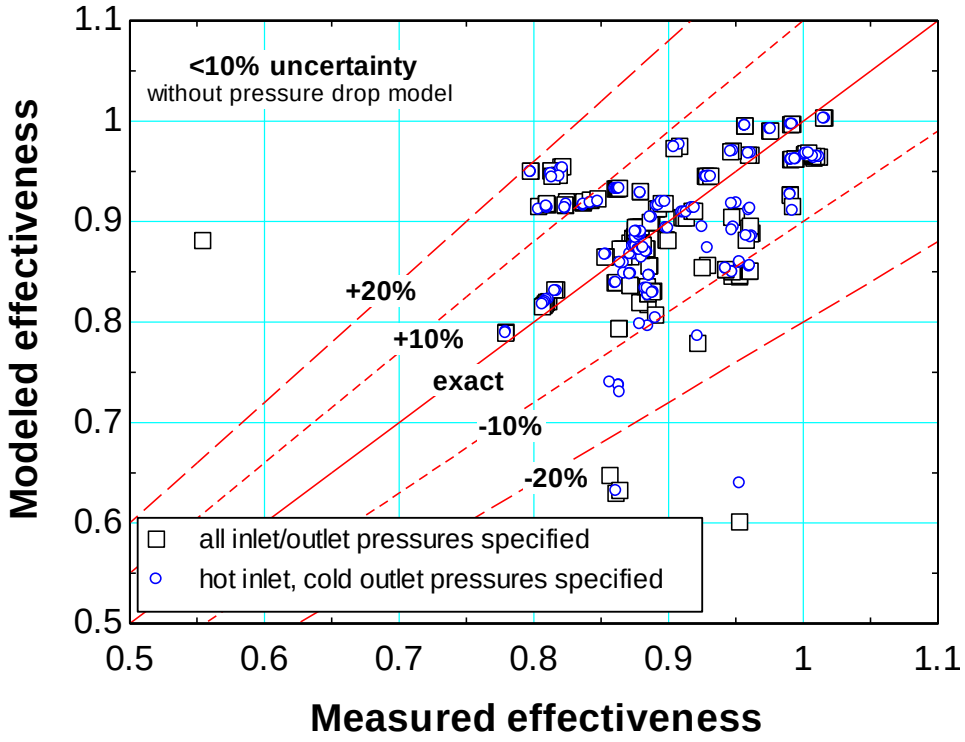
<10% uncertainty
without pressure drop model
+20%
+10%
exact
-10%
-20%
all inlet/outlet pressures specified
hot inlet, cold outlet pressures specified
Modeled effectiveness
Measured effectiveness
0.5
0.6
0.7
0.8
0.9
1
1.1

(c)

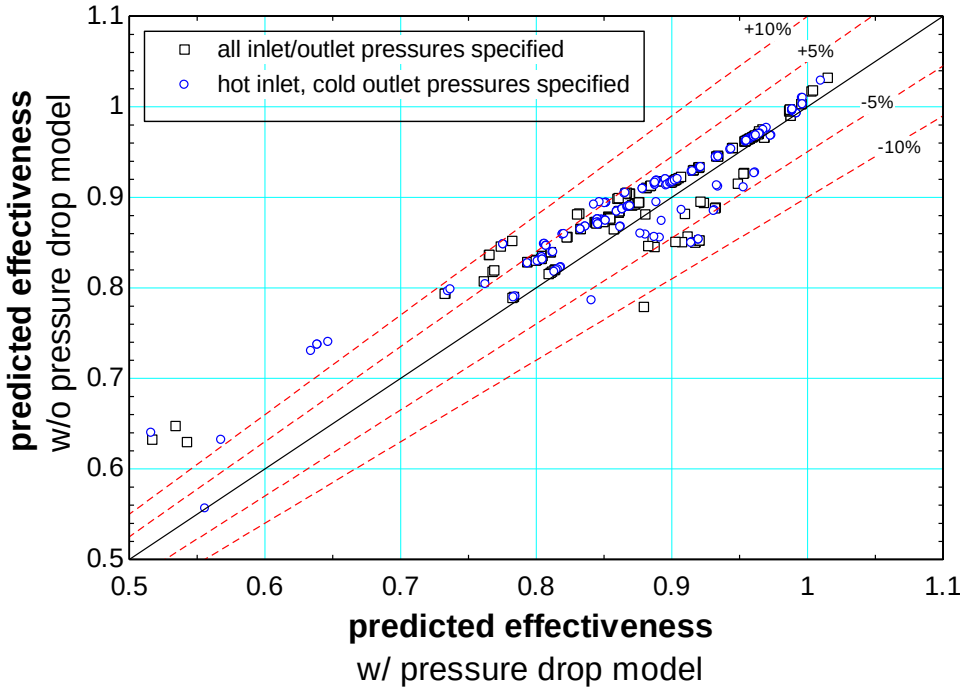

Figure 5-7: Measured vs. predicted recuperator effectiveness with <10% uncertainty both (a) with the pressure drop model and (b) without the pressure drop model implemented. (c) illustrates the difference between (a) and (b). Predictions are made using both the measured pressure values as well as using just the hot inlet and cold outlet pressures with the pressure drop models described. (Adapted from Skye 2011)

5.4 Precooler Conductance

Heat transfer in the precooler is more precisely understood than in the recuperator. The gas mixture can be assumed to exchange heat with the precooling pure refrigerant at constant temperature, and the hot outlet temperature will not vary significantly with mixture composition (sensitive mostly to the 1st stage saturation temperature). For full discussion, see Section 5.2.1 of Skye 2011.

5.4.1 Vapor Phase Conductance

The precooler cold stream (1st stage) flow conditions did not change significantly for the experimental data presented here. Therefore, similar to the recuperator data, the precooler conductance is correlated with the 2nd stage mixture (hot stream) Reynold's number; however, since only the hot stream inlet temperature and pressure are measured, the data is not as resolved as in the recuperator. Figure 5-8(a) shows the precooler vapor conductance normalized by the length of the finned tube in the recuperator (21.7 inches) as a function of the Reynolds number at the hot side inlet sorted by uncertainty. The data with less than 50% uncertainty were chosen to create the curve fit shown in Figure 5-8(b), as they retain the majority of the measurements without significantly increasing the RMS error. Table 5-8 shows the curve fit statistics, including a comparison to the previous correlation without the pressure drop model.

(a)

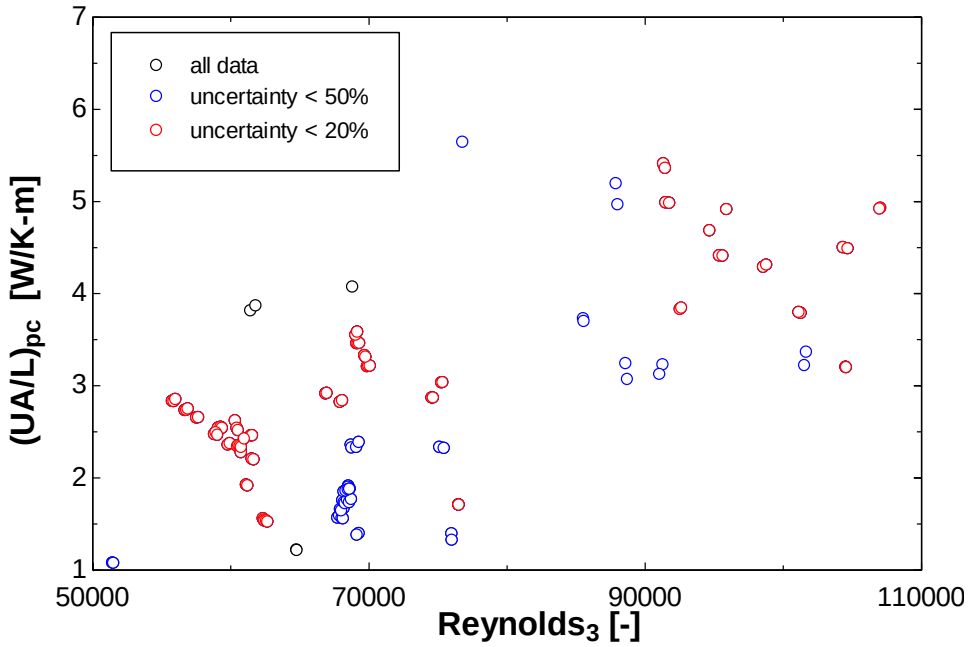

(b)

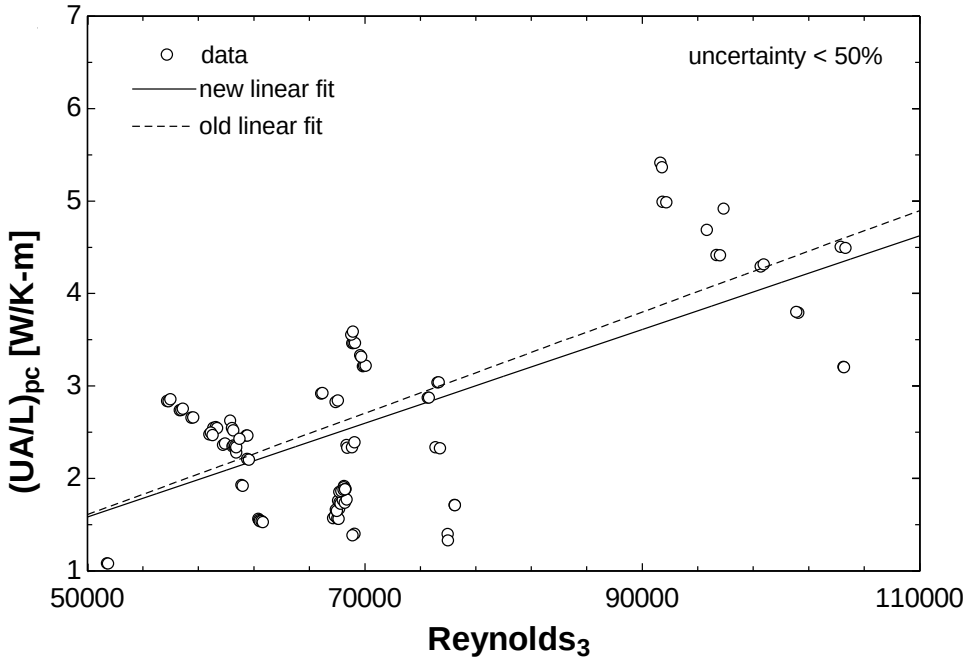

Figure 5-8: Precooler conductance data where the 2nd stage refrigerant exits as a vapor. (a) Conductance normalized by tube length and plotted against hot stream Reynolds number at state 3 sorted by uncertainty. (b) Conductance linear best fit (both new and old) for the <50% uncertainty data. (Adapted from Skye 2011)

Table 5-8: Precooler vapor conductance linear fit and correlation statistics (a) with the pressure drop model and (b) without the pressure drop model (Skye 2011).

$\left.\frac{UA_{pc}}{L_{pc}}\right)_{vap}$ **vs. *Reynolds*$_3$ correlation**						
Correlation form	**Uncertainty Criteria**	**a_0 [W/K-m]**	**a_1 [W/K-m]**	**RMS error [W/K-m]**	**R^2**	**N_{points}**
(a) $\left.\frac{UA_{pc}}{L_{pc}}\right)_{vap} = a_0 + a_1 Re_3$ with pressure drop	*UA/L* < 20% all points	-0.37062	4.71E-05	0.6179	0.58	72
	UA/L < 50% all points	-0.95274	5.07E-05	0.7363	0.45	104
	UA/L < 70% all points	-1.02279	5.14E-05	0.7449	0.44	106
(b) $\left.\frac{UA_{pc}}{L_{pc}}\right)_{vap} = a_0 + a_1 Re_3$ without pressure drop	*UA/L* < 20% all points	-0.53371	5.14E-05	0.7055	0.55	72
	UA/L < 50% all points	-1.13072	5.48E-05	0.8133	0.44	104
	UA/L < 70% all points	-1.21125	5.56E-05	0.8142	0.44	108

5.4.2 Two-Phase Conductance

The vapor conductance model described in the previous section is used with the numerical precooler model (Section 3.4) to determine the length of tube experiencing two-phase flow (see Section 6.4, Skye 2011). The length of finned tube for each section in the vapor state and the one section where the flow transitions to two-phase is calculated:

$$L_{tube,f,pc,i} = \frac{UA_{pc,i}}{\frac{UA_{pc}}{L_{pc}}\left(Re_3\right)} \tag{5.3}$$

where $\frac{UA_{pc}}{L_{pc}}(Re_3)$ is the normalized conductance evaluated with the hot inlet Reynolds number as described in the previous section. The tube length associated with the vapor phase in the transition section is computed based on the fraction of heat transferred in the section to reach the saturation temperature at the section average pressure. This fraction is computed:

$$f_{trans,vap} = \frac{h_{2nd,pc,i-1,trans} - enthalpy\left(\bar{y}_{2nd}, x_{2nd,pc} = 1, P = \left[P_{2nd,pc,i-1} - P_{2nd,pc,i}\right]/2\right)}{h_{2nd,pc,i-1,trans} - h_{2nd,pc,i,trans}} \quad (5.4)$$

where $h_{2nd,pc,i-1,trans}$, $h_{2nd,pc,i,trans}$, $P_{2nd,pc,i-1}$ and $P_{2nd,pc,i}$ are the enthalpies and pressures of the 2nd stage refrigerant at the beginning and end of the transition section. The length of precooler tube experiencing two-phase flow can then be calculated by subtracting the summed vapor length from the total precooler finned tube length ($L_{pc,f}$):

$$L_{tube,f,pc,2\phi} = L_{pc,f} - \left(\sum_{i=1}^{\#sections_{vapor}} \frac{UA_{pc,i}}{\frac{UA_{pc}}{L_{pc}}(Re_3)} + f_{trans,vap} \left. \frac{UA_{pc,i}}{\frac{UA_{pc}}{L_{pc}}(Re_3)} \right|_{trans} \right) \quad (5.5)$$

where $x_{2nd,pc}$ is the thermodynamic quality of the 2nd stage refrigerant in the precooler and $\left. \frac{UA_{pc,i}}{\frac{UA_{pc}}{L_{pc}}(Re_3)} \right|_{trans}$ is the computed tube length in the transition section. The same method is used to compute the two-phase conductance:

$$UA_{pc,2\phi} = UA_{pc} - \left(\sum_{i=1}^{\#sections_{vapor}} UA_{pc,i} + f_{trans,vap} UA_{pc,i}\Big|_{trans} \right) \tag{5.6}$$

where $UA_{pc,i}\Big|_{trans}$ is the conductance in the transition section and UA_{pc} is the total precooler conductance, computed as:

$$UA_{pc} = \sum_{i=1}^{N_{pc}} UA_{pc,i} \tag{5.7}$$

The length-normalized conductance can be computed by dividing the results from Eq. (5.5) and Eq (5.6):

$$\left(\frac{UA_{pc}}{L_{pc}} \right)_{2\phi} = \frac{UA_{pc,2\phi}}{L_{tube,f,pc,2\phi}} \tag{5.8}$$

The quality chosen to correlate the conductance normalized by length is the average between the transition section (saturated vapor, $x_{2nd,pc} = 1$) and the precooler hot exit. Unlike the recuperator, there is insufficient two-phase data to create a precise curve fit correlating the precooler conductance with the fluid quality (see Figure 5-9); instead, the fit is based on observations from the recuperator experimental data. A second order polynomial (see Table 5-9) is used to estimate the quality peak observed in the recuperator data, with the saturated vapor value set to 3 W/K-m (from the averaged vapor values shown in Figure 5-8) and the saturated liquid value set 4.5 times higher at 13.5 W/K-m.

Table 5-9: Quadratic fit correlation for the precooler two-phase conductance data both (a) with the pressure drop model and (b) without the pressure drop model.

Correlation form	b_0 [W/K-m]	b_1 [W/K-m]	b_2 [W/K-m]
(a) with pressure drop model $\left(UA_{pc}/L_{pc}\right)_{2\phi} = b_0 + b_1 x_{2nd,pc} + b_2 x_{2nd,pc}^2$	13.5	239.2	-249.7
(b) without pressure drop model $\left(UA_{pc}/L_{pc}\right)_{2\phi} = b_0 + b_1 x_{2nd,pc} + b_2 x_{2nd,pc}^2$	5	290.1	-291.6

The precooler conductance correlation is created to enforce a continuous function between flow regimes (see Skye 2011 Section 6.1 for full discussion):

$$UA_{pc}/L_{pc} = Eterm \underbrace{\left(a_0 + a_1 Re_3\right)}_{vapor\ correlation} + \left(1 - Eterm\right)\underbrace{\left(b_0 + b_1 x_{2nd,pc} + b_2 x_{2nd,pc}^2\right)}_{two-phase\ correlation} \tag{5.9}$$

where:

$$Eterm = \exp\left(-100\left(1.001 - x_{2nd,pc}\right)\right) \tag{5.10}$$

where a_0 and a_1 are the vapor conductance curve fit terms from Table 5-8, Re_3 is the Reynolds number at the 2nd stage high pressure inlet of the precooler (state 3), b_0, b_1, and b_2 are the curve fit terms for the two-phase precooler conductance correlation, and $x_{2nd,pc}$ is the quality of the 2nd stage fluid in the precooler. The final curve fit is plotted with a comparison to the previous curve fit in Figure 5-9, and the precooler conductance model across the three flow regimes is summarized in Table 5-10.

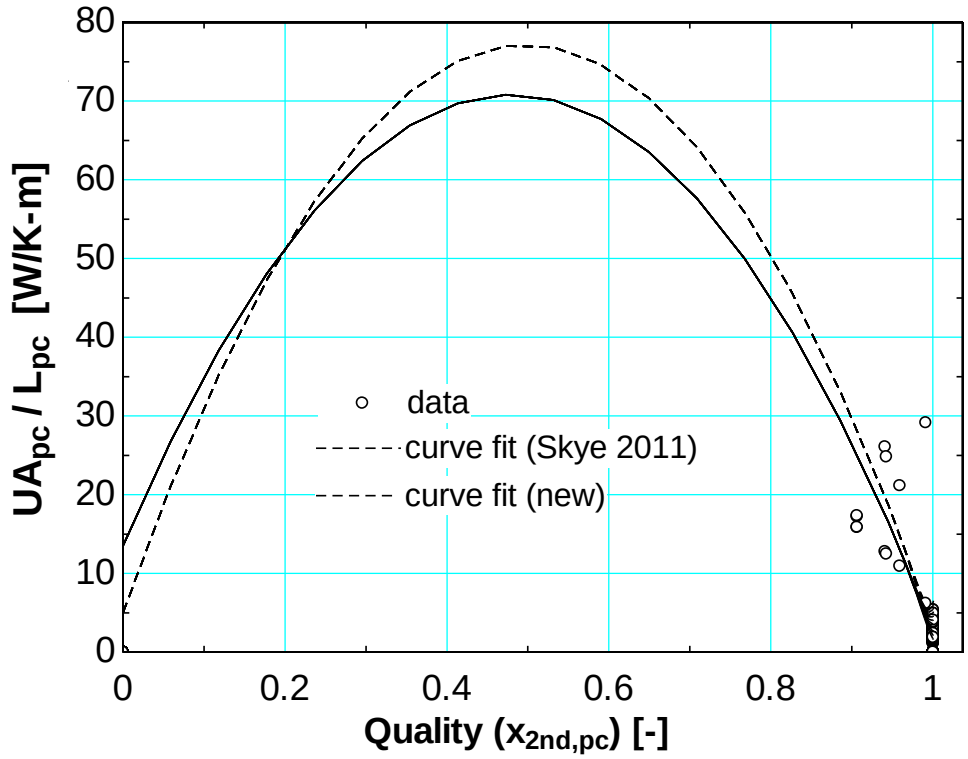

Figure 5-9: Length-normalized two-phase precooler conductance data as a function of the local thermodynamic quality. The data points and both the new and previous curve fits are shown. Vapor values are included with a quality of 1.001 for comparison. (Adapted from Skye 2011)

Table 5-10: Final precooler conductance correlation extending through the liquid, two-phase, and vapor regimes.

Correlation form
$UA_{pc} / L_{pc} = Eterm\left(a_0 + a_1 Re_3\right) + \left(1 - Eterm\right)\left(b_0 + b_1\, x_{2nd,pc} + b_2 x_{2nd,pc}^2\right)$
$Eterm = \exp\left(-100\left(1.001 - x_{2nd,pc}\right)\right)$

Coefficients					
Correlation version	a_0 **[W/K-m]**	a_1 **[W/K-m]**	b_0 **[W/K-m]**	b_1 **[W/K-m]**	b_2 **[W/K-m]**
(a) with pressure drop model	-0.953	5.07E-05	13.5	239.2	-249.7
(b) without pressure drop model	-1.13	5.48E-05	5	290.1	-291.6

5.5 Precooler Model Verification

The precooler conductance model in Section 5.4 was validated using a similar method as described for the recuperator in Section 5.3. A summary of how the simulation model iteratively determines the thermodynamic state points can be found in Section 5.6; for a full description, see Section 6.6.1 of Skye 2011. Since there are insufficient temperature and pressure measurements for the 1st stage fluid, the precooler effectiveness is defined using the enthalpy change in the 2nd stage mixture:

$$\varepsilon_{pc} = \frac{h_3 - h_4}{h_3 - h(P_3, T_8)} \tag{5.11}$$

where h_3 and h_4 are the 2nd stage inlet and outlet enthalpies, respectively, and $h(P_3,T_8)$ represents the minimum possible hot stream exit enthalpy where mixture exits at the evaporation temperature of the 1st stage refrigerant (T_8). Similar to the recuperator validation, two different estimates of the pressure at state 4 were used to explore the sensitivity of the effectiveness calculation to the pressure drop correlation. The first method estimates the precooler hot side outlet pressure using the pressure drop model described in Chapter 4 for the new model (and the average of P_3 and P_5 for the old model). The second method uses the value determined using the appropriate pressure drop correlation described in Section 5.1.

Figure 5-10 shows the precooler measured vs. modeled effectiveness both with and without the pressure drop model implemented, filtered for <50% uncertainty in the precooler *UA*. For both model versions, most of the data lie within 20% agreement. The new model shows slightly more scatter, with an average deviation of about 12% in

comparison to 10% for the model from Skye 2011. However, the worse agreement is caused by the new model including more data points in the analysis (i.e. more points converged to a reasonable, non-negative UA value). Additionally, we again see that there are fewer instances of a pinch point violation calculated in the precooler, as evident by a lack of effectiveness values greater than one.

(a)

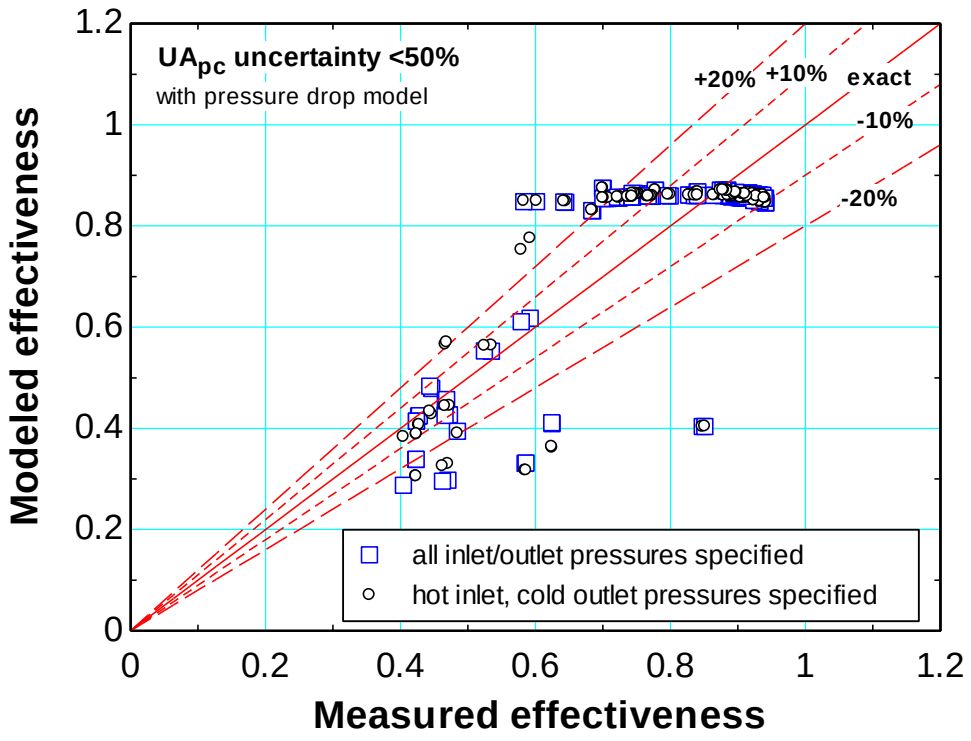

(b)

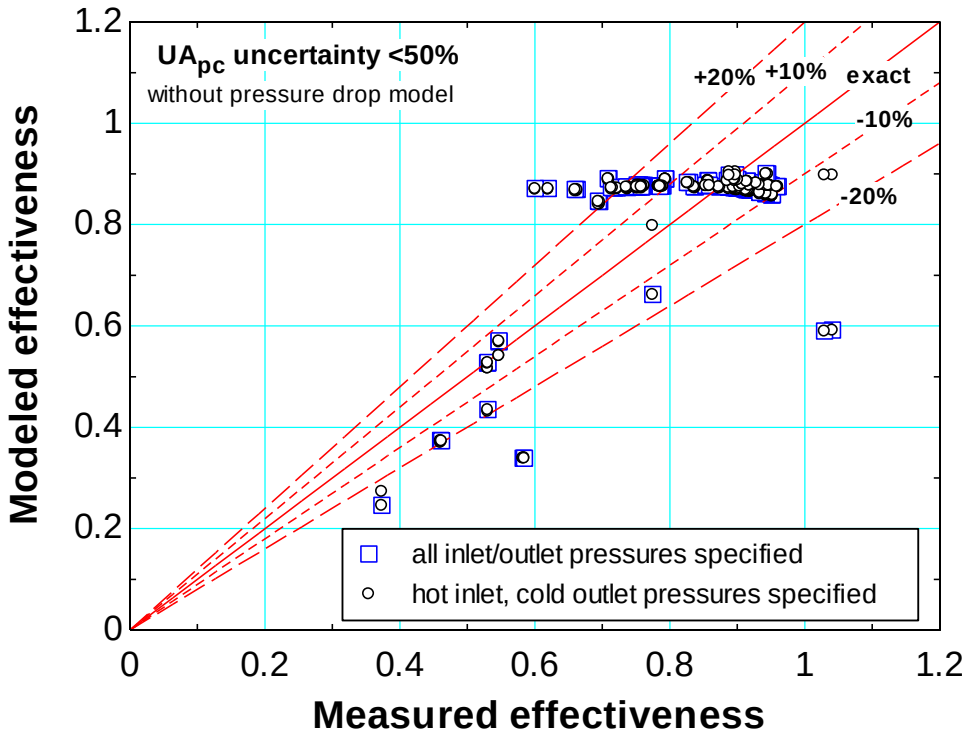

Figure 5-10: Measured vs. predicted precooler effectiveness with <50% UA uncertainty both (a) with the pressure drop model and (b) without the pressure drop model implemented. Predictions are made using both the measured pressure values as well as using just the hot inlet and cold outlet pressures with the pressure drop models described. (Adapted from Skye 2011)

5.6 System Model Verification

The pressure drop and conductance correlations are implemented into the simulation model to predict the refrigeration power of the system at a specified load temperature (T_7). The accuracy of the model is evaluated by comparing the predicted refrigeration power with the measured refrigeration power (uncertainty ±0.00001 W) from the experimental data. For direct comparison with the first generation empirical model developed by Skye, a fixed 2nd stage mass flow is given as an input to the simulation model in addition to the suction and discharge pressures rather than using the

compressor performance map as described in Chapter 6. Additionally, for the majority of the experimental data points, the compressor bypass valve was used to manually adjust the pressure ratio across the compressor, thus confounding the relationship between the mass flow and pressures for the compressor. The simulation model has a limited number of inputs to simulate a real-world design situation where few measurements are available. These inputs include:

1. 2nd stage circulating mixture composition
2. 2nd stage mass flow
3. 2nd stage compressor suction and discharge pressures (P_1 and P_3),
4. 2nd stage load temperature (T_7),
5. 2nd stage high pressure inlet temperature (T_3, which is nominally ambient temperature)
6. 1st stage evaporator (precooler) saturation temperature ($T_8 = T_{11}$)

A detailed description of the simulation model can be found in Section 6.6.1 of Skye 2011. Using the inputs described above, the model uses a method similar to the data processing method described in Chapter 0 to calculate the thermodynamic state points, the heat exchanger conductances, and the refrigeration load. The heat exchanger models divide the energy exchange into small sections (60 in the recuperator and 15 in the precooler) that have relatively constant specific heats, allowing the effectiveness-NTU relationship to be applied. An iterative method is used to predict the conductance by varying the outlet temperature until the computed and actual lengths of finned tube agree. The computed length of finned tube in each iteration is found by dividing the conductance of each section (calculated as in Chapter 0) by the empirical length-normalized conductance correlation (as described in Sections 5.2 and 5.4) at the predicted

flow conditions. Figure 5-11(a) compares the refrigeration power measured during the experimental tests with the values calculated using the new simulation model. Similar to the results from Skye 2011, the prediction for low refrigeration power (tests using pure refrigerants and the three-component mixture) is within 20% of the measured value. Unfortunately, as the heat input increases, the agreement is worse; however, as shown in Figure 5-11(b), there are a few promising differences between the new and old models in this region.

Test points 142 and 143 show the greatest improvement with the pressure drop model implemented, with the predicted refrigeration increased by a factor of about 4. This drastic improvement is caused by a lower predicted pressure drop in the precooler, which results in a larger predicted enthalpy change in the hot stream and a larger heat transfer rate. As shown in Figure 5-12, this results in the precooler fluid exiting in a two-phase state and drastically increases the precooler conductance prediction (see Section 5.4). Additionally, the new model predicts a larger conductance at low quality in the recuperator (see Section 5.2), resulting in a lower temperature leaving the hot side of the recuperator. The results for test point 144 are similar; the old empirical model actually does not converge due to a pinch point violation. However, the new model, again predicting a smaller pressure drop in the precooler, pushes the exit conditions into the two phase region and gives a prediction within 25% of the measured value. Test points 146 and 147 also show a marked increase in predicted refrigeration power from about 15 to 20 W. These test points are from the relatively small number of tests that have a very low quality in the recuperator (around 0.06 at the exit); as seen in Section 5.2, the new

model including the pressure drop model shows a much higher conductance prediction in this region.

These results suggest that the pressure drop model improvements may help to more accurately predict the refrigeration power of the system for better-performing mixtures. The agreement for the majority of the data that have a heat input of less than 15 W is within 20%; more data points with larger heat inputs would be necessary to explore the performance in more detail at these conditions. Additionally, the uncertainty of the mass flow measurements as discussed in Section 2.2.2 may have some effect on these results. The precooler performance is another large factor in the predictions for the mixtures with a higher refrigeration power. As many of these points are near the dew point at the precooler exit, more data points that exhibit two-phase flow in the precooler are important to accurately predict the system performance.

(a)

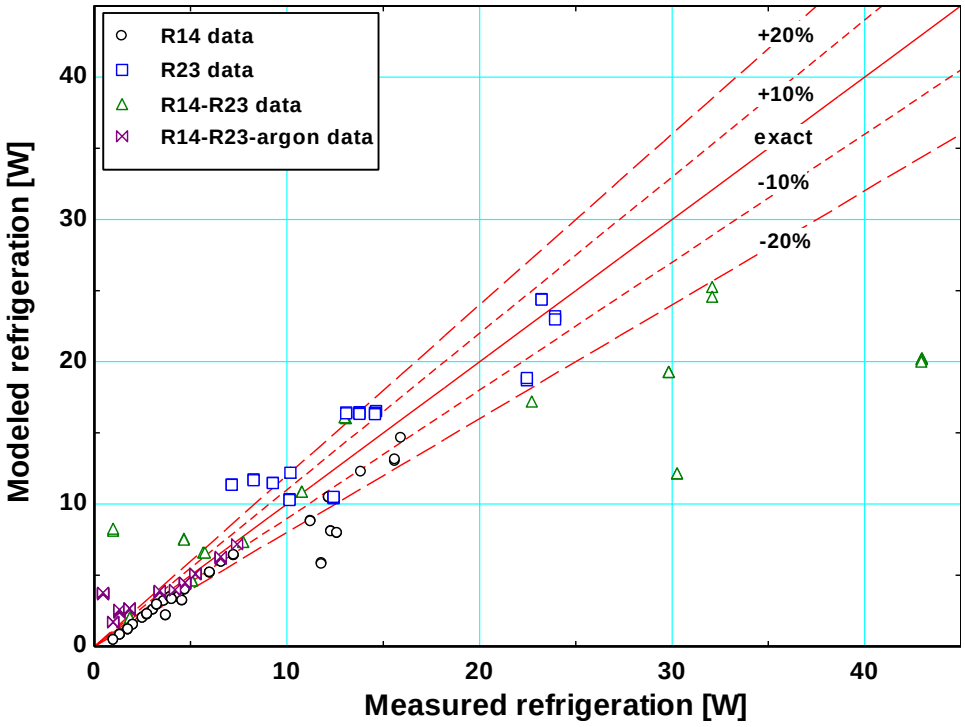

(b)

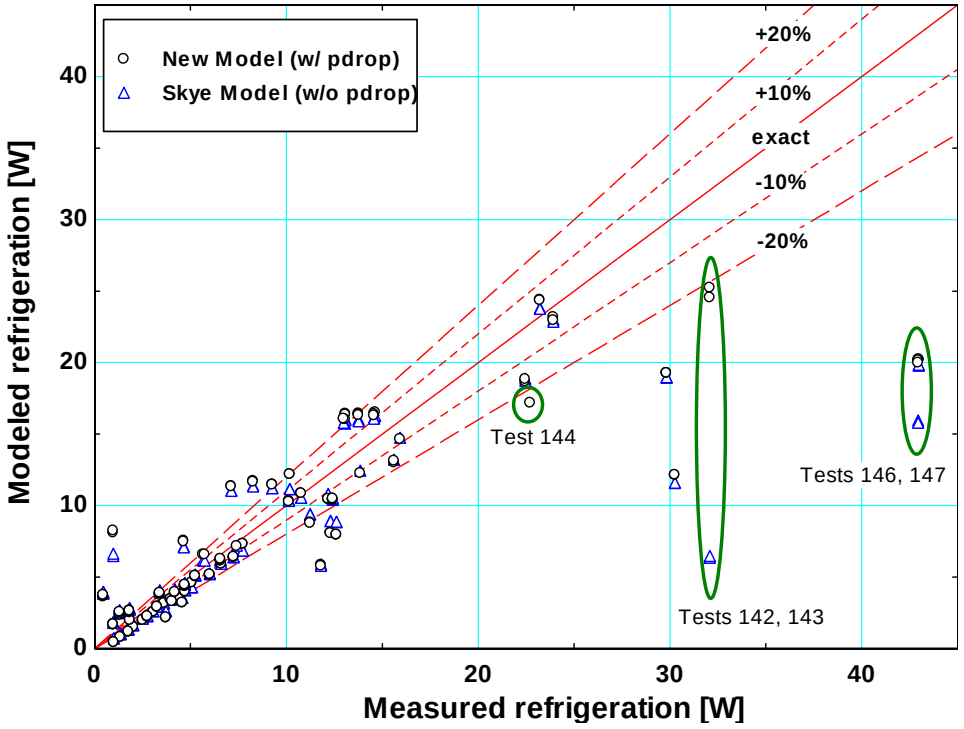

Figure 5-11: Measured refrigeration power compared to refrigeration predicted using the empirically tuned model (a) sorted by working fluid and (b) comparing the results with and without the pressure drop implemented with important test points highlighted. (Adapted from Skye 2011)

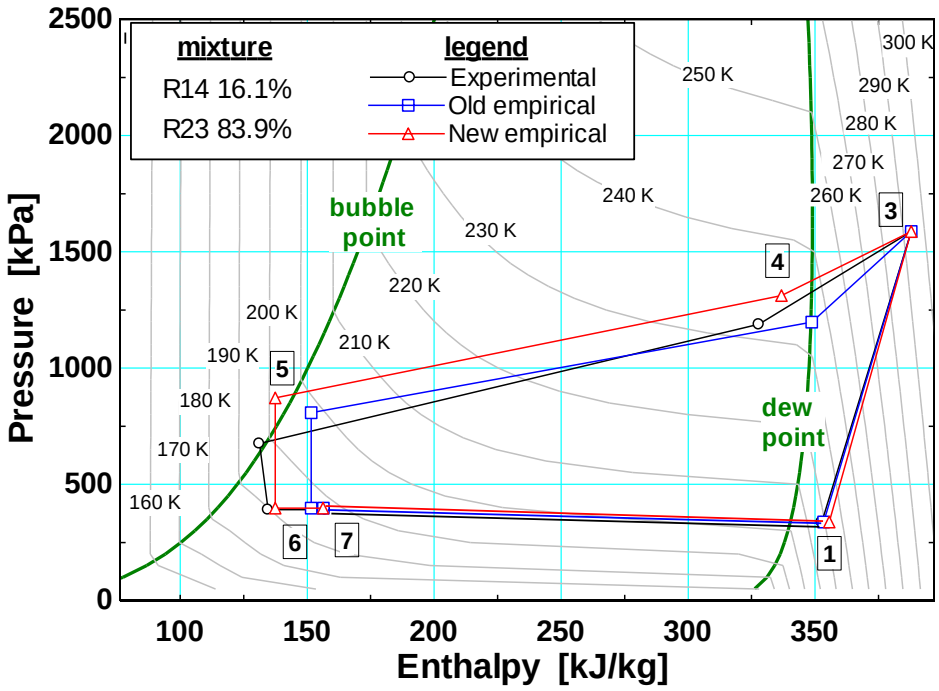

Figure 5-12: Pressure-enthalpy diagram for the 2nd stage cycle comparing the experimental data (with P_4 estimated using the pressure drop model) to both the old and new empirical model results. (Adapted from Skye 2011)

5.7 References

Hughes, C. B. 2004. Experimental Measurement of Heat Transfer Coefficients for Mixed Gas Working Fluids in Joule-Thomson Systems. M.S. thesis. Madison, WI USA: University of Wisconsin - Madison, Mechanical Engineering Dept.

Nellis, G., C. Hughes and J. Pfotenhauer. "Heat transfer coefficient measurements for mixed gas working fluids at cryogenic temperatures". *Cryogenics* 2005; 45(8): 546-556.

Skye, H.M. 2011. Modeling, Experimentation and Optimization for a Mixed-Gas Joule-Thomson Cycle with Precooling for Cryosurgery. PhD thesis. Madison, WI USA: University of Wisconsin – Madison, Mechanical Engineering Department.

Timmerhaus, K. D. and T. M. Flynn. *Cryogenic Process Engineering* 1989.

6 Compressor Map

6.1 Volumetric Efficiency Model

The volumetric efficiency model is used to map the performance of the 2nd stage compressor (Danfoss model TFS4.5CLX) in order to link the mass flow rate of the gas mix cycle to the pressure ratio across the compressor. Volumetric efficiency is defined as the ratio of the volume of fluid actually displaced by the piston to its swept volume. The semi-empirical model used was developed by Popovic and Shappiro (1995):

$$\eta_{vol} = \frac{\dot{V}_{suction}}{\dot{V}_{disp}} = 1 + C - C\left(\frac{P_{discharge}}{P_{suction}}\right)^{\frac{1}{n}} \tag{6.1}$$

where
- η_{vol} - volumetric efficiency
- $\dot{V}_{suction}$ - suction volumetric flow rate
- $\dot{V}_{disp}$ - displacement rate
- C - clearance volume ratio
- $P_{discharge}$ - discharge pressure
- $P_{suction}$ - suction pressure
- n - polytropic exponent

For the full derivation of this model, reference Jähnig Chapter 3.3 (1999). This model neglects that the state of the re-expanded clearance vapor will be slightly different than the state of the fluid in the suction line, instead assuming that the specific volume after taking in fresh refrigerant is equal to the specific volume of the refrigerant in the suction line. Pressure drop through the valves is also neglected.

6.2 Performance Experiments

Many of the variables in Eq. (6.1) can be measured experimentally. Table 6-1 gives a summary of measurements and sensor names, and Figure 6-1 shows a diagram of the measurement locations for the performance tests. The suction volumetric flow rate is calculated using the 2nd stage mass flow and the inlet conditions:

$$\dot{V}_{suction} = \dot{m}_{2nd} / \rho(T_{suction}, P_{suction}) \tag{6.2}$$

where $P_{suction}$ is the pressure measured by the AMS sensor in Figure 3-2 (P_5) and $T_{suction}$ is measured by TC_3. The AMS pressure sensor is built into the compressor unit and is therefore well-located for an accurate measurement of the inlet pressure.

Table 6-1: List of compressor map variable names and corresponding experimental measurement sensors.

Variable name	Sensor name (Figure 3-2)	Sensor location	Measurement error	Max error (est. with error due to location)
$P_{suction}$	P5 (AMS sensor)	compressor inlet	+/-1%	+/-1%
$T_{suction}$	PRT[14]	inside dewar (cold side recuperator outlet)	+/-0.5 K	+/-5 K
$\dot{m}_{2nd}$	$\dot{m}_{2nd}$	after flex hose (high pressure side)	+/-1%	+/-1%
$P_{discharge}$	P1	after flex hose (high pressure side)	+/-3 psi	+20%

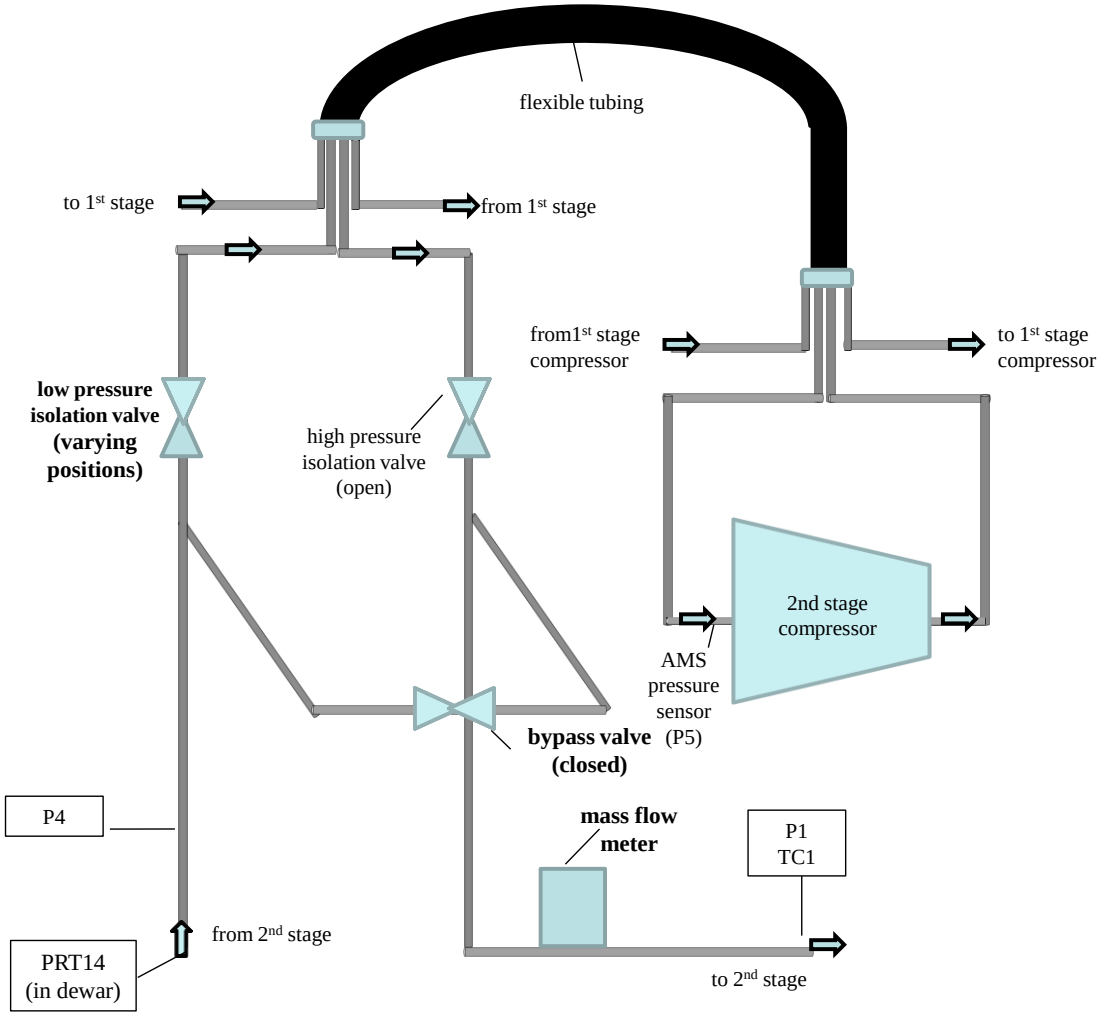

Figure 6-1: Partial cycle diagram (not shown to scale) for performance tests with bypass closed and low pressure isolation valve used to regulate the system pressure ratio.

The second stage fluid, exiting the cold side of the recuperator at greater than 280 K (measured by PRT_{14}), is well-estimated as being room temperature (measured by TC_3) by the time it reaches the compressor inlet. This effect is due to the vapor phase fluid traveling through the long length of tubing connecting the test section to the compressor,

which effectively serves as an aftercooler. To verify this assumption, an effectiveness-NTU analysis was performed on the heat exchanger return tube using several experimental measurements from the performance tests described in the next section (see Table 6-2). For the most extreme temperature difference observed, with a dewar outlet temperature of 279 K and an ambient temperature of 301 K, the calculated fluid outlet temperature was calculated to be within 5 K of ambient.

Table 6-2: Results of effectiveness-NTU analysis used to verify that the ambient temperature is a good estimate of the compressor inlet temperature.

T_{amb} (TC_3) [K]	$T_{suction}$ (PRT_{14}) [K]	Effectiveness [-]	$T_{out,calc}$ ($T_{comp,in,est.}$) [K]	ΔT (T_{amb} -$T_{comp,in,est.}$) [K]
297.9	292	0.8945	297.3	0.6225
298	292.5	0.9335	297.6	0.3659
297.2	293	0.9656	297.1	0.1443
297.9	293.3	0.989	297.8	0.05042
299.7	291.8	0.9451	299.3	0.4336
301.1	281.9	0.8826	298.8	2.255
301.3	280.9	0.8733	298.7	2.584
300.8	279.1	0.8386	297.3	3.503
300.2	286.5	0.8841	298.6	1.588
301.2	289.9	0.9054	300.1	1.068
301.1	292.4	0.9465	300.6	0.4651

The displacement rate can be calculated from data provided by the manufacturer:

$$\dot{V}_{disp} = V_{disp}\ RPM \tag{6.3}$$

However, as Section 6.3.1 discusses, the values from the manufacturer may not be accurate. Another variable from Eq. (6.1), the discharge pressure, is measured using P_1 from Figure 3-2, which introduces uncertainty due to the pressure drop through the

flexible tubing between the compressor and the measurement point. If this pressure drop is estimated using the Müller-Steinhagen correlation presented in Chapter 4, it shows an underestimation of the compressor outlet pressure of up to 20% (i.e. the pressure drop is up to 20% of the measured absolute suction pressure, see Figure 6-2). The polytropic exponent *n* from Eq. (6.1) is replaced by the isentropic exponent *k*, which changes with changing mixture composition:

$$k = \frac{c_p(T_{suction}, P_{suction})}{c_v(T_{suction}, P_{suction})} \tag{6.4}$$

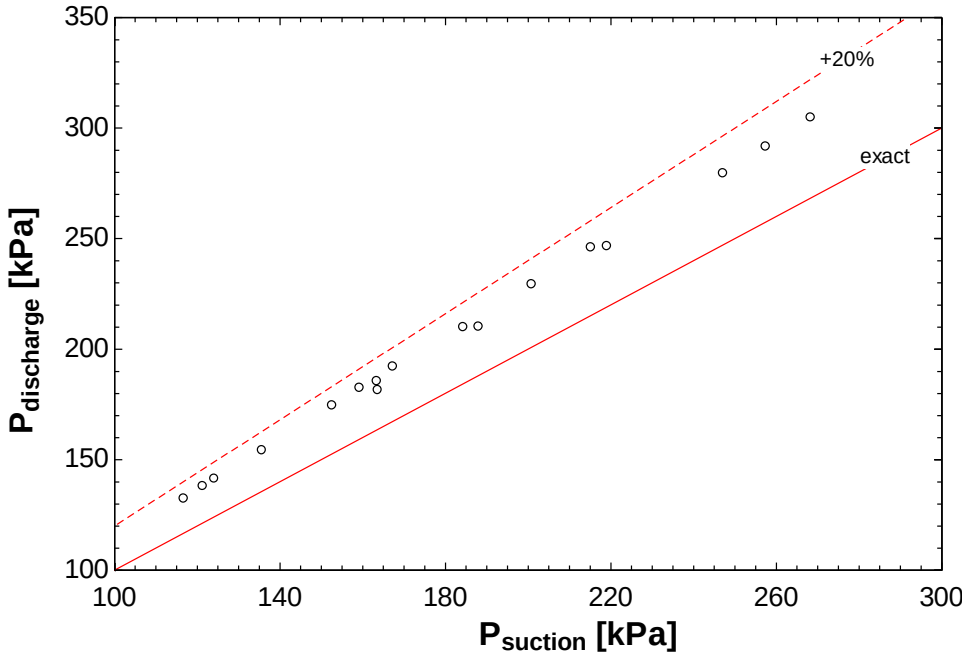

Figure 6-2: Predicted compressor outlet pressure using the Müller-Steinhagen correlation as a function of the measured compressor inlet pressure.

In the simulation model, the compressor model will predict a mass flow from the design suction and discharge pressures. All of the experimental data processed as

discussed in Chapter 0 were taken with the compressor bypass valve partially open in order to regulate the pressure ratio in the system (see Figure 3-2 for location in the experiment). As a result, the actual mass flow through the compressor was not measured for these tests because an unmeasured fraction of the flow was diverted through the compressor bypass. In order to formulate a compressor map relating the pressure ratio and the mass flow, additional experimental tests with the bypass valve closed were taken using nitrogen and R23 as working fluids. These fluids were chosen because they have very different physical properties. Rather than using the bypass valve to regulate the pressure ratio across the compressor, the low pressure isolation valve was used. The low pressure isolation valve is located on the experiment side of the flexible tubing between P_4 and P_5 (see Figure 6-1).

Tests spanning the possible charge pressures were taken (see Table 6-3), with additional tests taken at each charge pressure with varying positions of the low pressure valve. Figure 6-3 shows the resulting data with the second stage mass flow as a function of the pressure ratio:

$$P_{ratio} = \frac{P_{discharge}}{P_{suction}} \tag{6.5}$$

Higher mass flows loosely correlate with a higher charge pressure, but the position of the isolation valve also regulates the flow rate (see Figure 6-4). For example, the highest R23 mass flow of 0.83 g/s corresponds to the highest charge pressure of about 120 psig, and the lowest nitrogen mass flow of 0.19 g/s corresponds to the lowest charge pressure of about 40 psig; however, the positioning of the isolation valve causes intermediate mass flows from tests with a range of charge pressures.

Table 6-3: Summary of test parameters for the collected compressor data.

2nd stage	**Set 1**	**Set 2**
Working Fluid	Nitrogen	R23
High Pressure	110-260 psig	170-255 psig
Low Pressure	3-25 psig	5-15 psig
Static Charge Pressure	40-100 psig	80-120 psig
Mass flow ($\dot{m}_{2nd}$)	0.18 -0.47 g/s	0.48-0.83 g/s

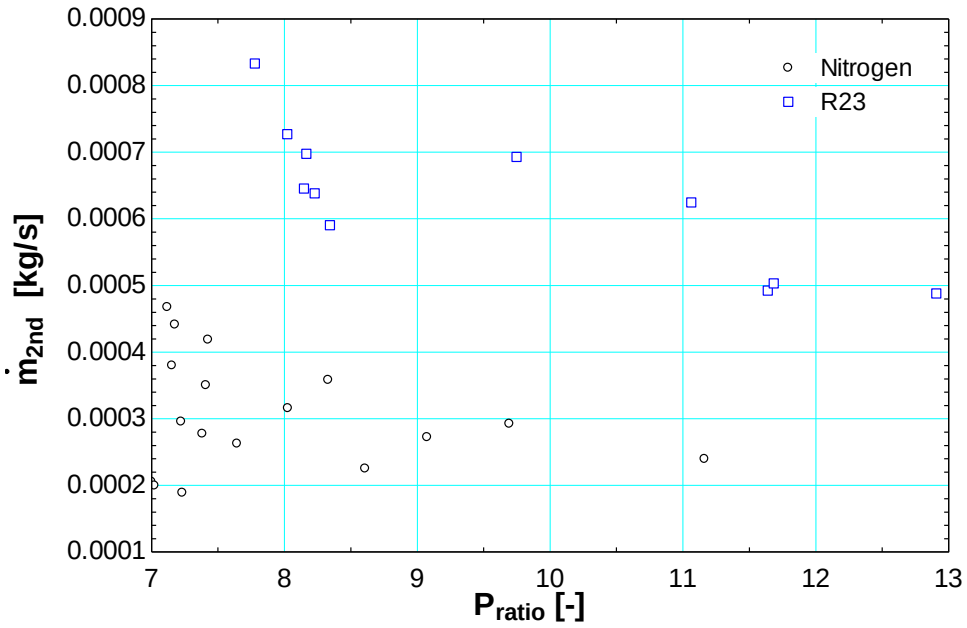

Figure 6-3: Experimental data with bypass closed with both nitrogen and R23 as the working fluids, showing the second stage mass flow as a function of the pressure ratio.

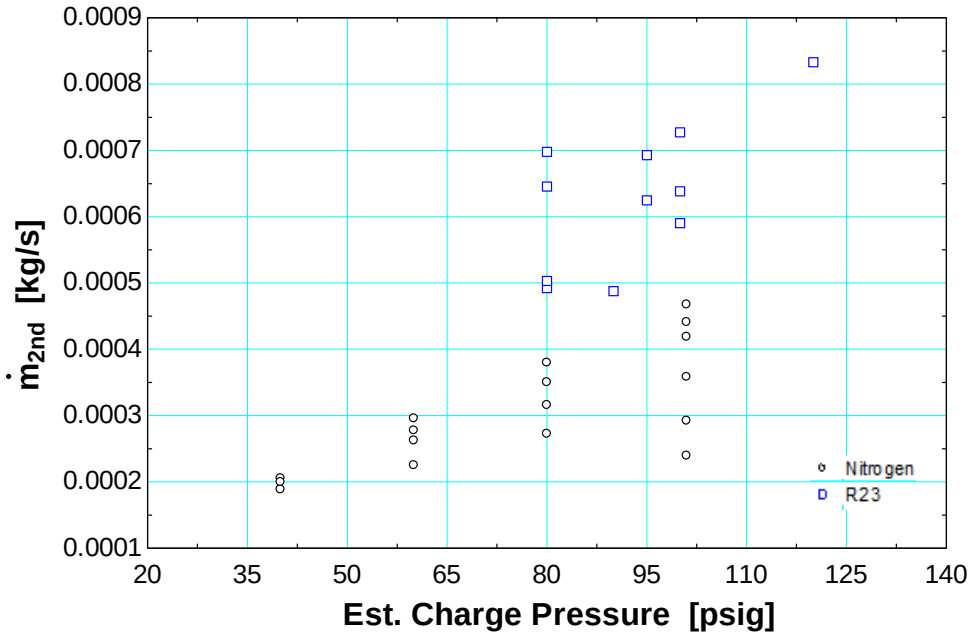

Figure 6-4: Mass flow as a function of the estimated charge pressure.

6.3 Simulation Model (Calculating the Volumetric Efficiency)

Two constant parameters have to be estimated to calculate the volumetric efficiency in Eq. (6-1): the clearance volume ratio *C* and the displacement rate $\dot{V}_{disp}$. The polytropic index was set to the specific heat ratio evaluated at the compressor inlet conditions, with values for nitrogen about 1.4 and the values for R23 about 1.2.

6.3.1 Using Manufacturer's Data

The experimental measurements from the tests described in the previous section are used with Eq. (6.1) to calculate the clearance volume ratio. If the data reported by Danfoss are used to estimate the displacement rate using Eq. (6-3), with V_{disp} = 4.63 cm^3 and RPM = 60 Hz, *C* is the only variable not measured in this equation and the clearance volume ratio can be calculated for each experimental point and averaged to find the best

overall estimate. The estimates of the clearance volume ratio and the displacement rate calculated using this method is shown in Table 6-4 with the RMS errors. Figure 6-5 shows the volumetric efficiency of the experimental data as a function of the pressure ratio, with curve fits formulated using the manufacturer's data and the value of *C* shown in Table 6-4. The results show a poor fit, with the R23 RMS error being a large fraction of the experimental volumetric efficiency (over 30%). The nitrogen error is smaller, but Figure 6-5 visually shows that the fit does not follow the trend of the data well. If the clearance volume ratio is plotted as a function of the pressure ratio (see Figure 6-6), there is a strong trend observed. Additionally, the volumetric efficiency from both the experimental data and the fit is much lower than expected for a compressor operating near its design condition. This may indicate that the manufacturer's data does not accurately describe this compressor's displacement rate.

Table 6-4: Compressor correlation form with the manufacturer's data used to estimate the displacement rate.

Correlation form (using manufacturer's data)	***C*** **[-]**	$\dot{V}_{disp}$ **[m^3/s]**	E_{RMS} **Nitrogen**	E_{RMS} **R23**	E_{RMS} **all data**
$\eta_{vol} = \frac{\dot{V}_{suction}}{\dot{V}_{disp}} = 1 + C - C\left(\frac{P_{comp,out}}{P_{comp,in}}\right)^{\frac{1}{n}}$	0.11860	0.0002701	0.066	0.189	0.129

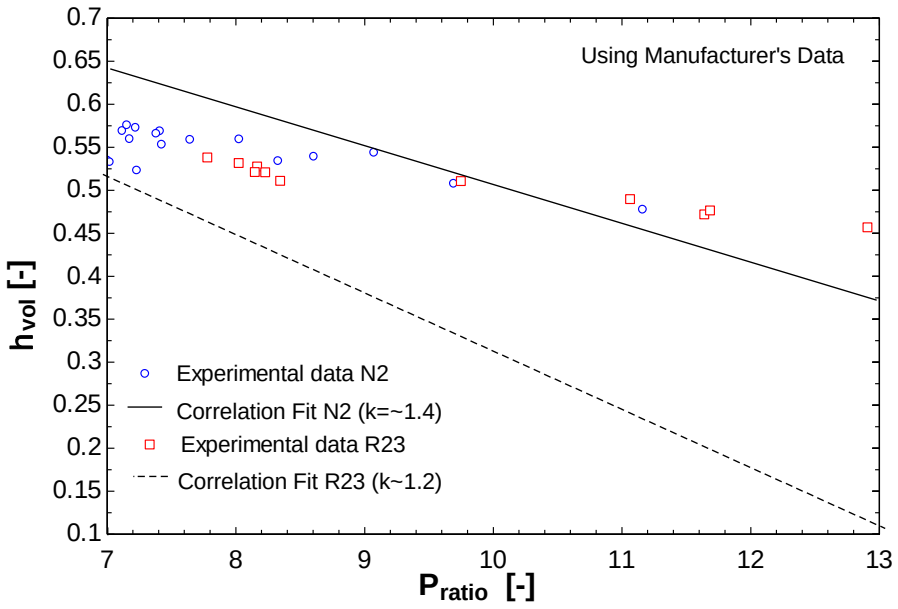

Figure 6-5: Volumetric efficiency as a function of the pressure ratio with correlation fits using the manufacturer's data to estimate the displacement rate.

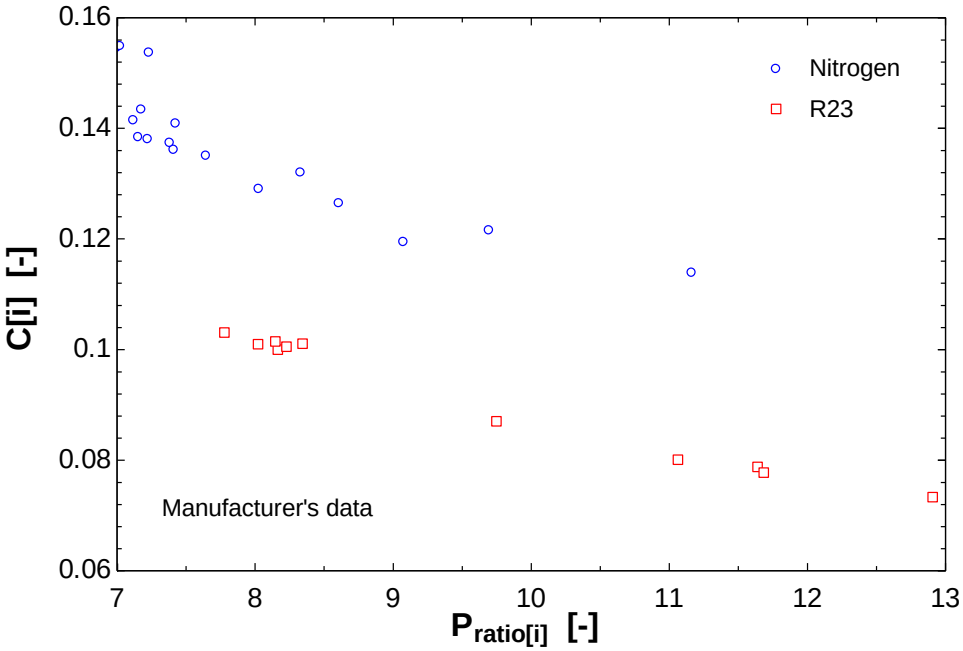

Figure 6-6: Calculated clearance volume as a function of pressure ratio for each experimental point.

6.3.2 Displacement Volume (Short Circuit) Experiments

Since the displacement rate calculated from the manufacturer's data did not accurately describe the performance of the compressor, short circuit data were taken to estimate the displacement volume of the compressor. The bypass valve was placed in the fully open position and the high and low pressure sides were blocked off for these tests, creating an open circuit (see Figure 6-7). Assuming no pressure drop through the lines, the high and low side pressures are assumed equal:

$$P_{suction} = P_{discharge} \tag{6.6}$$

Substituting this result into Eq. (6.1), the volumetric efficiency and pressure ratio are both equal to one and the displacement rate must be equal to the measured suction volumetric flow rate:

$$\eta_{vol} = \frac{\dot{V}_{suction}}{\dot{V}_{disp}} = 1 + C - C(1)^{\frac{1}{n}} = 1 \tag{6.7}$$

$$\dot{V}_{suction} = \dot{V}_{disp} \tag{6.8}$$

Experimental tests were run with this configuration using nitrogen as the working fluid over the full range of possible charge pressures. Figure 6-8 shows the results of these tests, displaying the volumetric flow rate as a function of the pressure at the compressor inlet. As these tests were taken using the original calorimetric flow meters post-calibration (see Section 2.2.2), the uncertainty in the measured mass flow is very high (3 std L N_2/min). Also, the data exhibit a relatively large range of values which is not consistent with the attempt to measure a constant displacement rate; the lowest and

highest values vary by 10%. The average value of the measured displacement rate is about 30% lower than the value calculated from the data reported by the manufacturer.

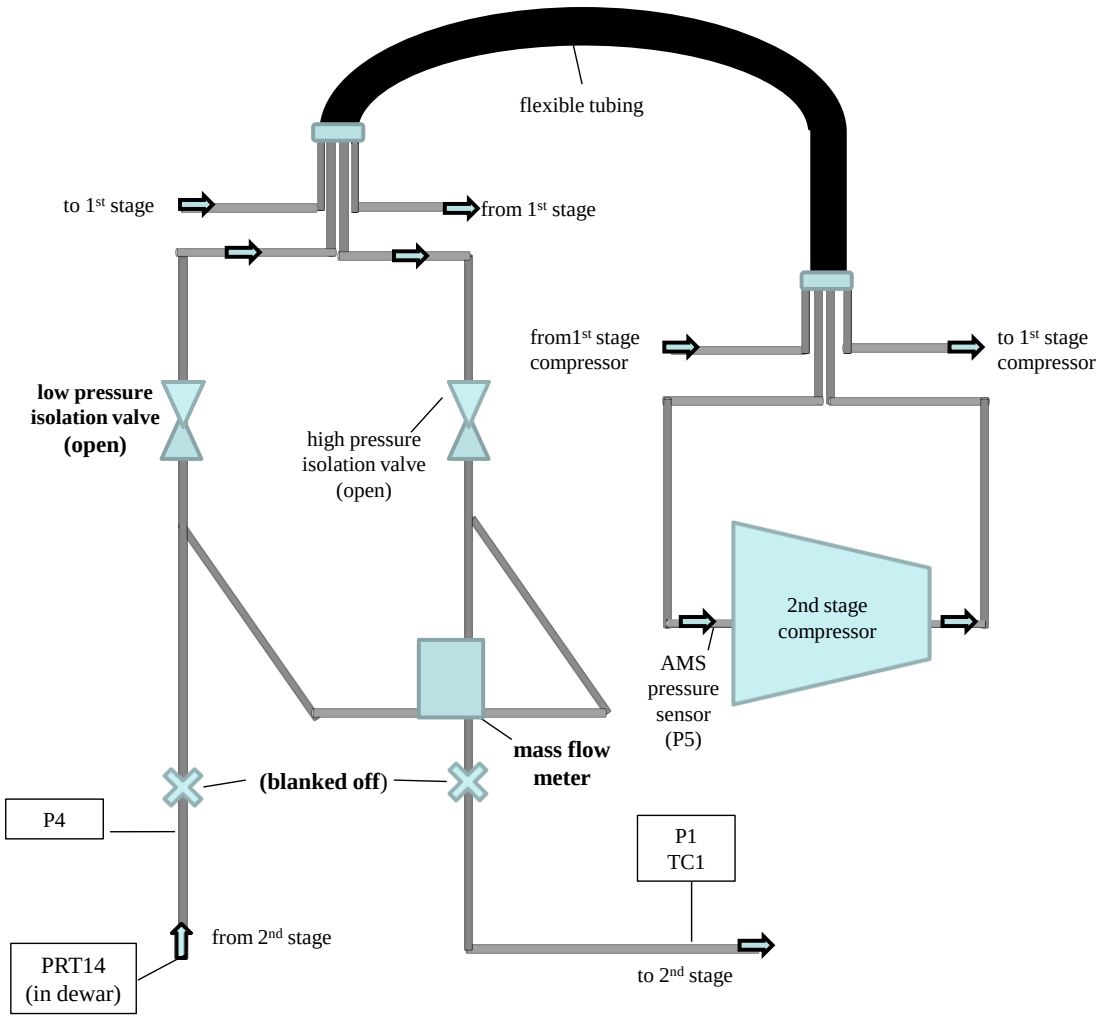

Figure 6-7: Partial cycle diagram (not shown to scale) for short circuit tests.

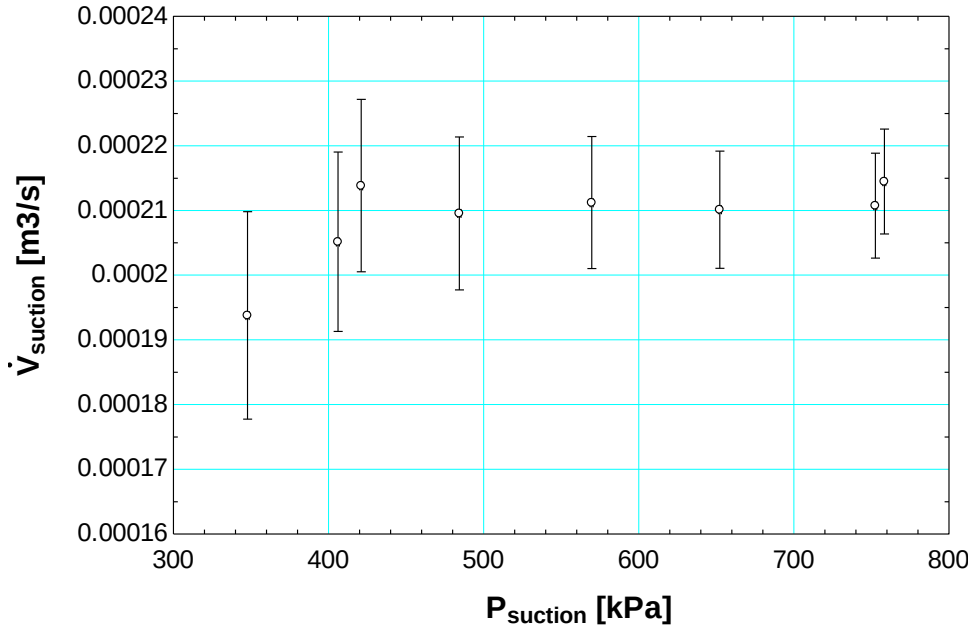

Figure 6-8: Volumetric flow rate as a function of the compressor inlet pressure for the short circuit tests.

The average suction volumetric flow rate from the short circuit tests was used as an estimate of the displacement rate. As in the previous section, *C* is then the only variable not measured in Eq. (6-1) and the clearance volume ratio can be calculated for each experimental point and averaged to find the best overall estimate. The estimates of the clearance volume ratio and the displacement rate calculated using this method are shown in Table 6-5 with the RMS errors. Figure 6-9 shows the volumetric efficiency of the experimental data as a function of the pressure ratio, with curve fits formulated using the short circuit data. The fits are significantly better than those using the manufacturer's data; however, it is still evident that the fits do not follow the trend of the data very well, especially for the R23 tests (>14% RMS error). With the large experimental uncertainty

of these tests and the poor fits, it seems that the short circuit tests may not estimate the displacement rate accurately.

Table 6-5: Compressor correlation form with the short circuit data used to estimate the displacement rate.

Correlation form (using short circuit data)	***C*** **[-]**	$\dot{V}_{disp}$ **[m^3/s]**	E_{RMS} **Nitrogen**	E_{RMS} **R23**	E_{RMS} **all data**
$\eta_{vol} = \frac{\dot{V}_{suction}}{\dot{V}_{disp}} = 1 + C - C\left(\frac{P_{discharge}}{P_{suction}}\right)^{\frac{1}{k}}$	0.07812	0.0002086	0.038	0.099	0.069

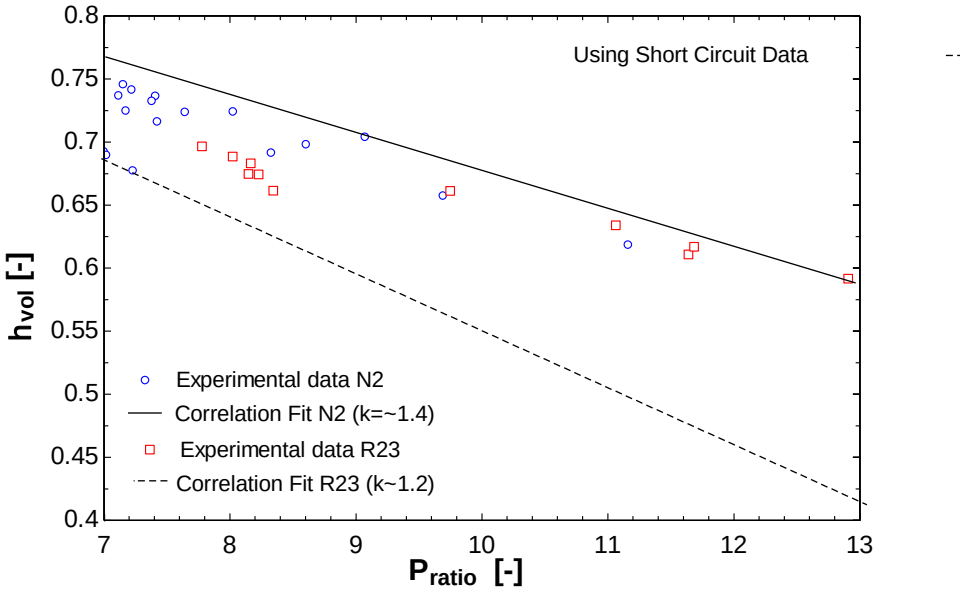

Figure 6-9: Volumetric efficiency as a function of the compressor pressure ratio with correlation fits using the short circuit data to estimate the displacement rate.

6.3.3 Two Degree Optimization

A two degree optimization using the variable metric method in EES was used to find the best fit values for the clearance volume ratio and displacement rate by minimizing the overall RMS error between the predicted and measured volumetric efficiency. The optimization was carried out by minimizing the overall error for the nitrogen and R23 data separately and also for all of the data together in order to determine values of displacement rate and clearance ratio. The fits are shown in Figure 6-10, and the clearance volume ratio and displacement rate values chosen are presented in Table 6-6 along with the E_{RMS}.

(a)

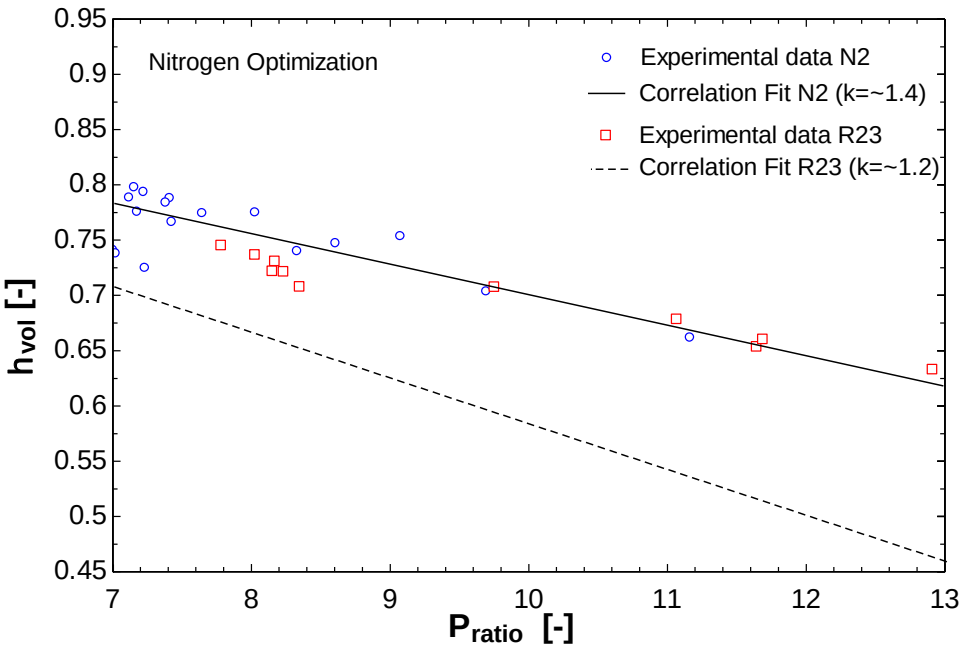

(b)

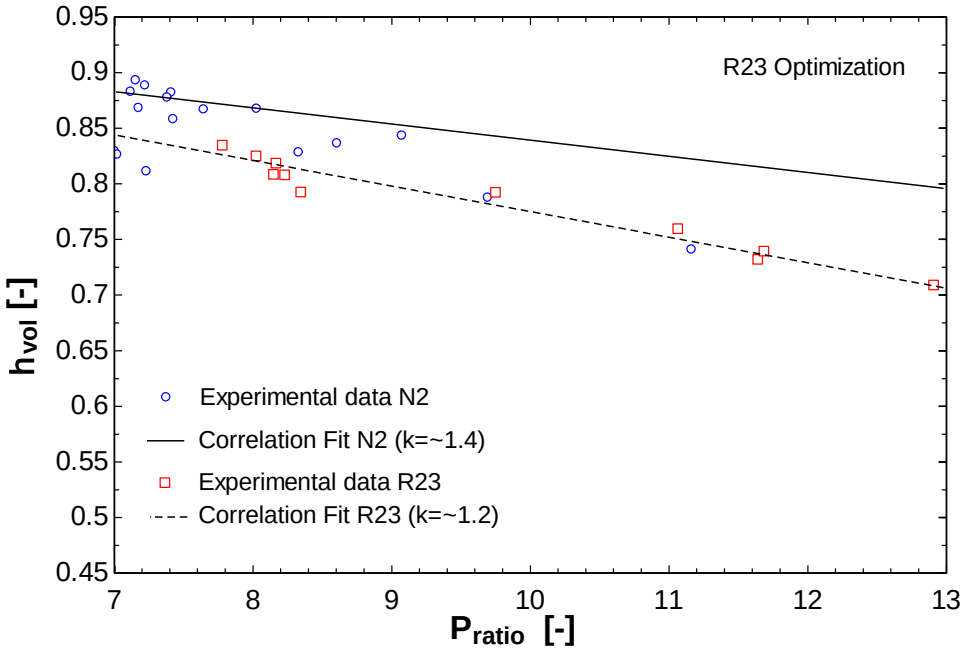

(c)

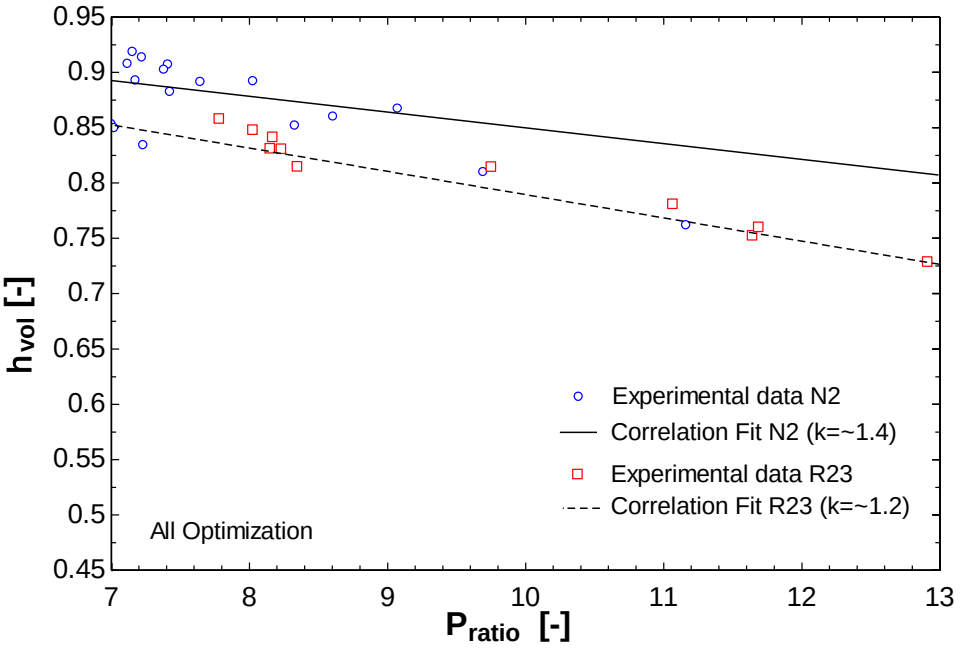

Figure 6-10: The optimization results, showing the volumetric efficiency calculated for the experimental data as a function of pressure ratio. The corresponding fits are shown for minimization of the E_{RMS} of (a) the nitrogen data only, (b) the R23 data only, and (c) all of the data.

Table 6-6: Compressor correlation form with (a) the nitrogen data E_{RMS}, (b) the R23 data E_{RMS}, and (c) all data E_{RMS} used for the optimization.

Variable to Minimize	***C*** **[-]**	$\dot{V}_{disp}$ **[m^3/s]**	E_{RMS} **Nitrogen**	E_{RMS} **R23**	E_{RMS} **all data**
(a) E_{RMS} η_{vol}, nitrogen	0.07227	0.0001949	0.023	0.108	0.070
(b) E_{RMS} η_{vol}, R23	0.03898	0.0001741	0.036	0.009	0.029
(c) E_{RMS} η_{vol}, all data	0.03655	0.0001693	0.025	0.013	0.025

As expected, the optimization considering the nitrogen error only shows the best fit for the nitrogen data but the worst fit for the R23 data; conversely, the optimization using only the R23 error gives the best fit for the R23 data and the worst fit for the nitrogen data. The optimization using all of the data does relatively well for both data sets. The clearance volume ratio predicted by the nitrogen optimization is high; this value is expected to be under 5%, and the optimization for the R23 and all of the data fits this criteria. All three optimizations extrapolate to a volumetric efficiency near one with a pressure ratio of one. With all of this taken into consideration, the optimization using all of the data is chosen as the best representation for further analysis.

To estimate the uncertainty in the volumetric efficiency, we have the measured uncertainties of the mass flow, inlet temperature, and inlet pressure; however, we need to estimate the sensitivity of the displacement rate chosen in the optimization due to the uncertainties in the measured variables (inlet pressure, inlet temperature, mass flow rate, and outlet pressure). The optimization was run with these measured variables individually increased and decreased to the maximum expected measurement error as described in Table 6-1. The sensitivity results are presented in

Table **6-7**. All the changes are around 2% or less, with the exception of the outlet pressure's effect on the clearance volume ratio (-16%). All of the tests highlighted in gray caused the displacement rate to decrease; to observe the maximum possible effect of these uncertainties combined, all of these were implemented in the same optimization test, resulting in a clearance volume ratio of 0.0306 [-] (-16%) and a displacement rate of 0.0001663 [m^3/s] (-1.8%). This is a good estimation of the maximum expected error for the optimized value of the displacement rate, so this uncertainty is used (along with the measurement uncertainties) to examine the uncertainty in the experimental volumetric efficiency (see Figure 6-11).

Table 6-7: Sensitivity analysis for the volumetric efficiency E_{RMS} optimization for all of the data. Each variable was increased or decreased by the maximum expected error and the optimization was rerun to observe the changes in the predicted clearance volume ratio and displacement rate.

Variable name			
$P_{suction}$	**Tested Uncertainty**	**+1%**	**-1%**
	C [-]	0.03644	0.03666
	$\dot{V}_{disp}$ [m^3/s]	0.0001684	0.0001702
$T_{suction}$	**Tested Uncertainty**	**+5K**	**-5K**
	C [-]	0.03607	0.03705
	$\dot{V}_{disp}$ [m^3/s]	0.0001719	0.0001667
$\dot{m}_{2nd}$	**Tested Uncertainty**	**+1%**	**-1%**
	C [-]	0.03655	0.03655
	$\dot{V}_{disp}$ [m^3/s]	0.000171	0.0001676
$P_{discharge}$	**Tested Uncertainty**	**+20%**	-
	C [-]	0.03068	-
	$\dot{V}_{disp}$ [m^3/s]	0.0001689	-

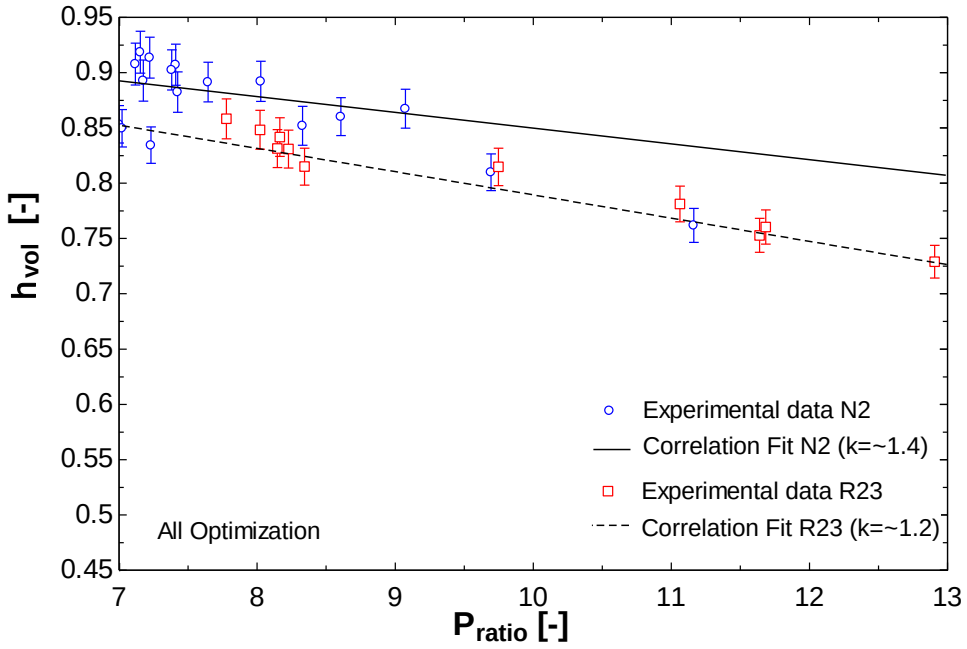

Figure 6-11: The optimization results, showing the volumetric efficiency (with uncertainty) calculated for the experimental data as a function of pressure ratio. The fits are calculated by minimizing of the E_{RMS} of all of the data.

6.3.4 Choice of Compressor Correlation

Three methods were used to try to describe the relationship between the pressure ratio and mass flow. First, the manufacturer's data were used to calculate the displacement rate of the compressor. This resulted in poor fits (E_{RMS} > 30%) and unexpectedly low volumetric efficiencies. Second, short circuit data was used to estimate the displacement rate of the compressor. The displacement rate predicted was 30% lower than the manufacturer's value, and showed improved fits; however, the experimental uncertainty in these tests was high and the R23 fit was still relatively poor (E_{RMS} > 15%). Finally, a two-degree optimization was run to find the best fit values for the clearance

volume ratio and the displacement rate. These fits were significantly improved, showing good agreement for both the nitrogen and R23 data sets. As a result, the two-degree optimization using all of the data was chosen for the compressor map (see Table 6-8).

Table 6-8: Final compressor correlation form, created using a two-degree optimization minimizing the E_{RMS} for all of the data.

Correlation Form	*C* [-]	$\dot{V}_{disp}$ [m^3/s]	E_{RMS} Nitrogen	E_{RMS} R23	E_{RMS} all data
$\eta_{vol} = \frac{\dot{V}_{suction}}{\dot{V}_{disp}} = 1 + C - C\left(\frac{P_{discharge}}{P_{suction}}\right)^{\frac{1}{k}}$	0.03655	0.0001693	0.025	0.013	0.025

6.4 References

Danfoss website, technical manual for TFS4.5CLX LBP Compressor: http://www.ra.danfoss.com/TechnicalInfo/Literature/Manuals/06/TFS45CLX_R404A-R507_115V_60Hz_09-02_Cf52d222.pdf

Jänig, D. 1999. A Semi-Empirical Method for Modeling Reciprocating Compressors in Residential Refrigerators and Freezers. MS thesis. Madison, WI USA: University of Wisconsin – Madison, Mechanical Engineering Department.

Klein, S. A. EES - Engineering Equation Solver. 2011, *9.032*, f-Chart Software, http://fchart.com.

Müller-Steinhagen H, Heck K. A simple friction pressure drop correlation for two-phase flow in pipes. *Chem Eng Process* 1986; 20:297-308.

Popovic, Predrag and Shapiro, Howard N. A Semi-empirical Method for Modeling a Reciprocating Compressor in Refrigeration Systems. *ASHRAE Transactions* 1995; 101(2):367-382.

7 Optimization

7.1 Using the Model to Select an Optimized Mixture

Past experience with the cryoprobe manufacturer (American Medical Systems) has shown that optimizing the cold tip temperature alone is not sufficient to maximize the ablation of undesirable tissue (Skye 2011); the size of the iceball formed during surgery is the target parameter used to judge the medical effectiveness of the instrument. The refrigeration capacity of the probe needs to be balanced with the tip temperature, as the refrigeration decreases with decreasing tip temperature. Also, the refrigeration capacity must be sufficient to intercept the heat input from the body that increases as the surface area of the iceball grows. Therefore, during the design process, the refrigeration capacity must be balanced with the iceball size to choose the best load temperature. This process has been studied in depth by Frederickson et al. (2004, 2006), but for the following examples a reasonable load temperature is assumed for analysis.

Sections 7.2 and 7.3 present two different examples for the commercial system studied here which optimize a binary mixture of R14 and R23, although these methods could be extended to mixtures with more than two components. Section 7.2.1 presents a parametric study that compares the optimized mixtures for the first generation and adjusted empirical models with a fixed mass flow, and Section 7.2.2 uses the compressor map from Chapter 6 to study the effects of a variable mass flow on the optimization. Section 7.3 shows an optimization that uses the genetic algorithm to determine the mixture best composition and the 2^{nd} stage operating conditions.

7.2 Optimization for Fixed Geometry and Operating Conditions

7.2.1 Fixed Mass Flow

A binary mixture of R14 and R23 is optimized for the cryoprobe studied in this project without the compressor map in order to compare the mixtures chosen by Skye's model with the adjusted empirical model described in Chapter 5. Therefore, the inputs to the model include a fixed 2nd stage mass flow, suction and discharge pressures, and 1st stage evaporator temperature (see Table 7-1 for specified values). The load temperature is varied between 170 and 210 K, but this temperature should be selected using the method described in Frederickson (2004) to achieve the largest iceball.

Table 7-1: Specified system operating conditions for the optimal binary mixture selection for the fixed geometry cryoprobe.

Parameter	Value
Load temperature (T_7)	170-210 K
2nd stage compressor discharge pressure (P_3)	289.5 psig
2nd stage compressor suction pressure (P_1)	31.7 psig
2nd stage mass flow ($\dot{m}_{2^{nd}}$)	0.0012 kg/s
1st stage evaporation temperature (T_8)	241.5 K
Mixture constituents	R14 & R23

Figure 7-1 shows the calculated refrigeration power predicted by the two versions of the empirically tuned model at varying load temperatures and mixture compositions. For these specified operating conditions, the new model predicts refrigeration powers that are lower than those predicted by the old model; however, the shapes of the curves trace closely except around the optimum value due to the differences in the correlation fits. As

a result, the optimum mixtures chosen (represented by the peaks of each load temperature curve) have a slightly lower fraction of R14. The largest difference is shown at a load temperature of 190 K, where the composition chosen using the new model contains about 6% less R14 than the old model. It is probable that different chosen operating conditions would show better agreement between the two models depending on the fluid quality in the heat exchangers, or would show a higher refrigeration capacity predicted for the new model (as shown for different experimental test points in Figure 5-11).

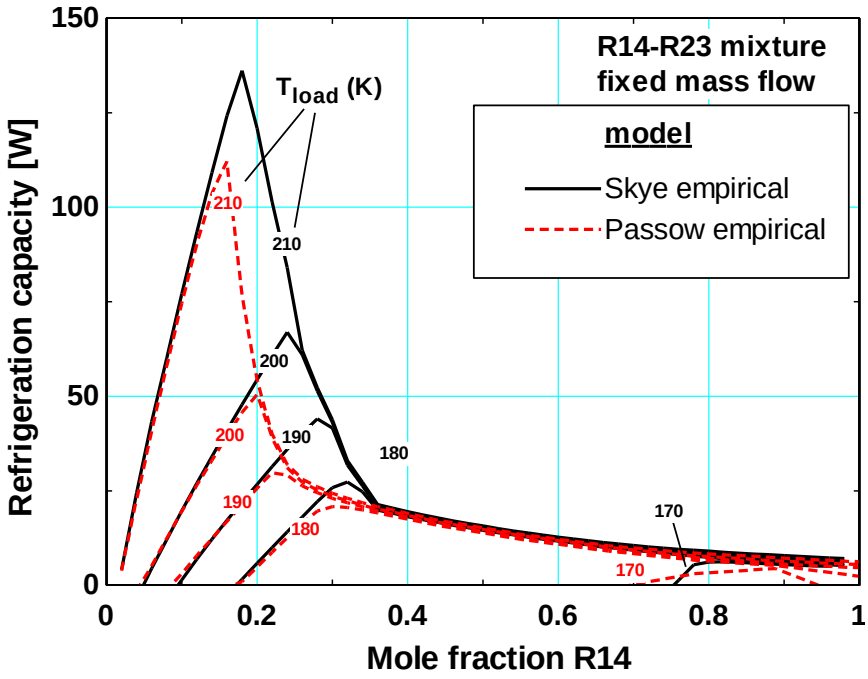

Figure 7-1: Cryoprobe refrigeration as a function of mole fraction R14 for the binary mixture. Results predicted using the first generation empirical model (Skye) and the empirical with correlations formed using the pressure drop model (Passow) are compared. (Adapted from Skye 2011)

7.2.2 Variable Mass Flow (Determined by Compressor Map)

Implementing the compressor map (see Table 6-8) allows the mass flow rate to be determined from the pressure ratio and the mixture properties. Specifying a fixed mass flow rate as in Section 7.2.1 does not consider the effects of differing mixture properties (i.e. density, c_p/c_v) on the mass flow rate, and may result in a different optimized mixture. For this analysis, a binary mixture of R14 and R23 is optimized for the cryoprobe studied in this project with the compressor map for a given load temperature, suction and discharge pressures, and 1st stage evaporator temperature (see Table 7-2 for specified values).

Table 7-2: Specified system operating conditions for the optimal binary mixture selection for the fixed geometry cryoprobe.

Parameter	Value
Load temperature (T_7)	170-210 K
2nd stage compressor discharge pressure (P_3)	289.5 psig
2nd stage compressor suction pressure (P_1)	31.7 psig
1st stage evaporation temperature (T_8)	241.5 K
Mixture constituents	R14 & R23

Figure 7-2 shows the cryoprobe refrigeration predicted for varying load temperatures and compositions for the Skye empirical model (fixed mass flow), and the adjusted empirical model with fixed and variable mass flow. The mass flows predicted by the compressor model are higher than the fixed value used in Section 7.2.1, and increase as the mole fraction of R14 increases due to the different values of the isentropic exponent (see Figure 7-3). For this example, allowing the mass flow to vary generally

does not cause a large change in the optimized mixtures; the estimated fixed mass flow in Section 7.2.1 is a relatively good estimate (taken from a 3-component experimental point with the same suction/discharge pressures analyzed here). The largest difference in mass flow corresponds to the mixtures with a larger fraction of R14 (mass flow about 30% larger for pure R14). The optimized mixture at 210 K shows the largest change due to the variable mass flow, which contains 2% less R14 than the optimization with fixed mass flow and a total 6% less R15 than Skye's model. The variable mass flow is likely to be most useful for mixtures with more than two components or components that have not been tested in the experiment, as a good estimate for the mass flow in these situations would be lacking.

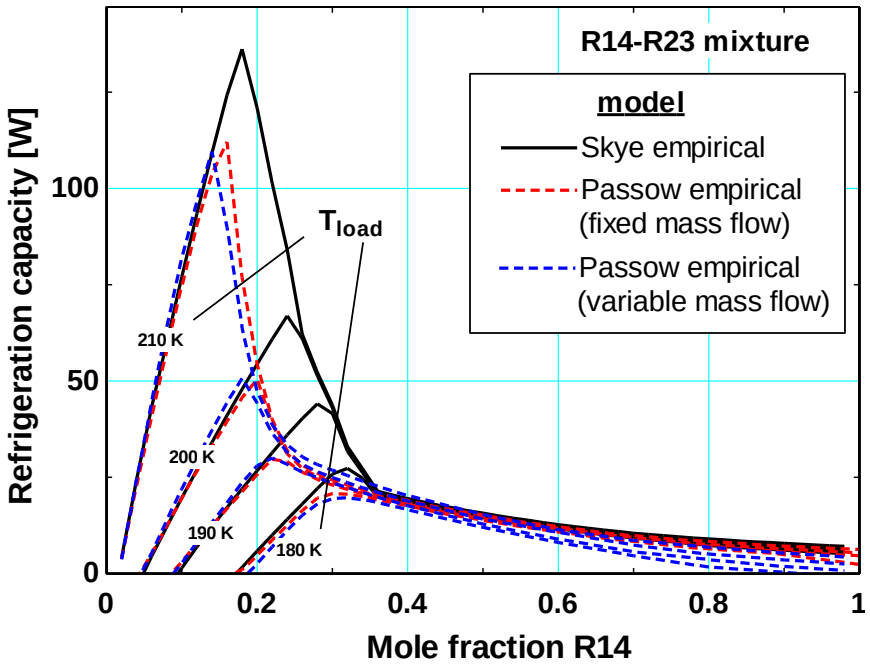

Figure 7-2: Cryoprobe refrigeration as a function of mole fraction R14 for the binary mixture. Results predicted using the first generation empirical model (Skye) and the adjusted empirical model both with fixed and variable mass flow are compared. (Adapted from Skye 2011)

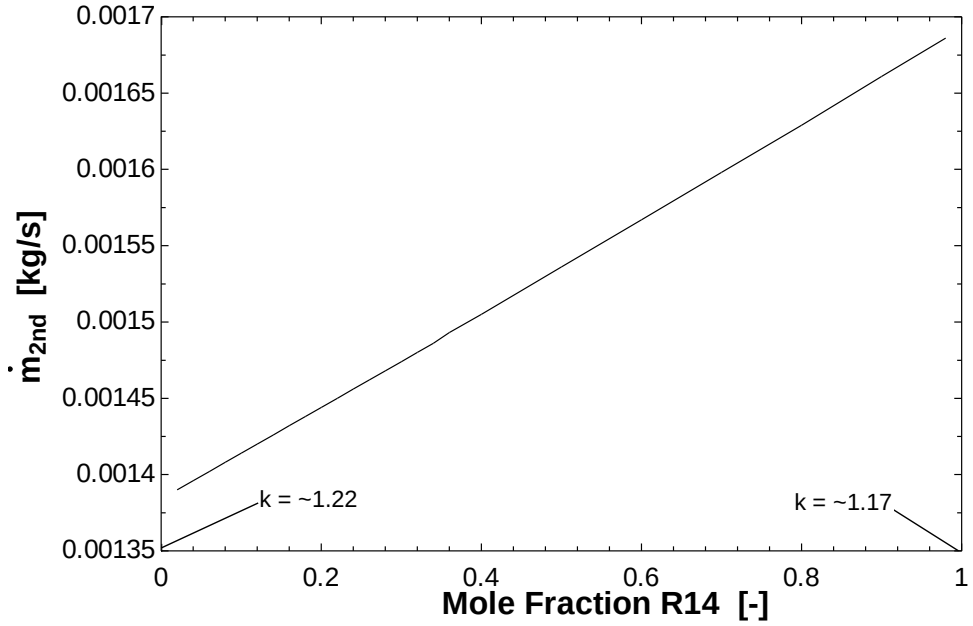

Figure 7-3: 2nd stage mass flow calculated using the compressor map as a function of the mole fraction of R14 used in the optimization. Mass flow varies with the changing isentropic exponent *k* (~1.22 for pure R23 and ~1.17 for pure R14).

7.3 Optimization for Fixed Geometry and Variable Operating Conditions

7.3.1 Optimization Summary

The parametric study in Section 7.2.1 explored the selection of best mixtures for a set of fixed operating conditions, with the suction pressure, discharge pressure, and mass flow specified. Implementing the compressor map from Chapter 6, Section 7.2.2 showed how the composition prediction changes if the mass flow is allowed to vary with the pressure ratio (as it does in a physical system). However, implementing the compressor map allows a full optimization for a fixed system in which both a mixture composition and operating conditions (high pressure, low pressure, and mass flow) that will maximize

the refrigeration power of the cryoprobe system are selected. Table 7-3 shows the remaining parameters that were specified for this optimization example.

Table 7-3: Specified system operating conditions for the optimal binary mixture selection for the fixed geometry cryoprobe.

Parameter	Value
Load temperature (T_7)	180 K
1st stage evaporation temperature (T_8)	241.5 K
Mixture constituents	R14 & R23

7.3.2 Genetic Optimization Algorithm

The optimization routine used to select the best mixture for the optimization described in Section 7.3.1 is the PIKAIA 1.2 (Charbonneau 2002) which is implemented in EES (Klein 2012). This routine finds the maximum of the objective function using an algorithm that mimics biological evolution. First, a population of individuals (i.e. sample points) is chosen at random from a specified range (determined by the bounds set on the independent variables). Next, these individuals are evaluated to determine their fitness. The 'fitness' of a sample point is determined by the calculated value of the objective function (i.e. the variable selected to be minimized or maximized). The next generation is then generated in a stochastic manner by 'breeding' selected members of the current population. Individuals with higher fitness have a higher probability of being selected for breeding, and the characteristics of the chosen individuals are passed on as encoded values of the independent variables. Random variations are also introduced by the possibility of 'mutations'.

This algorithm is useful to locate global optima when local optima also exist. This is particularly useful for the selection of best mixtures (as described in Keppler et al. 2004), whose properties have sharp discontinuities near phase boundaries and other mixture constraints. Other optimization techniques, such as the direct search and variable metric methods, have difficulties with these characteristics and as a result do not reliably converge. However, the robustness of the genetic algorithm comes at the expense of the computational speed, and faster techniques should be used if possible. In addition, the upper and lower bounds set for the independent variables are very important, as the initial population is chosen from the full range of these values.

7.3.3 Genetic Optimization Results

Table 7-4 shows the resulting optimized parameters from the genetic optimization example. Figure 7-4 illustrates the progression of the optimization, with the grey dotted lines and numbers differentiating individuals from different generations. The figure only shows individuals with a positive predicted refrigeration power; later generations had a greater number of individuals with this characteristic. This example shows that for the same few fixed parameters (load temperature, mixture constituents, and 1st stage evaporation temperature), the optimization that allows the remaining operating parameters to be optimized (suction/discharge pressures/mass flow) gives a significantly higher predicted refrigeration power; that is, running a fixed system at optimized operating conditions in addition to choosing an optimum mixture can greatly improve the system performance. For this example, the genetic optimization chooses a mixture with

about 10% more R14 and much higher discharge pressure than the previous example, which results in a refrigeration power that is greater by more than a factor of two.

Table 7-4: Optimized parameters for genetic optimization example with variable operating conditions compared with the fixed operating conditions example.

Optimized Parameters	Variable Operating Conditions	Fixed Operating Conditions
Mole Fraction R14/R23	41%/59%	30%/70%
Suction/Discharge Pressure	31.2/487 psig	31.7/289.5 psig
2nd Stage Mass Flow	0.001328 kg/s	0.0012 kg/s
Refrigeration Power	55.8 W	20.8 W

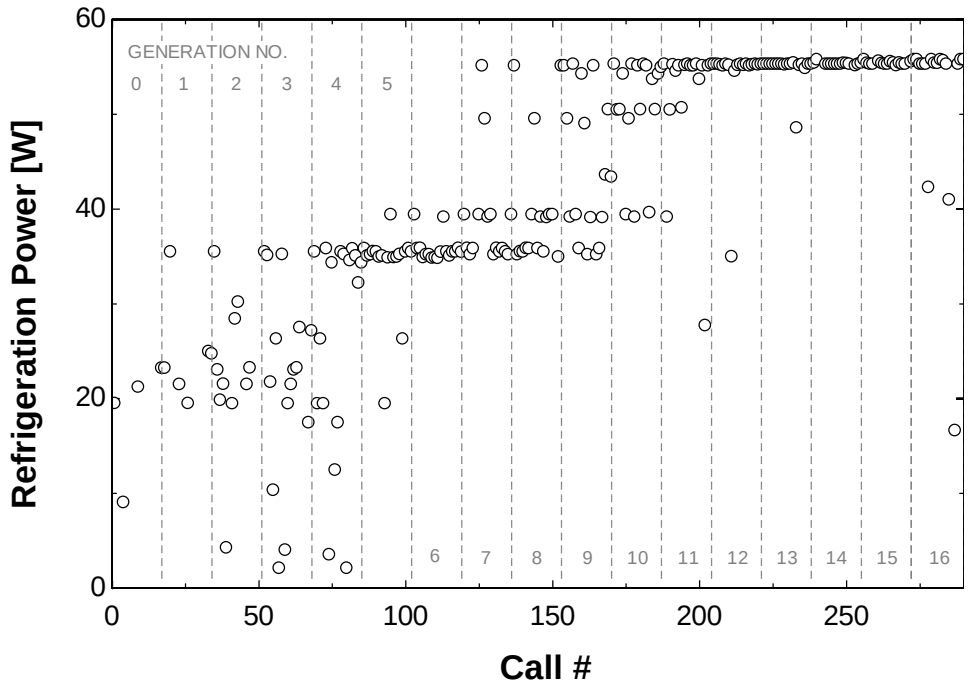

Figure 7-4: Results of optimization example, showing how the refrigeration power predictions progress with every call. The grey lines and numbers divide the individuals by generation.

The bounds in the genetic optimization should be chosen according to the physical constraints of the system; for the commercial system studied here, the discharge pressure chosen by the optimization above is higher than the nominal limit used by the cryoprobe manufacturer; AMS found that if the working pressure was above 400 psi, the compressor got too hot. Therefore, an optimization with a lower constraint on this parameter may be necessary to find reasonable operating conditions. If the upper bound on the discharge pressure is set to 400 psi, the optimized parameters are shown in Table 7-5 and the progress of the genetic optimization is shown in Figure 7-5. For this optimization, the mole fraction is more similar to the fixed mass flow example, with the composition of R14 is within 4% of the optimized composition from Section 7.2.2; however, the refrigeration power predicted still shows a marked increase, about 83% larger than the example with constrained suction/discharge pressures.

Table 7-5: Optimized parameters for genetic optimization example with more reasonable upper bound on discharge pressure. Results for the variable operating conditions are compared with the results with fixed operating conditions.

Optimized Parameters	**Variable Operating Conditions**	**Fixed Operating Conditions**
Mole Fraction R14/R23	34%/66%	30%/70%
Suction/Discharge Pressure	30.5/361.5 psig	31.7/289.5 psig
2^{nd} Stage Mass Flow	0.001381 kg/s	0.0012 kg/s
Refrigeration Power	38.0 W	20.8 W

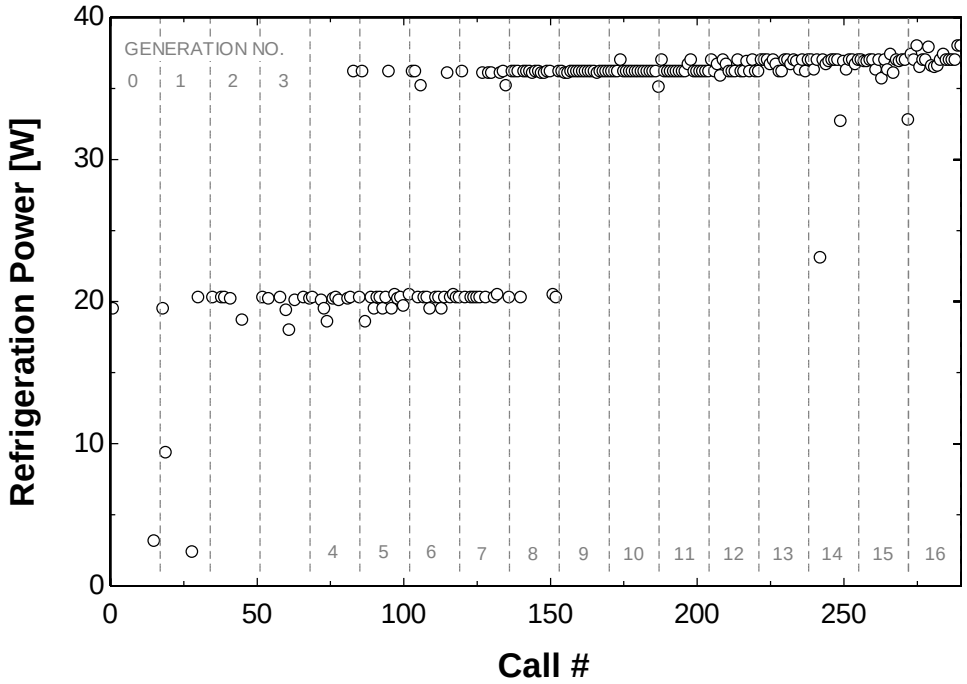

Figure 7-5: Results of optimization example with lower upper boundary on discharge pressure, showing how the refrigeration power predictions progress with every call. The grey lines and numbers divide the individuals by generation.

7.4 References

Charbonneau, P. 2002. *Release Notes for PIKAIA 1.2*, NCAR Technical Note 451+STR (Boulder: National Center for Atmospheric Research).

Fredrikson, K. 2004. Optimization of Cryosurgical Probes for Cancer Treatment. M.S. thesis. Madison, WI USA: University of Wisconsin - Madison, Mechanical Engineering Dept.

Fredrikson, K.; Nellis, G.; Klein, S. A. "A Design Method for Cryosurgical Probes". *International Journal of Refrigeration* 2006; 29:700-715.

Keppler, F. Nellis, G. and Klein, S. (2004) Optimization of the Composition of a Gas Mixture in a Joule-Thomson Cycle. *International Journal of Heating, Ventilation, Air Conditioning, and Refrigeration Research*, Vol. 10, No. 2, pp. 213-230.

Klein, S. A. EES - Engineering Equation Solver. 2011, *9.032*, f-Chart Software, http://fchart.com.

Skye, H.M. 2011. Modeling, Experimentation and Optimization for a Mixed-Gas Joule-Thomson Cycle with Precooling for Cryosurgery. PhD thesis. Madison, WI USA: University of Wisconsin – Madison, Mechanical Engineering Department.

8 Summary and Future Work

8.1 Summary

The goal of the work presented here was the improvement of the empirical MGJT cryoprobe model developed by Skye (2011). This model can be used to select the optimum refrigerant mixture for the system studied here; however, the method demonstrated to formulate the empirical correlations could be repeated for any cryoprobe system.

Chapter 1 gave an introduction to cryosurgical technology, MGJT systems, and the previous work that has been completed for the optimization of mixtures for these cycles. Chapter 2 gave a brief overview of the test facility, recent experimental modifications, and the experimental tests that have been completed to date. One important note is the unreliability of the mass flow measurements in the collected data; the original calorimetric flow meters from the two stages were tested in series and found to read 40% different, possibly due to oil damage to the sensors. These meters have now been replaced with Coriolis meters, but the accuracy of the data used to create the empirical correlations is questionable. Chapter 3 presented the detailed thermodynamic and heat transfer equations that are used for data processing. This method uses the measured temperatures and pressures in detailed numeric heat exchanger models to compute the system performance.

Chapter 4 details the pressure drop model that is used to replace the assumption that the pressure drops through the precooler and recuperator are equal. The pressure drop model uses the Müller-Steinhagen correlation to create a more physics-based

prediction of the total and intermediate pressure drops through each heat exchanger and therefore of the total conductance. The pressure drop predicted by the unadjusted model generally underpredicts the experimental pressure drop by about 25%, with higher disagreement evident with higher experimental pressure drops. Therefore, scaling the calculated section pressure drops to agree with the total experimental pressure drop is necessary. In general, the pressure predicted at state 4 only changes an average of 5%. However, the change in calculated recuperator conductance is much larger, an average of 10% with an even larger change for two-phase experimental data.

In Chapter 5, the data processed as described in Chapter 3 with the pressure drop model implemented as described in Chapter 4 is used to reformulate the empirical correlations from Skye (2011). Generally, the new correlations show a slightly worse fit than the old correlations without the pressure drop model. However, the recuperator and precooler validations show fewer instances of pinch point violation (more experimental points converge during the data processing), and fewer instances with predicted effectiveness values greater than one. Additionally, the mass flow meter readings from the experimental data are unreliable; if this data is retaken, the hope is that the correlation fits will improve.

Chapter 6 describes the process used to create a compressor model in order to relate the pressure ratio to the system mass flow. The displacement rate and the clearance ratio were the primary unknowns in the volumetric efficiency model used, where the polytropic exponent n was replaced by the isentropic exponent k which varies with mixture composition. Performance experiments using nitrogen and R23 were conducted with the bypass closed, such that the clearance volume ratio could be calculated for each

data point and averaged if the displacement rate is known. The displacement rates calculated using the manufacturer's data and using the short circuit experiments were found to create curve fits that fit the data poorly. Instead, a two degree optimization was used to create the compressor map.

Chapter 7 shows examples of optimizations for the fixed geometry for the cryosurgical system studied here. First, a parametric study with fixed mass flow was used for direct comparison with an optimization from Skye (2011). The optimum mixtures predicted differed in R14 composition by up to 6%. Then, the compressor map was used to estimate the varying mass flow from the suction/discharge pressures used in the optimization. For this example, the varying mass flow changed the optimized composition by less than 2%; however, for operating conditions and mixtures beyond the scope of the experimental data, the compressor map will be an important tool. Finally, an example of a genetic optimization was shown, where the compressor map was used to allow the optimization of the suction/discharge pressures in addition to the composition of the mixture. This example showed that allowing the operating conditions to be optimized may result in a much higher refrigeration power for a given geometry as well as a different optimum mixture composition; however, the system limits must be taken into account when setting the boundaries for the optimization.

8.2 Future Work

The data used to create the empirical correlations presented in Chapter 5 have high uncertainty due to the mass flow error (see Section 2.2.2). The hope is that with the new Coriolis meters, data that will provide better correlation fits can be retaken. The Coriolis meters should not have the same issues with the oil as the previously used calorimetric flow meters; they directly measure mass without diverting the flow stream through a restriction, and carefully monitored density readings should signal when oil is entering the system. For this new set of data, a wide range of operating conditions should be attempted to ensure the broad applicability of the model. In particular, two-phase precooler data and low quality recuperator data was lacking in the current data set; focusing on these regions in new data taken with the Coriolis meters should improve the predictive capability of the model.

To achieve these low quality data, further testing with binary mixtures of R14-R23 would be advantageous. In comparison with mixtures with a great number of components, these binary mixtures have properties that compute relatively quickly with high accuracy, and it is relatively easy to mix two constituents in the system to vary the composition. In addition, the particular binary combination of R14 and R23 has been shown to give good two-phase recuperator data as well as data with high refrigeration power at higher load temperatures. However, to achieve data with a two-phase condition in the precooler and data with increased refrigeration capacity at lower temperatures, the addition of a constituent with a relatively high boiling point such as R410a or R134a may be required.

Once the data has been retaken and the correlations have been reformulated, optimized mixtures such as the ones shown in Section 7.3.3 may be tested in the experiment for validation purposes. However, additional modeling and/or experimental work may be required for this to be successful. First, the compressor map should be validated with other pure refrigerants as well as refrigerant mixtures. Also, the effect of the charge pressure should be studied. A higher charge pressure has been shown to create higher suction and discharge pressures in the system, thereby causing a smaller JT effect across the jewel orifice and overall higher cycle temperatures. Exploring the relationship between the compressor pumping power, the total system volume, and the flow restrictions and the subsequent distribution of refrigerant in the system (and therefore, pressures) could be useful for optimizing the charge pressure of a given mixture.

Additionally, it has been shown (see Section 5.4.2 of Skye 2011) that the composition of the circulating mixture can change significantly from the charged composition. This occurs as mixture components are preferentially adsorbed in the compressor oil or condense out of the mixture based on their individual boiling points. It is the circulating mixture that represents the working fluid for the cycle, and this composition must be used to calculate the thermodynamic performance of the system. However, this makes formulating an optimized mixture difficult, as the circulation at the optimized operating condition may be significantly different than the charged mixture. Further study to determine the relationship between the charged and circulating mixture is necessary to test mixtures optimized using the empirical model that has been developed.

8.3 References

Gong, M.Q.; Wu, J.F.; Qi, Y.F.; Hu, G.; and Zhou, Y. “Research on the Change of Mixture Compositions in Mixed-Refrigerant Joule-Thomson Cryocoolers”. Advances in Cryogenic Engineering, Vol 47, 2002

Gong, M.; Zhou, W.; and Wu, J. “Composition Shift due to Different Solubility in Lubricant Oil for Multicomponent Mixtures”, Cryocoolers 14, 2007

Gong, M.; Deng, Z.; Wu, J.; “Composition Shift of a Mixed-Gas Joule-Thomson Refrigerator Driven by an Oil-Free Compressor”, Cryocoolers 14, 2007

Skye, H.M. 2011. Modeling, Experimentation and Optimization for a Mixed-Gas Joule-Thomson Cycle with Precooling for Cryosurgery. PhD thesis. Madison, WI USA: University of Wisconsin – Madison, Mechanical Engineering Department.

APPENDIX: Standard Operating Procedure

Startup

1) Experimental Equipment Setup

a) Restart computer to refresh memory
b) Turn on SCXI 1000 DAQ system
c) Turn on Lakeshore 332 Temperature Controller – make sure heater is off
d) Turn the Variac heater switch to 140 V - make sure the dial is set to 0%
e) Turn on Solenoid Valve Rheostat – set to 100%
f) Check vacuum level in dewar is < 1 x 10-4 Torr (see *Evacuating the Dewar* section below)
g) Make sure all fans are plugged in
   i) USB fan for vacuum turbo
   ii) Oil separator fan
   iii) 1st stage evaporator fan
h) Set voltage of Harrison 6296A DC Power Supply between 50-250mV (allows AMS unit to turn on even if GMC pressure is not in the allowed range)
i) Manual Ball Valves
   i) KF-40 evac port valve - closed
   ii) Pressure gauge isolation valve - closed --> already closed during fill (SEE *Refrigerant Recovery* section below)
   iii) GMC compressor high pressure isolation valve – open
   iv) GMC compressor low pressure isolation valve – open
   v) Bypass valve - mostly closed

2) DAQ Software

a) Upload previous day's data to the shared network drive
b) Start National Instruments Labview 8.6
c) Open latest version of "Cryoprobe" vi from C:\Desktop\DAQ\
d) Input the fluid information, mixture information, and jewel size into the LabVIEW interface
e) Input the vacuum pressure in the dewar read from the 943 Cold Cathode Pressure gauge
f) Input the Ambient pressure read from the barometer next to the lab door
g) Deselect 'Solenoid Valve Sequence'
h) Select 'Use default flow meter values'
i) Run the Labview interface, making sure the "Create new CONTINUOUS file?" and "Write to CONTINUOUS file?" buttons are clicked to on (green light on) if you want to create and new file and write to it.
j) Save the file for data collection in the "Data" folder on the desktop, including date and mixture information in the file name
k) Check the static charge pressure – typical values are:
   i) GMC 65-85 psig
   ii) PCC 145 psig

3) Lab Notebook during Startup

a) Record file name
b) Record charge mixture and starting pressure
c) Record the values of the min/max frequency and min/max density values corresponding to each Endress Hauser flow meter
d) Record times of start of PCC and GMC cycles

4) Start System

a) Make sure that the cryoprobe system is plugged in and the power switch is on
b) Turn the PCC Cycle switch off (it's in the gray "High Voltage Danger" box)
c) Start GMC cycle
    i) Press power button on CryoGen System, wait for system to warm up (~3 min.)
        (1) If system errors out, try adjusting the multimeter voltage - usually the value is between 50mV and 250mV (record this value in the notebook)
        (2) If the pressure in the PCC is too low the system will return an error (the PCC is not supplied a 'trick' voltage like the GMC, and ~45 psig is required for startup)
    ii) From LCD control screen, press option button (left button)
    iii) Scroll down 2 spaces to blank option using down arrow
    iv) Press up arrow, down arrow, and right buttons simultaneously to go into "Service Mode"
    v) Press right button to select "View Sensors"
    vi) Press "-" button on the "cryoprobe handle" to begin the cycle
d) Begin solenoid valve sequence
    i) Set "Minutes between Valve cycles" to 30 min.
    ii) Set "Solenoid Sequences to Skip – PCC" to 3
    iii) Click "Solenoid Valve Sequence" button in the LabVIEW VI (valves should immediately go through sequence)
    iv) NOTE: If valves cycle successfully, the system pressures should momentarily change as the gas bypasses the system; sticky valves may need to be cycled manually
e) Regulate the GMC cycle pressures using the 2nd stage compressor bypass valve
    i) P1 should be 275-325 psig, PR should be ~10 (i.e. P1/P5 in psi <10)
f) Keep an eye on mass flow and pressure differences to ensure system is not clogging/freezing (mass flow will cut off rapidly and pressures will spike if freezing occurs, in which case you must turn off the system and complete the triple evacuation process for maintenance)
g) Set desired heater value
    i) Go to "Lakeshore 332" tab in LabVIEW
    ii) Select desired "Manual Output" range
    iii) Configure "Heater Range" to "High"
    iv) Set Loop to 1
    v) Press "Configure" and observe the measured heater power [W]
    vi) Adjust "Manual Output" value, pressing "Configure" after each adjustment, until the desired wattage is attained
h) Wait for steady state condition
    i) As the system nears steady state, increase the valve sequence time to 30-60 minutes to give the system enough time to stabilize
    ii) "Steady State" condition defined as a 20 minute period over which the temperatures change less than 0.25 K (confirm that pressures are also stable)

i) Keep door shut to minimize ambient temperature fluctuations

Data Collection

1) Record any unusual observations or deviations from normal procedure
2) Keep door shut to minimize ambient temperature fluctuations
3) Keep an eye on frost conditions on experiment
   a) If frost forms on 2nd stage return tube (approaching GC collection point), use variac heater (silvery blue) to make sure GC is taking only vapor sample
   b) Be careful of melting frost on experiment-use paper towels to keep experiment dry and rust-free. Be especially aware of special vacuum fittings with small welded pieces.
4) Steady State
   a) After criteria for steady state have been met (<0.25 K change in all temperatures over 20 minutes), record the start and stop times in the lab notebook corresponding to steady state
   b) Record steady state measurements in notebook for future reference (pressures/temperatures/heater values/flow rates, etc.)
   c) Take GC point (see *Gas Chromatograph Operation* section below)
5) Reset the valve sequence to 15 minutes
6) Adjust the heater value for the next steady state condition

Gas Chromatograph Operation

1) Turn on Helium carrier gas
   a) Hook up the copper tubing that connects the Helium bottle to the GC carrier line and to the sample line on the GMC
   b) Open the helium tank and turn in the regulator until the pressure in the carrier line is 50-55 psig (as read on the Column Head Pressure gage on the GC front panel)
   c) NOTE: He regulator is touchy, and CHP gage may take several minutes to adjust
2) Turn on the GC (switch is on right bottom side), and wait for self-check routine to finish
3) Prepare GC components
   a) Set the oven temp to 50ºC by pressing the OVEN TEMP button, followed by the ON button
   b) Set the injector temp to 100ºC by pressing INJ A TEMP, then ON
   c) Turn TCD A detector on by pressing DET, A, and ON
4) Allow TCD signal to come to equilibrium (to view the TCD signal, press SIG 1 twice)
   a) The baseline signal should become steady in the range of 3.5 to 4.5 after 30-60 min
   b) Wait until there is no variation in the signal for ~10 min
   c) NOTE: changing the CHP pressure will change the baseline.
5) Turn on the HP Integrator if using for data collection (push button on the back)
   a) Allow unit to warm up, wait for green "READY" LED to light up
   b) Press the ATTN key twice (it will print "ATT ^2"), press 5, then ENTER
      i) NOTE: This scales the peaks so they fit on the page without being cut off (increasing the attn will make the peaks smaller)
   c) Press the THRSH button twice (it will print "THRSH"), press 5, then ENTER
      i) NOTE: This sets the threshold for noise reduction (increasing the threshold will decrease the amount of noise picked up)
6) Flush sample line with Helium

a) Open the screw valve near GMC sample point
b) Let helium flow at 10-20 ccm (read on rotameter by GC) for 10 minutes
c) Close screw valve

7) Adjust GMC sample flow
   a) Make sure black valve on left side of GC is barely open
   b) Open sample line ball valve when steady state has been achieved in GMC
   c) Adjust P_{gage} to ~10-20 psig and P_{diff} to ~0.08-0.12
      i) Look at "GC" tab in Labview for values
      ii) Adjust readings by changing the positions of the black screw valve (left side of GC) and rotameter dial (on top of GC)
8) Begin GC run
   a) Make sure "NOT READY" light on front of GC is off
   b) Record the P_{gage}, P_{diff}, rotameter flow measurement (may be very small), and TCD baseline values in the notebook
   c) If just using integrator:
      i) Press "Start" on front of GC
      ii) Press "Start" on Integrator
      iii) Wait for 2nd hiss (signaling close of pneumatic injection mechanism)
      iv) Close sample line ball valve
      v) Wait until all peaks elute (~ 20 min for R23)
      vi) Press STOP on integrator to see measurements
      vii) Record areas in notebook
   d) If using LabVIEW Cornell GC software in conjunction w/ integrator:
      i) NOTE: The integrator is run in addition to the LabVIEW software to validate the new digital method
      ii) NOTE: The GC must be set to an older Firmware Mode (HP 5890 Series A mode) to work with the software. This is accomplished by jumping P15 (consists of two pins) on the GC's main PC board.
      iii) Open GasChromatograph.lib
      iv) Open GasChromatograph.vi from LLB Manager
      v) Accept Terms and Conditions, Click OK
      vi) Press "Set Method"
         (1) Temperature default values should be correct (Oven temp 50ºC, Inj A port 100º, TCD temp 100ºC)
         (2) Change data rate to 5 Hz
         (3) Press OK
         (4) Turn TCD ON
         (5) Wait for temperatures to adjust
         (6) Press OK
      vii) Follow setup for integrator (step 5 above)
      viii) Press "Measure Sample"
         (1) Press ok
         (2) Press START on integrator
         (3) Wait for 2nd hiss (signaling close of pneumatic injection mechanism)
         (4) Close sample line ball valve
         (5) Wait until all peaks elute (~ 20 min for R23)
         (6) Press STOP on integrator to see measurements
         (7) Press STOP on LabVIEW vi
         (8) Save chromatogram

(a) Press “Save Chromatogram”
(b) Enter name and description, and record in lab notebook
(9) Set peak threshold, max noise, and min points to fit in vi to 0 to allow program to autocalculate retention times and areas
(10) Copy results to Excel to calculate corrected mole percents

9) After all desired GC points have been recorded:
   a) Quit LabVIEW GC vi
   b) Turn GC off
   c) Turn off helium carrier gas

Shutdown

1) Turn Lakeshore 332 Temperature Controller to 0%
2) Turn off Variac heater
3) Cycle 1st and 2nd stage solenoids manually
   a) Press “Manual Override”
      i) Press “GMC Valve 1”, leave for 4-8 sec and then turn off
      ii) Press “GMC Valve 2”, leave for 4-8 sec and then turn off
      iii) Press “PCC Valve 1”, leave for 4-8 sec and then turn off
4) Turn off Solenoid valve Rheostat
5) Turn off PCC Cycle first (using the switch in the High Voltage box)
6) Press “+” button to turn off GMC cycle
7) Allow ~10 min. for fans to cool compressors
8) Unplug all fans
9) Allow LabVIEW data to continue to collect data as the system warms up
10) As the system warms up, wipe off the snow and water that collects on the tubes and dewar
   a) NOTE: Leaving water on the sensors and fragile weld vacuum connections can cause sensor damage and rust!
11) Press power button on CryoGen system to turn machine off

Refrigerant Recovery

1) Connect the Promax Refrigerant Recovery Machine (RG6000) to a 115V outlet
2) Check to make sure the inlet and outlet valves on the RG6000 are both set to closed
3) Connect the inlet line on the RG6000 unit to the GMC low Schrader valve (closed)
4) Connect the outlet line on the RG6000 unit to the blue (liquid) valve on the appropriate (R410a or Mix) yellow recovery tank (NOTE: max psi of 350)
5) Slowly open the blue (liquid) valve of the recovery cylinder while watching hoses and connections for leaks
6) Set the recover/purge valve on the RG6000 unit to “RECOVER”
7) Open the outlet valve on the RG6000 unit
8) Toggle the power switch to the “ON” position
9) Open the inlet valve on the unit
10) Slowly open the low Schrader valve, about 1 psi drop per update
11) Note: If the unit begins to “knock,” slowly throttle back the Schrader valve until the noise stops
12) Run the RG6000 until the desired vacuum is achieved

13) Close the low Schrader valve
14) Turn the inlet valve on the RG6000 to the "CLOSED" position
15) Toggle the power switch to the "OFF" position
16) Purge Procedure
17) **CAUTION: Always purge the RG6000 unit after a recovery procedure. Failure to purge the remaining refrigerant from the unit could result in acidic degradation of internal components, ultimately causing premature failure of the unit.**
18) Verify the Schrader valves are closed
19) Verify the outlet valve on the unit is open and the inlet valve is closed
20) Verify the liquid valve on the recovery cylinder is open
21) Turn the recover/purge valve to the "PURGE" position
22) Toggle the power switch "ON"
23) Slowly turn the inlet valve toward the "PURGE" position
24) As the inlet side pressure decreases, open the valve to the full purge position
25) Run the unit until the desired vacuum is achieved
26) Close the inlet and outlet valves on the unit
27) Toggle the power switch "OFF"
28) Close the ports on the recovery cylinder
29) Turn the recover/purge valve to the "RECOVER" position

Triple Evacuation/Purge for GMC plumbing

1) Recover refrigerant in GMC (see *Refrigerant Recovery* above)
2) Evacuate
   a) Make sure pressure in system is <2 psig
3) Connect orange cart roughing pump to system
   a) Connect to KF-40 evac port
   b) Connect to GMC high Schrader valve
   c) Connect to GMC low Schrader valve
   d) Connect to Convectron vacuum gauge 1
4) Valves
   a) KF-40 evac port valve - closed
   b) Convectron vacuum gauge 2 isolation valve – closed (pressure > ambient could ruin gauge)
   c) High pressure isolation valve - closed
   d) Low pressure isolation valve – closed
      i) NOTE: Closing the isolation valves helps keep oil from entering the system
   e) Bypass valve - open
   f) GMC high Schrader valve - closed
   g) GMC low Schrader valve - closed
5) Turn on vacuum pump
   a) Evacuate refrigeration hoses and KF-fittings to 200 mTorr
6) Slowly system valves
   a) Crack open the KF-40 evac port valve
   b) Wait about 30 s before opening the vacuum gauge isolation valve (where Convectron vacuum gauge 2 is located)
   c) Watch the pressure gauge while slowly opening KF-40 evac port valve the rest of the way

i) Make sure the gauge stays in a vacuum and that the pump is not being overworked
d) Wait until vacuum gauge 1 (nearest the roughing pump) is at 200 mTorr

7) Evacuate from GMC low Schrader port
   a) Slowly open GMC low Schrader valve with small adjustments
      i) Open valve a small increment, observe vacuum pressure jump
      ii) Wait until vacuum pressure returns to low value (after ~1 minute) before next small adjustment
      iii) Continue until GMC low Schrader valve fully open
   b) Open solenoid valves one at a time, waiting for pressure to return to 200 mTorr
   c) After about 10 minutes, close both solenoid valves
8) Evacuate from GMC high Schrader port
   a) Open valve slowly
9) Wait for vacuum pressure to reach its lowest value
   a) The first evacuation will take longer (maybe leave overnight)
   b) Subsequent evacuations may take only 3-4 hours
   c) Previous low points have been ~ 150 milliTorr (on 2nd/3rd evacs)
   d) Record vacuum level and time to reach ultimate vacuum in lab notebook
10) Stop evacuation process
   a) Close the valves
      i) KF-40 evac port valve - closed
      ii) Convectron vacuum gauge 2 isolation valve – closed
         (1) Don't blow out the vacuum gauge! – close vacuum gage valve
      iii) High pressure compressor isolation valve - open
      iv) Low pressure line valve - open
      v) Bypass valve - closed
      vi) GMC high Schrader valve – closed
      vii) GMC low Schrader valve - closed
   b) Turn off the vacuum pump
11) Purge with Nitrogen
   a) Ball Valve Settings
      i) KF-40 evac port valve - closed
      ii) Convectron vacuum gauge isolation valve 2 - closed
         (1) Don't blow out the vacuum gauge! – close vacuum gage valve
      iii) High pressure compressor isolation valve - open
      iv) Low pressure compressor isolation valve - open
      v) Bypass valve - closed
   b) Open Nitrogen tank valve, pressure on backside of regulator should read tank pressure
   c) Check that regulator frontside pressure reads 0
   d) Open brass valve screw valve
   e) Purge fill line including the Service Access valve
      i) Turn regulator dial in until gas comes out – regulator pressure gauge may not move, listen for gas exiting fill fitting
      ii) Allow to purge for ~10-15 seconds where last 5 seconds are with service access valve screwed mostly onto GMC high Schrader port
         (1) NOTE: It is important that there is no air in the system – air has water in it which will freeze in system
   f) Tighten Service Access Valve on GMC high Schrader valve– finger tight, plus ~1/2 turn. If Fill fitting leaks during pressure increase, tighten fitting
   g) Turn regulator dial in until the pressure reads ~20-40 psig

   h) Open GMC high Schrader valve SLOWLY, such that the pressure rises ~2 psig per LabVIEW measurement update
   i) Watch GMC pressures in LabVIEW under the "Filling pressures" section
   j) When median pressure reaches desired pressure, close Schrader valve
12) Turn Regulator valve all the way out
13) Close brass screw valve
14) Close Nitrogen tank valve
15) Disconnect fill line and open GMC low Schrader valve to relieve pressure to ~2 psig
16) Close GMC low Schrader valve
17) Repeat Evacuation – record vacuum level
18) Purge
19) Final evacuation
   a) Connect the refrigerant fill line to the GMC high Schrader port via the service access valve to evacuate the fill line (the vacuum pump will only be connected to the LP Schrader port and the KF-40 Evac port)
   b) Open tank valve for refrigerant, pressure on backside of regulator should read tank pressure
   c) Check that the regulator (front) pressure reads 0
   d) Open screw valve
   e) Purge fill line including the Service Access valve
      i) Turn regulator dial in until gas comes out – regulator pressure gauge may not move, listen for gas exiting fill fitting
      ii) Allow to purge for ~10-15 seconds where last 5 seconds are with service access valve screwed mostly onto GMC high Schrader port
      iii) NOTE: It is important that there is no air in the system – air has water in it and will freeze in system
   f) Tighten Service Access Valve on GMC high Schrader valve– finger tight, plus ~1/2 turn. If fill fitting leaks during pressure increase, tighten fitting
   g) Close screw valve
   h) Open GMC high Schrader valve
   i) Proceed with evacuation as normal (steps 4-10, ignoring 8)
20) Record vacuum level
21) Fill with desired refrigerant after 3 evacuations and 2 Nitrogen purges

Charging the GMC Cycle Plumbing with Refrigerant

1) Complete Triple Evac/Purge process
2) There should be a vacuum on the system of less than 100 mTorr
3) Check valve positions
   a) KF-40 evac port valve - closed
   b) Convectron vacuum gauge 2 isolation valve – closed
      i) Don't blow out the vacuum gauge! – close vacuum gage valve
   c) High pressure compressor isolation valve – open
   d) Low pressure compressor isolation valve – open
   e) Bypass valve – closed
   f) GMC high Schrader valve – closed
      i) Should be connected to refrigerant with fill line evacuated
   g) GMC low Schrader valve - closed
4) Open screw valve on refrigerant

5) Open GMC high Schrader valve
6) Turn Regulator Valve in to ~70 psig (or +5psi whatever charge pressure is needed)
    a) Watch Labview pressures, regulating rate with the Schrader valve
    b) System will lose some charge before beginning
7) Close Schrader valve
8) Turn Regulator valve all the way out
9) Close brass screw valve
10) Close refrigerant tank valve
11) ALTERNATIVELY: Use manifold to charge system
    a) Connect hoses
        i) Connect hose from high Schrader port to left side manifold connection
        ii) Connect second hose from vacuum system to middle manifold connection
        iii) Connect third hose from desired refrigerant to right side manifold connection
    b) With all manifold valves open and the Schrader port closed, run vacuum to evacuate fill lines
    c) Close middle manifold connection valve and turn off vacuum
    d) Turn in refrigerant regulator to desired pressure
    e) Open GMC high Schrader port SLOWLY, adding ~2 psi per LabVIEW update
    f) When desired charge is achieved, close Schrader port and see Refrigerant Recovery to recover refrigerants that cannot be released into the atmosphere

NOTE: To evacuate and charge the PCC you must use the PCC low Schrader port. Everything else is the same as for the GMC cycle except that there are no intermediate valves (like the high and low isolation valves) that need to be closed on the PCC.

NOTE: If the regulator on the bottle does not go high enough to achieve the desired charge pressure, you will have to attach the fill line to the LOW Schrader valve (not the high valve) and suck in refrigerant when the compressor is running. This will work for both the PCC and GMC. Be aware that you won't know what the true resting charge pressure is until you turn the compressors off and let the system cool down.

Evacuating the Dewar

1) Connect gray roughing pump to the dewar by attaching the stainless steel vacuum hoses to the T-fitting attached to the turbo vacuum pump
2) Make sure purge valve is screwed closed
3) Makes sure blue valve lever by roughing pump is closed
4) Turn roughing pump on
5) Slowly open blue valve lever
6) Watch Convectron vacuum pressure gauge (near the cold cathode gauge) to ensure pressure decreases slowly
7) Listen to pump pitch and smell for pump oil to make sure pump is not overworked
8) When valve is fully open, wait for a pressure of ~1000 milliTorr to ensure there are no leaks
9) Press start on the turbo controller
    a) Make sure the USB fan cooling the turbo is plugged in
10) Turn on 943 Cold Cathode Pressure gauge to read vacuum pressures less than 1e-3 torr
11) Wait until 943 Cold Cathode Pressure gauge reads a vacuum of < 1x10-4 Torr before starting experiment